# Interfacial Engineering of Highly Efficient Perovskite Solar Cells with Charge-Transporting Polymers

# 電荷輸送性ポリマーによる界面制御とペロブスカイト太陽電池の高性能化

February 2020

**Koki SUWA**

諏訪　康貴

# Interfacial Engineering of Highly Efficient Perovskite Solar Cells with Charge-Transporting Polymers

# 電荷輸送性ポリマーによる界面制御とペロブスカイト太陽電池の高性能化

February 2020

Waseda University
Graduate School of Advanced Science and Engineering
Department of Advanced Science and Engineering,
Research on Applied Chemistry A

**Koki SUWA**

諏訪　康貴

Promoter: Prof. Dr. Kenichi Oyaizu
Referees: Prof. Dr. Yukio Furukawa
Prof. Dr. Yoshinori Nishikitani
Dr. Michio Suzuka
Prof. Dr. Hiroyuki Nishide
Dr. Ludmila Cojocaru

# *Preface*

Organic-inorganic perovskite solar cells have attracted significant attention because of their high photovoltaic conversion efficiency (> 25 %), facile fabrication processes, and wide applicability due to their positive beneficial characteristics, which include their weightlessness, bendability, and semi-transparency. Besides, the possibility of achieving tunable band gaps by optimizing the perovskite composition renders the perovskite solar cells useful for application in various tandem solar cells. However, the further improvement in the photovoltaic conversion efficiency, a reduction in the cost of hole-transporting materials, and an extension in a lifetime determined by unstable perovskite and hole-transporting layers have continuously been investigated.

Charge-transporting polymers, with sufficient hole mobility, have been studied extensively as components of organic electric and photoelectric devices owing to their satisfactory film formability and adjustable energy levels. The charge-transporting polymers, with outstanding stability, can be used effectively to improve the conversion efficiency, the fabrication process, and the durability of the perovskite solar cells.

In this thesis, the charge-transporting polymers were incorporated in the perovskite solar cells as a hole-transporting layer and an effective scaffold for high-quality perovskite grain formation to enhance their photovoltaic characteristics. The polymers were also, for the first time, applied to the hole-transporting layer of evaporated perovskite solar cells for improving their durability. Chapter 1 outlines the characteristics of the perovskite solar cells and the properties as well as applications of the charge-transporting polymers. Chapter 2 describes the synthesis of highly soluble arylamine polymers and their application as the hole-transporting materials. Chapter 3 describes the application of TEMPO polymers as effective scaffolds and as eliminating agents for superoxide anion radical which decomposes the perovskite compounds at the perovskite surface. Chapter 4 describes the in-situ vapor phase polymerization of hole-transporting thiophene derivatives and their application for the evaporated perovskite solar cells. Chapter 5 displays the device configurations of perovskite/silicon and perovskite/perovskite tandem solar cells using the hole-transporting polymers. The last chapter summarizes this thesis and presents prospects of the studies described in this thesis.

Koki Suwa

# CONTENTS

### Chapter 4 Vapor-Phase Formation of Hole-Transporting Polymer Layers and their Applications for Evaporated Perovskite Solar Cells

### Chapter 5 Tandem Solar Cells with a Vapor-Phase Formed Hole-Transporting Polymer

### Chapter 6 Conclusion and Future Prospects

# Chapter 1: General Introduction

## 1.1 Introduction

An effective use of renewable energy is important not only for environmental conservation on a global scale, but also for the further development of the world economy governed by the sustainable development goals (SDGs). Solar cells offer a solution for the procurement of large amounts of clean energy from the sun, which emits 177 trillion kW of energy toward the earth annually. To allow for the widespread use of solar cells, new types of solar cells have been in demand that can be fabricated at a low cost and exhibit easy handling as well as versatility for multiple applications.

Organic-inorganic halide perovskite compounds have been used as light absorption and photoelectric conversion layers in the next-generation solar cell since their first use in 2009 by Miyasaka *et al.*; these are characterized by light absorption in the entire visible light range, an approximately 100% internal quantum efficiency, and a long carrier diffusion length of several micrometers.[1] These solar cells, known as “perovskite solar cells”, have attracted the considerable attention of several researchers and industries because of their high photovoltaic conversion efficiency, low fabrication costs, and broad applicability, e.g., as walls, windows, car bodies, and Internet of Things (IoT) devices.[2–4] Although, the perovskite solar cells are currently being developed for practical applications, the cell durability and the fabrication of large-area cells remain significant problems.[5]

Firstly, the chemical stability of both the commonly used hole-transporting organic compound, 2,2,7,7-tetrakis(*N,N*-di-*p*-methoxyphenylamine)-9,9-spirobifluorene (spiro-OMeTAD), and the perovskite compounds is still considerably poor.[6–8] Although the application of oxygen and moisture barrier layers, and/or the encapsulation of whole devices have been reported to retard the decomposition of spiro-OMeTAD and perovskites for guaranteeing cell durability, these methods do not provide a fundamental solution to the problem of chemical instability.[9–11] Therefore, the use of highly durable hole-transporting materials to replace spiro-OMeTAD could present an effective method for enhancing the durability of the perovskite layer.

Tandem solar cells fabricated with two or more light-absorbing layers are effective and profound methods for enhancing the overall photovoltaic conversion efficiency.[12,13] The perovskite solar cells, in particular, are suitable for use as the top cell of the tandem cells with silicon cells owing to their facile film formability and the adjustability of the photoelectric properties related to the perovskite composition.[14]

However, the second problem, the large area fabrication, has hindered the applicability of the perovskite solar cells in tandem cells.[15] Although evaporation can be conducted to form clean and homogeneous layers on large substrates with a pyramidally structured surface to suppress light reflection and redirect light into the cells, the design of hole-transporting materials for the evaporation process is an additional problem. [16,17]

Charge-transporting polymers including π-conjugated and non-conjugated polymers are characterized by excellent film formability, high carrier mobility, and structural stability. Furthermore, these polymers can possibly solve the previously mentioned problems of the perovskite solar cells.[18,19] Highly solvent-soluble and facilely prepared hole-transporting polymers are expected to form homogeneous and durable charge-separation layers to replace spiro-OMeTAD and enhance the durability of the perovskite solar cells. Non-conjugated polymers with organic stable radical species of 2,2,6,6-tetramethylpiperidine-1-oxyl (TEMPO) can be effective scaffolds for forming high-quality perovskite layers and eliminating superoxide anion radical to extend the lifetime of the perovskite solar cells.[20,21] These polymers are difficult to apply for dry processes using the evaporation method due to their large molecular weight and strong intermolecular interactions. However, an in-situ polymer layer formation could resolve the problem related to the large area fabrication of the highly durable perovskite solar cells on pyramidal silicon substrates.

In the research described in this thesis, the application of the charge-transporting polymers for enhancing the photovoltaic characteristics of the perovskite solar cells is investigated as follows: (1) Arylamine-based polymers were prepared via facile addition-condensation as robust and effective hole-transporting materials of the perovskite solar cells. (2) TEMPO polymers were incorporated in perovskite precursor solution to form high-quality perovskite grains for enhancing the photovoltaic performance and durability. (3) An in-situ vapor phase formed thiophene polymer was applied as a stable hole-transporting layer to evaporated perovskite solar cells and perovskite/silicon tandem solar cells.

To provide the necessary background, this section includes a review of the fundamental characteristics of the perovskite solar cells and the charge-transporting polymers. In section 1.2, the basic properties and configurations of the perovskite solar cells are described. In section 1.3, the charge-transporting polymers are classified according to their molecular structure, and described in terms of electric properties and device application. In section 1.4, previously reported methods for improving the photovoltaic characteristics and durability of the perovskite solar cells are reviewed from the viewpoint of an interfacial engineering.

## 1.2 Perovskite Solar Cells

### 1.2.1 Conventional solar cells and expectations regarding a new solar cell

A solar cell is a type of electric device that converts light energy, specifically sunlight, to electricity. Solar cells consist of a light-absorbing layer with a band gap that corresponds to the wavelength of absorbed light, charge-transporting layers for the extraction or blocking of charges, and electrodes.[22,23] The photovoltaic characteristics of solar cells can be evaluated using the following four parameters: short circuit current density ($J_{SC}$), open circuit voltage ($V_{OC}$), fill factor ($FF$), and photovoltaic conversion efficiency ($\eta$), as shown in Figure 1.1.[23]

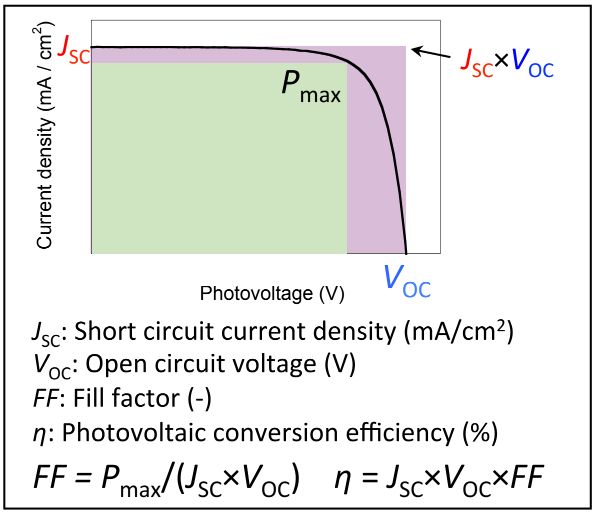

Figure 1.1 Parameters regarding photovoltaic conversion performance of solar cells.

The efficiencies of most types of solar cells are summarized in the Best Research-Cell Efficiency Chart of the National Renewable Energy Laboratory (NREL) (Figure 1.2).[24] In this chart, monolithic solar cells can be divided into the following three types: silicon solar cells, thin film solar cells with direct-gap semiconductors, and organic solar cells.

Silicon solar cells, the most common and market-competitive solar cells, consist of a *p*-doped silicon (with an aluminum dopant) layer, an *n*-doped silicon (with a phosphorus dopant) layer, and electrodes.[25,26] The junction of these silicon layers integrates Fermi levels by band bending.[27] The silicon layers have an appropriate band gap ($E_g$ = 1.1 eV), and their bent bands become the driving force for charge separation and drift diffusion to an external circuit.[27] These cells are classified into single crystal, polycrystal, and amorphous silicon solar cells, and have various uses depending on their application.[28,29] However, as silicon is an indirect-gap semiconductor, the formation of a thick silicon film can be problematic as the film causes the cells to become heavy and unbendable. In addition, the efficiency of these cells also seems to have reached a peak.

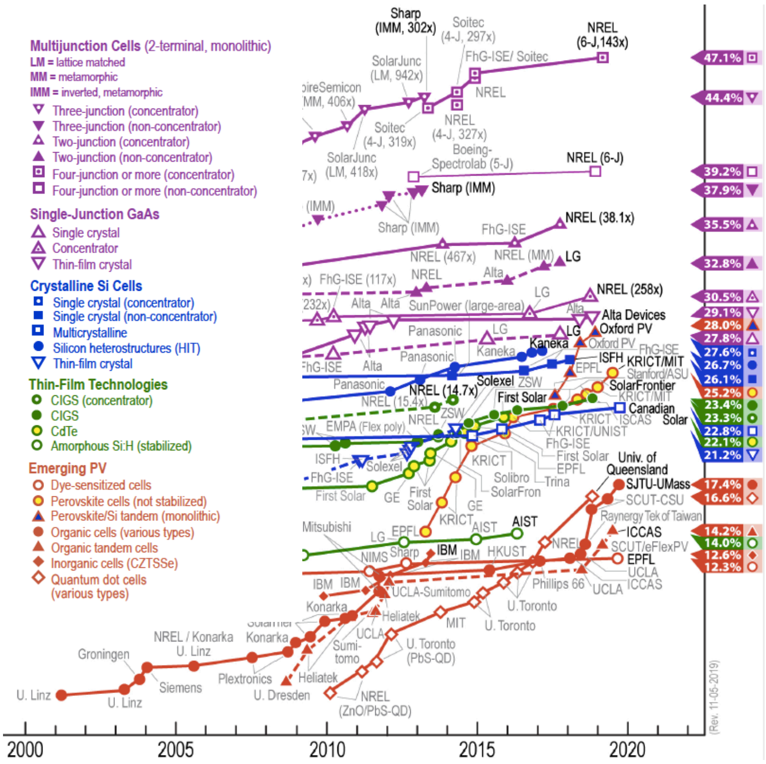

Figure 1.2 NREL chart since 2000.[24]

A second-generation solar cell, which is a thin film solar cell using direct-gap semiconductors, has been developed for higher efficiency.[30] These solar cells consist of transition metals, for example, CIGS (Cu, In, Ga, and Se) or GaAs, and show high efficiency (> 30%) in monolithic cells. However, their production costs are extremely high and they have only been used in limited applications, such as in outer space.[31,32]

Organic solar cells fabricated by organic multilayers have been proposed since the 1970s.[33,34] Unlike for solar cells made of inorganic materials, the organic solar cells do no use band bending as the driving force for charge diffusion, as the organic layers do not create a band structure.[35] In organic solar cells, organic materials (mainly *p*-type materials) with appropriate band gaps absorb sunlight to generate excitons. These excitons then diffuse to the interfaces with the other materials (mainly *n*-type materials) and are separated to holes and electrons, with each charge moving to the counter electrode by drift diffusion.[35] Charge separation occurs only at the interfaces, resulting in a low efficiency due to excitons being wasted through charge recombination. This occurs even with a bulk heterojunction structure that creates a wide interface by mixing *p*- and *n*-type materials in bulk. An additional problem that has been encountered is the low durability of the organic compounds. Dye-sensitized solar cells (DSSCs) made up of organic dyes, which act as light-absorbing materials on the surface of titanium dioxide, have been proposed by Grätzel *et al.*[36,37] The DSSCs exhibit a high efficiency, especially considering that they are organic solar cells. However, the handling of these cells is not facile as organic solvents and ionic materials are used as mediators.[38,39] Therefore, there is a need for solar cells that have a high conversion efficiency, are easy to handle, have a low cost fabrication process, and are broadly applicable.

### 1.2.2 Perovskite solar cells and their photovoltaic conversion layers

Organic-inorganic perovskite solar cells have attracted worldwide attention due to their high photovoltaic conversion efficiency (> 25%), their facile processability, and their low cost fabrication methods, from firstly announced by Miyasaka *et al.* in 2009.[1,40,41] Furthermore, their positive characteristics, which include being thin, light-weight, flexible, and transparent, have made them suitable for various applications, not only on roofs like silicon solar cells, but also for windows, coatings for houses or cars, and for IoT devices.[42] The organic-inorganic perovskite solar cells consist of light-absorbing perovskite compounds, hole-transporting materials, electron-transporting materials, and electrodes (Figure 1.3).[43]

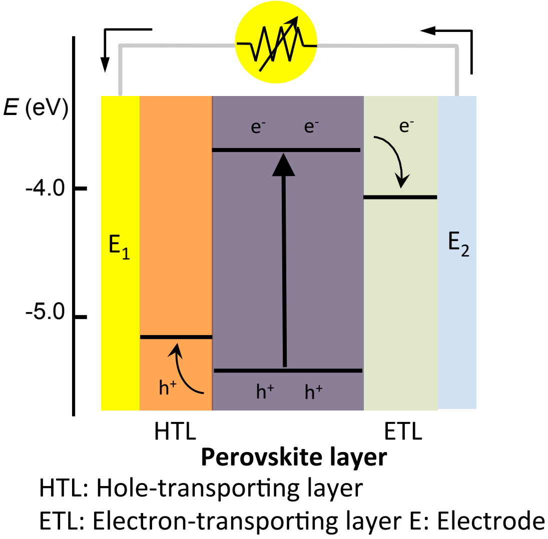

Figure 1.3 Configuration of perovskite solar cells.

Originally, “perovskite” referred only to calcium titanium oxide ($CaTiO_3$).[44] However, currently, the “perovskite” is also applied to the same type of crystal structures known as perovskite structures ($ABX_3$). The word “perovskite” is derived from the Russian nobleman Lev Perovski, the founder of the Russian Geographical Society.[44] Organic-inorganic perovskite compounds that are utilized in the light-absorbing layer of the solar cells also consist of $ABX_3$ structures, but with specific A, B, and X sites (Figure 1.4).[45,46] Examples of A sites are organic cations of methylamine ($CH_3NH_3$) and formamidine ($CH(CH_2)_2$) or large alkyl cations of cesium (Cs) and rubidium (Rb).[47–49] The B sites consist of central transition metals with mainly lead (Pb) being used due to its high photovoltaic conversion efficiency. However, Pb suffers the problem of environmental load, therefore, tin (Sn) or bismuth (Bi) are also used instead of Pb.[50,51] Halogens, such as iodine (I), bromine (Br), and chlorine (Cl) are used as X sites. The combination of A, B, and X sites determines the chemical, physical, and photoelectrical properties of perovskite compounds, such as the band gap and carrier mobility, as well as the photovoltaic performance of the solar cells, e.g., open circuit voltage ($V_{OC}$) and short circuit current density ($J_{SC}$). The selection of A, B, and X must confirm to a tolerance factor limitation, which determines a capable combination to form specific crystal phase structures, as shown in Equation 1.1.[44,52]

$$t = \frac{r_B + r_X}{\sqrt{2}(r_A + r_X)} \quad \text{(Eq. 1.1)}$$

*t*: tolerance factor, *r*: molecular radius of each site

The tolerance factor should be close to 1, otherwise, the photo-electric convertible α-phase of the perovskite structure is not formed.

.

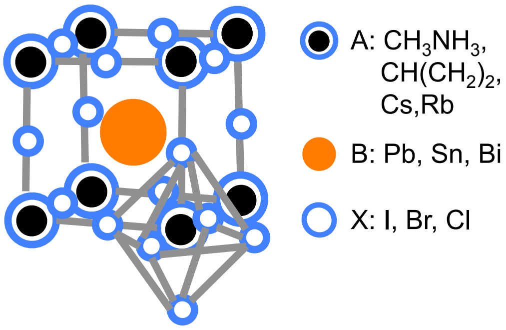

Figure 1.4 Structure of perovskite compounds.

The specific characteristics of the monolithic perovskite compounds include wide light absorption in the entire range of visible light, simple high quality crystal formation, and direct charge separation not through excitons; the efficiency of charge separation can be regarded as 100%. Additionally, perovskite compounds with multiple types of materials have also been reported as mixed-cation (A sites) perovskite or mixed-halide (X sites) perovskite compounds.[41,53] Highly efficient perovskite solar cells could be realized with the use of the mixed-cation and -halide perovskite layers due to their enhanced light absorption abilities in wider wavelengths with different light absorbing materials, their high-quality perovskite crystal formations with improved stability, and their ability to adjust the tolerance factor.[52] The above-mentioned perovskite compounds are used as light-absorbing layers, i.e., as *i*-type semiconductors, and stacking *p*- and *n*-type semiconductor layers can separate the hole and electron from the perovskite layers.

Perovskite layers have been fabricated using solution methods in the most reports.[54–59] Perovskite precursor materials of AX and $BX_2$ are dissolved in polar organic solvents, such as *N,N'*-dimethylformamide (DMF) and dimethyl sulfoxide (DMSO) to obtain high-quality perovskite crystal by precipitation.[54] The simplest method is a casting, in which the solvent is volatilized. However, the formed crystal layers are usually not homogeneous because the solvent deposition is too slow to form a homogeneous crystal layer.[55] Although, an anti-solvent method, which promotes crystal nucleation by dropping a poor solvent during spin-coating, has been widely used for the formation of highly efficient perovskite layers, this method requires expertise of how to properly drop the anti-solvent.[56,57] Recently, a two-step method, which forms high-quality perovskite layers by sequentially depositing AX and $BX_2$ solutions, has been successfully applied; however, the method is difficult to reproduce in all laboratories.[58,59] Although the efficiency is not high, a bar coating method and a role-to-role method using industrially available inks have also been studied due to their applicability in upscaling the cell area and simplifying the fabrication processes.[60,61] While these solution processes are relatively simple, a number of challenges still remain, including the use of “strong” or hazard-possible solvents, remnants of the solvent molecules in the perovskite layer, and the difficulty of forming a homogeneous layer upon textured substrates.

Evaporation methods, including co-evaporation and a sequential evaporation, have also been studied to solve the issues of the solution processes.[16,62,63] The innovative method could form a clean and homogeneous perovskite layer along the under layers without utilizing solvents.[64,65] On the other hand, these methods need complex evaporation systems, require expertise knowledge, and have a limitation of applicable materials.

### 1.2.3 Fabrication processes of the perovskite solar cells and its components

The representative structure of perovskite solar cells can be classified with *n-i-p* and *p-i-n* (inverted) configurations (Figure 1.5).

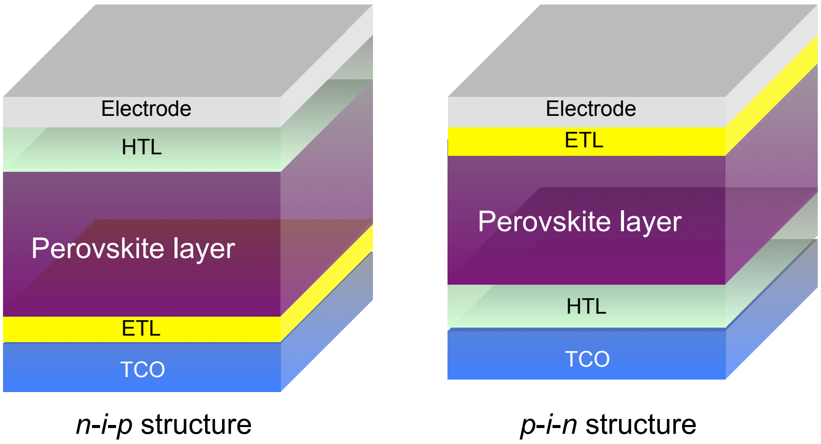

Figure 1.5 *n-i-p* and *p-i-n* configurations of perovskite solar cells.

In the *n-i-p* configuration, cells comprise the following order of layers: a transparent conductive oxide (TCO), an electron-transporting layer (ETL), a perovskite layer, a hole-transporting layer (HTL), and a counter electrode.[66] Two types of under layers can be used for the *n*-*i*-*p* configuration: one is a mesoporous-type under layer and the other is a planar-type under layer. Mesoporous-type perovskite solar cells possess both a compact metallic oxide thin layer and a mesoporous metallic oxide layer, with mainly titanium dioxide ($TiO_2$) as the ETL on a thermally stable fluorine-doped tin oxide (FTO) as the TCO.[67,68] Planar-type perovskite solar cells are fabricated with a planar metallic oxide layer, such as $TiO_2$ and tin oxide ($SnO_2$) formed on an indium-doped tin oxide (ITO), which demonstrates improved planarity and transparency instead of less thermal stability, which the FTO displays.[69,70] The planar $SnO_2$ layer shows a higher conductivity than the $TiO_2$ layer; however, the lattice constant of $SnO_2$ is dissociated from that of the perovskite compounds.[71] Results from research on a hybrid planar layers formed by both $SnO_2$ and $TiO_2$ showed an improvement in the matching of the lattice constant between the perovskite layer and the under layers.[72]

Organic charge-transporting materials that are soluble in chlorobenzene, chloroform, and toluene (solvents which do not dissolve the perovskite layers), have mainly been applied to the HTL of the *n*-*i*-*p* configured cells by solution processes. For example, low molecular weight compounds of spiro derivatives, representatively spiro-OMeTAD, and arylamine derivatives, including *N*4, *N*4, *N*4”, *N*4”-*tetra*([1,1’-biphenyl]-4-yl)-[1,1’:4’,1”-terphenyl]-4,4”-diamine (TaTm) and *N,N*’-bis(naphthalene-1-yl)-*N,N*’-bis(phenyl)-benzidine (NPD), hole-transporting polymers of poly[bis(4-phenyl)(2,4,6-trimethylphenyl)amine] (PTAA) and poly(3-hexylthiophene) (P3HT), and narrow band-gap polymers with donor-accepter structures, such as poly[*N*-9′-heptadecanyl-2,7-carbazole-*alt*-5,5-(4′,7′-di-2-thienyl-2′,1′,3′-benzothiadiazole)] (PCDTBT), have been utilized as HTLs of the *n*-*i*-*p* configured cells.[73–77] Amorphous low molecular weight compounds, such as spiro-OMeTAD, need to form a comparatively thick layer of ca. 100 nm due to their low film formability and should be treated with an additional chemical doping using a cobalt oxide, such as tris(2-(1*H*-pyrazol-1-yl)-4-tert-butylpyridine)cobalt(III) tri[bis(trifluoromethane)sulfonimide] (FK209), and a lithium salt, such as lithium bis(trifluoromethylsulphonyl) imide (LiTFSI), as well as *tert*-butylpyridine (*t*BP) as the base for enhancing their hole-transporting capability.[78,79] These low molecular weight compounds tend to be less stable due to their complex molecular structure and added dopants.[6] Conversely, the hole-transporting polymers with high hole mobility have been applied as a comparatively thin layer of ca. 10–20 nm with the minimum dopants of LiTFISI, and generally showed a high structural stability.[80,81] However, these hole-transporting polymers have a high production cost due to their multi-step synthetic processes.

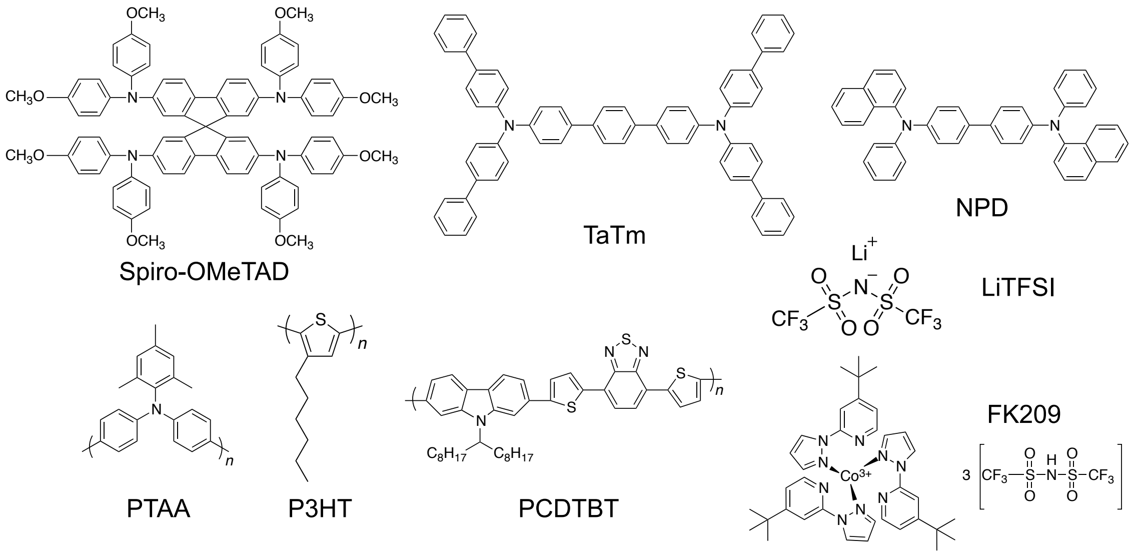

Figure 1.6 Molecular structures of organic compounds for the HTM of *n-i-p* cells and dopants.

Finally, metals with a high conductivity, superior light reflectivity, and appropriate Fermi levels, such as gold (Au) and silver (Ag), can be used as counter electrodes. In this thesis, *n-i-p* configured cells were used in Chapter 2, 3, and a part of Chapter 5.

In the *p-i-n* configuration, cells are fabricated in the following order: TCO, HTL, a perovskite layer, ETL, and a counter electrode.[82] Poly(3,4-ethylenedioxythiophene) doped with poly(4-styrenesulfonate) (PEDOT:PSS) is the most representative HTL of *p-i-n* cells due to its insolubility in the perovskite precursor solution of DMF and DMSO.[73,83] Moreover, PEDOT:PSS has generally been used as an aqueous dispersion; therefore, the formed layer does not repel the perovskite precursor solution. Inorganic semiconductors, such as nickel oxide (NiOx), have also been applied to the HTL.[84] While, [6,6]-phenyl-$C_{61}$-butyric acid methyl ester (PCBM) and 2,9-dimethyl-4,7-diphenyl-1,10-phenanthroline (BCP) have often been applied to the ETL of *p-i-n* cells due to their solubility in chlorobenzene, chloroform, and toluene (solvents which do not dissolve the perovskite layer). Additionally, zinc oxide (ZnO) or aluminum-doped zinc oxide (AZO) have been applied as a buffer layer.[85,86] Silver (Ag) or aluminum (Al) has often been selected as counter electrodes due to having deeper Fermi levels than Au.[87] In this thesis, *n-i-p* configured cells were selected in Chapter 4.

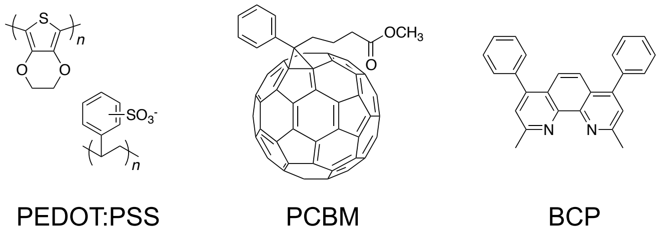

Figure 1.7 Molecular structures of organic compounds for *p-i-n* cells.

A further proposed cell configuration is an HTL-free perovskite solar cell fabricated with a *p*-doped perovskite layer.[88] Structural optimizations such as perovskite compositions, e.g., the addition of a small excess of $PbI_2$, and the introduction of the buffer layer to alleviate heteroepitaxy crystal growth due to dissociation of the lattice constant between the perovskite layer and under layers, have also been suggested by some groups.[89,90]

### 1.2.4 Perovskite-based tandem solar cells

The cost of silicon solar cells has decreased over the past years, which makes an improvement in the photovoltaic conversion efficiency of the cells a simple but effective solution for enhancing the value of the solar cells. Stacking two or more different types of solar cells with different light-absorbing wavelengths (related to their band gaps) as “tandem solar cells” is a simple but profound method to enhance the total photovoltaic conversion efficiency.[91] Perovskite solar cells are suitable candidates as components of tandem solar cells. For example, perovskite/silicon tandem cells were shown to have a 28.0% efficiency, and perovskite/perovskite tandem solar cells also gave an efficiency of 24.8%.[92] They have endeavored to achieve an extremely high photovoltaic conversion efficiency of over 30% owing to the adjustability of the band gap (1.5−1.8 eV) by the selection of perovskite compositions (Figure 1.8).[24]

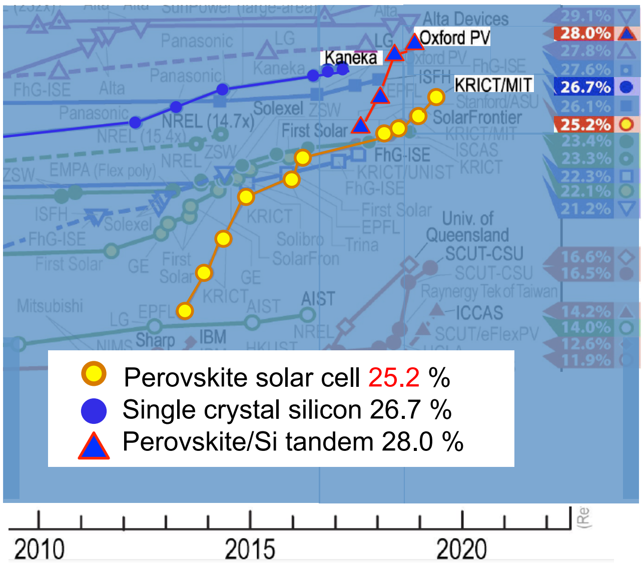

Figure 1.8 NREL chart focusing on perovskite/silicon tandem solar cells.[24]

Two terminal (2T) and four terminal (4T) configurations have been proposed for tandem solar cells (Figure 1.9).[93] The 2T configuration possesses two types of light-absorbing layers and each charge-transporting or -blocking layer is located on one cell. The $V_{OC}$ of the 2T cells is fundamentally a simple sum of that of two light-absorbing layers.[94] On the other hand, the $J_{SC}$ of the cells is determined by bulk and junction resistances of all materials and interfaces.[94] Despite the difficulty of the strict control of band alignment and physical matching between interlayers to obtain highly efficient cells, the 2T cells have received interest due to advantages in their facile manufacturing processes. A recombination layer has often been used for aligning the energy bands of entire cells (Figure 1.10).[95] The 4T-configured cells are fabricated by the simple stacking of two complete cells. The transparent conductive layer is placed between these two complete cells to take photocurrent out and is the same as connecting two separate cells in parallel.

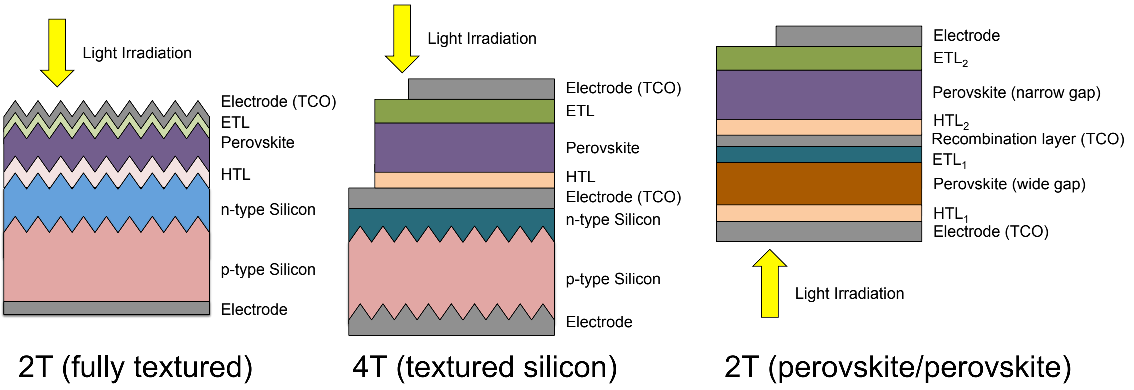

2T (fully textured) 4T (textured silicon) 2T (perovskite/perovskite)

Figure 1.9 Configurations of tandem solar cells with 2T and 4T structures.

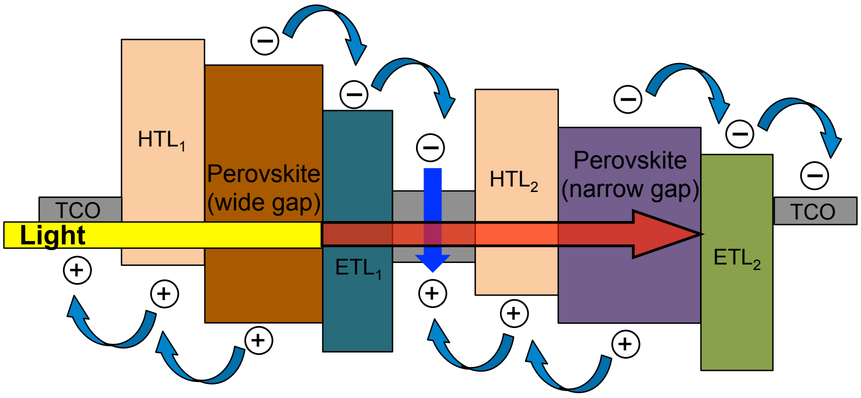

Figure 1.10 Band alignment of a perovskite/perovskite tandem solar cell.

Front side textured structures have been suggested to enhance the photovoltaic conversion efficiency of not only silicon solar cells themselves but also tandem solar cells.[96] Textured silicon substrates have micrometer-scale pyramidal structures to suppress surface light reflection and redirect light into the silicon cells to enhance the photocurrent (Figure 1.11).[97] The textured structure is created by etching processes using basic solvents; therefore, other layers, including the charge-transporting layer and electrodes, should be stacked after the formation of the textured structures. A limitation regarding applicable materials for the textured under layers is one of the crucial problematic issues because the solution processes cannot be applied. Tandem cells with three light-absorbing layers (silicon, narrow gap perovskite, and wide gap perovskite) have also been reported. Therefore, the discovery of materials that can be applied to the textured cells has become more important.

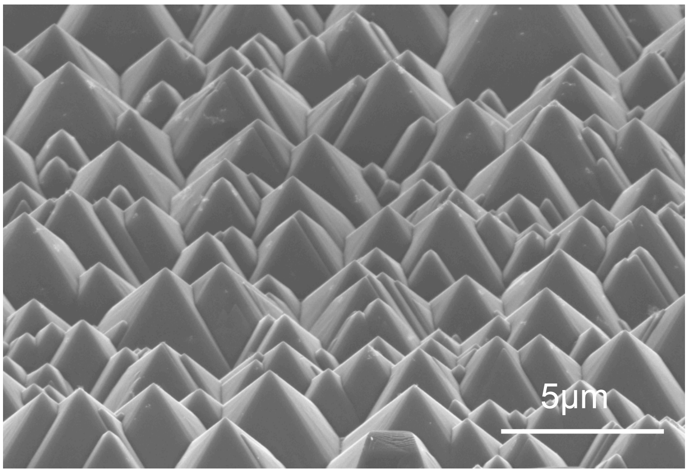

Figure 1.11 Surface SEM image of a textured silicon substrate obtained through a scanning electron microscope of the Fraunhofer Institute for Solar Energy Systems.

## 1.3 Charge-Transporting Polymers

### 1.3.1 Organic charge-transporting materials

Organic charge-transporting materials including low molecular weight charge-transporting materials and polymers are characterized as lightweight, bendable, and facile film formability using solution processes, which are not found in conductive inorganic materials such as metals.[18,34,98] Furthermore, organic charge-transporting materials can roughly be categorized into $p$- and $n$-types according to their carriers of hole or electron, and have been used for organic electric and photoelectric devices such as organic transistors, memories, and solar cells.[99,100] To further improve the functions of organic charge-transporting materials, research into their molecular alignment has actively been conducted using liquid crystals, self-organization, and additional molecular designs.[90,100] Notably, the required energy levels differ depending on the specific devices in actual application. Conductivity, one of the most important parameters of organic charge-transporting materials, is defined by the following equation (Eq. 1.2).[101]

$$\sigma = en\mu \quad \text{(Eq. 1.2)}$$

$\sigma$: conductivity (S/cm), $e$: elementary charge (C), $n$: carrier density (/cm$^3$), $\mu$: carrier mobility (cm$^2$/Vs)

Important factors for determining the conductivity of organic hole-transporting materials are carrier density and carrier mobility.[101] Chemical doping using oxidants has commonly been applied to increase the carrier density. Since carrier mobility is derived from the molecular structure and morphology of the formed film, the molecular design, such as the introduction of bulky substitutes, exclusion of alkyl side chains, or adjustment of π-conjugate length, is the most important factor for enhancing carrier mobility.[101]

Organic materials that are applied to organic devices as a thin film are classified with their molecular weight, and are specifically selected based on the device in use and their characteristics. These low molecular weight materials generally exist as agglutinates with weak intermolecular interactions. Therefore, they are soluble in various organic solvents and able to form homogeneous layers by facile wet processes such as spin-coating or casting methods. They are also deposited in dry processes such as vapor phase evaporation to form high-quality thin films.[102] The low molecular weight materials tend to form crystal structures with structural defects between the grains, which work as carrier traps to decrease the charge-transporting capability.[98] Materials that form isotropic and homogeneous amorphous thin films have been developed to reduce the crystallinity of the molecules by introducing a non-planar structure or bulky substituents.[103] The most commonly used hole-transporting material for perovskite solar cells, spiro-OMeTAD, is also included in this category. This material has a three-dimensional "spiro" structure with a quaternary carbon atom, which improves bulkiness and decreases the crystallinity (Figure 1.12). However, this type of bulky molecular structure generally shows steric instability and is associated with tedious synthetic steps.[6]

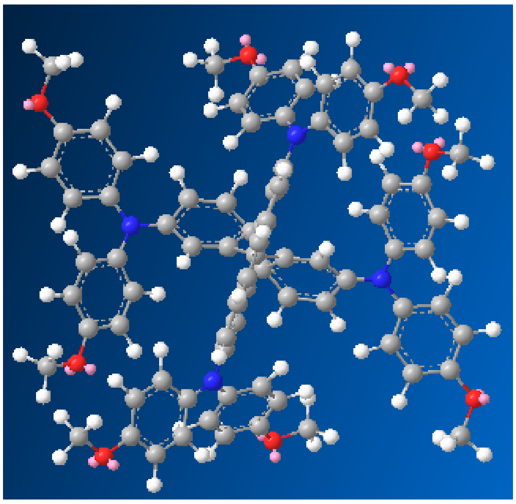

Figure 1.12 3D chemical structure of spiro-OMeTAD calculated by Molecular Mechanics program 2 (MM2).

Compared to the low molecular weight materials, polymers are more difficult to apply to dry film forming processes using an evaporation method due to their high molecular weight and the strong intermolecular interactions between long polymer chains.[104,105] Charge-transporting polymers are also not suitable for the formation of films in solution processes if no molecular designs are executed for enhancing their solvent-solubility.[106] Despite these challenges, charge-transporting polymers have significant potential in terms of their effective charge-transporting capability, thin film formability, and their structural stability for practical applications. In this thesis, several solutions for film formation methods will be proposed, including the improvement in solubility by introducing an alkyl side chain or a non-conjugated structure into the main chain, and in-situ polymerization on a substrate surface.

### 1.3.2 Charge-transporting conjugated polymers

Charge-transporting conjugated polymers, such as polythiophene and polyarylamine, have been widely investigated as components of various organic electric devices since the discovery of the conductivity of polyacetylene by Shirakawa *et al.* in the 1970's.[107] The carrier transfer of conjugated polymers is conducted through polaron and bipolaron structures generated by the chemical doping of π-conjugated units (Figure 1.13).[108]

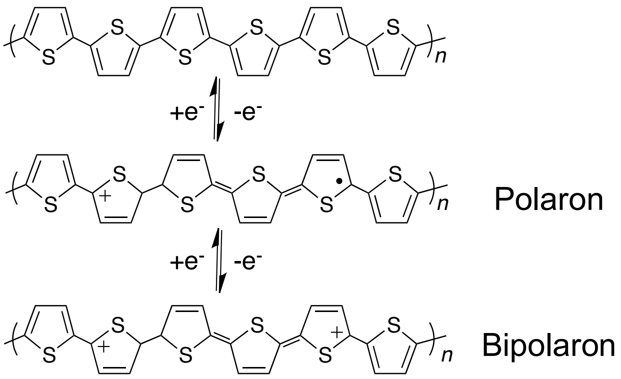

Figure 1.13 Polaron and bipolaron structures of poly(thiophene).

The intramolecular carrier transporting ability of these polymers is more effective than that of low molecular hole-transporting materials because of the wide delocalization of the carrier in the long π-conjugated structure. For example, PEDOT:PSS exhibits a conductivity of $10^0$ S/cm, which is close to that of inorganic conductors.[109]

However, conjugated polymers also have the disadvantages of high crystallinity and poor solvent-solubility in organic electric device applications due to their high flatness and strong intermolecular interactions. The introduction of long alkyl side chains such as poly(3-hexylthiophene) (P3HT) and poly(4-butyltriphenylamine) (PolyTPD) as well as the construction of non-planar structures using substituents such as poly[bis(4-phenyl)(2,4,6-trimethylphenyl)amine] (PTAA) have been proposed as solutions.[51,99] However, saturated hydrocarbons decrease the entire mobility, and the non-planar structures are usually difficult to be synthesized due to the steric hindrance.

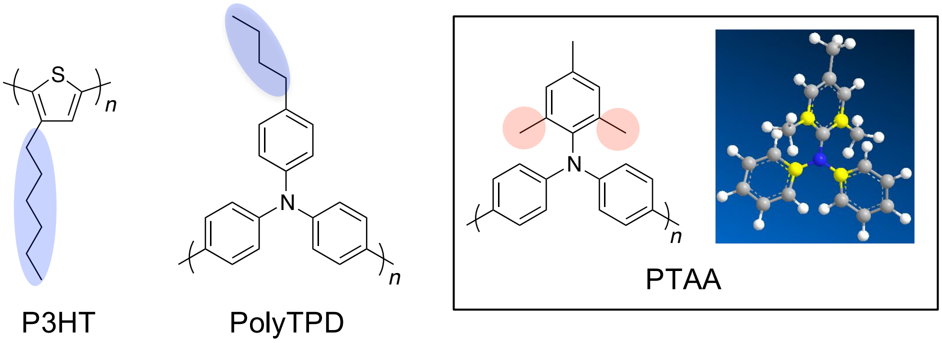

Figure 1.14 Molecular structures of conjugated polymers with alkyl side chains and non-planar structures.

### 1.3.3 Charge-transporting non-conjugated polymers

Charge-transporting non-conjugated polymers, in which redox groups are introduced into a non-conjugated backbone as side chains, conduct a charge-transport based on a chemical redox between the side chain units (Eq. 1.4).

$$\mathrm{M} + \mathrm{M}^{+} \rightleftarrows \mathrm{M}^{+} + \mathrm{M} \ (\mathrm{Eq.\,1.4})$$

Intermolecular hopping dominates the conduction due to the missing π-conjugated long pathway. The orbital overlap between the units tends to be small because the charge is strongly localized within the redox units. Therefore, unit density and side chain length, which determine the motion region of the units, are extremely important in molecular designs. The charge-transporting non-conjugated polymers with various side chains, such as poly(vinyltriarylamine), poly(vinyl-*p*-benzoquinone), and poly(1-oxy-2,2,6,6-tetramethylpiperidin-4-yl methacrylate) have been proposed.[110–112]

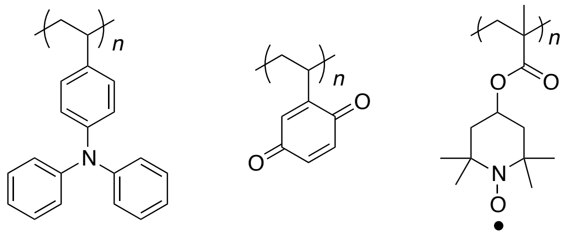

Figure 1.15 Examples of charge-transporting non-conjugated polymers.

High solubility due to flexible main chain structures is an advantage for the device application. The flexible main chain structure of non-conjugated polymers achieves an amorphous film formation to avoid creating defects in grain boundaries. Furthermore, an improvement in the glass transition temperatures of the polymers is also possible for the same reason.

Organic radical-bearing polymers, which play a significant role in this thesis, with a representative organic redox group of TEMPO have been applied as the charge transporting and storing materials of secondary batteries (Figure 1.16).[113,114] The charge-transporting capability of TEMPO polymers in a solid state via a hopping conduction between TEMPO substituents has also been described, for example, as a solid-type organic memory.[115,116] Recently, Boudouris *et al.* also reported the high charge-transporting capability of the TEMPO polymer.[117]

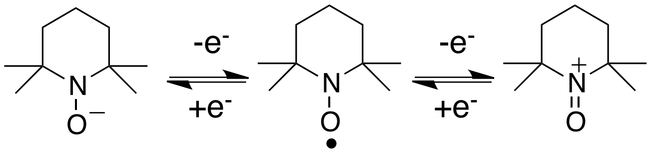

Figure 1.16 Redox reaction of the TEMPO moiety.

## 1.4 Interfacial Engineering of Perovskite Solar Cells with Polymers

### 1.4.1 Surface passivation of the perovskite layer

One of the most important factors for enhancing the photovoltaic performance of perovskite solar cells is the formation of a high-quality perovskite layer. Perovskite layers prepared by general solution methods are polycrystalline layers with a particle size of tens to hundreds of nanometers that include defects at the boundaries of the perovskite grains.[118] These defects are caused by strain fields and/or lattice defects due to ion migration in which atoms missing from the lattice of the perovskite crystals and working as carrier traps decrease the photovoltaic performance of the cells.[119,120]

The defect density of the perovskite layer is relatively low at $10^{15}$–$10^{16}$ $cm^{-3}$ compared to other polycrystalline materials, due to the structural optimization by annealing even at room temperature.[121] In other words, the relaxation energy of the defects is lower than the generation energy of the defects; therefore, the defects can be filled automatically if there are enough replenishment materials around them.[121] This phenomenon is defined as “passivation” following a word of silicon solar cells.[122]

Typical materials used for the passivation of the perovskite layer are alkylammonium halides, such as formamidine hydroiodide and guanidine hydrobromide, that react with the remaining $PbI_2$ on the perovskite surface to sequentially form new perovskite compounds.[123,124] These additional perovskite compounds exhibit positive synergies. For example, a new perovskite thin layer with tuned energy levels could work as an electron-blocking layer for more efficient charge extraction. Another example is a two-dimensional perovskite layer formed by alkylammonium halide with a long alkyl chain, which could make the cells more water-repellent.[10,125] Additionally, the passivation by organic compounds or polymers, such as poly(methylmethacrylate) (PMMA) and poly(propylene carbonate) (PPC), has also been shown to further improve the performance of the cell.[11,126] Although "passivation" has a lot of meanings, the method often refers to highly efficient cells with the defect-compensated perovskite layers.

### 1.4.2 Polymer incorporation in the perovskite precursor solution as a scaffold

Polymers have also been utilized as effective scaffolds for enhancing the quality of perovskite layers by simply adding them to the perovskite precursor solution.[127,128] The formation of perovskite layers can be considered to involve two separate processes, crystal nucleation and crystal growth. For the first process, the incorporation of the polymer additives decreases the surface energy of the crystal and Gibbs free energy to promote crystal nucleation that is caused by impure additives of the heterogeneous nucleation process and simultaneously occurs over the entire phase (Figure 1.17).[126]

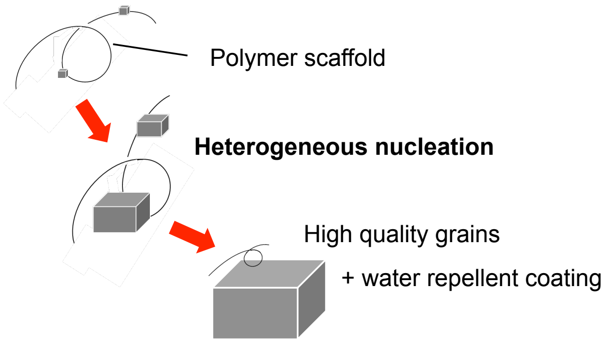

Figure 1.17 Schematic diagram of perovskite crystal growth with the incorporation of a polymer additive.

For the second process, polymers composed of ether, ester, or amine moiety, such as PMMA, PPC, poly(ethylene glycol) (PEG), and polyethyleneimine (PEI), interact with $PbX_2$ (a perovskite precursor) to decrease the growth rate of the nuclei produced by the above crystal nucleation step (Figure 1.18).[129,130] In conclusion, these two steps promote crystal nucleation and slow crystal growth, thereby, forming a homogeneous and the high quality perovskite crystal layer with large grains and fewer grain boundaries. The remaining polymers in the formed perovskite layer may also contribute to the surface passivation of the perovskite grains and to building a water-repellent coating for high durability.

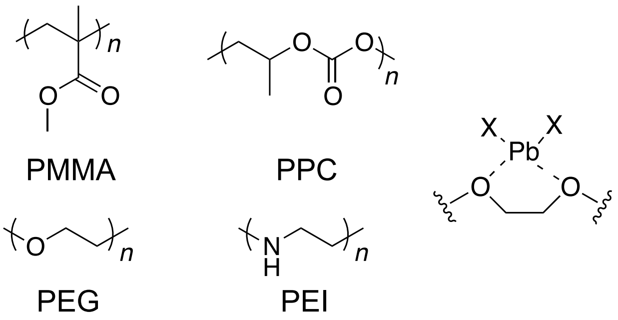

Figure 1.18 Molecular structures of the polymers and their interactions with $PbX_2$.

Along the above-mentioned background, charge-transporting polymers have the potential to improve the photovoltaic performance, the durability, and fabrication process of the perovskite solar cells by applying them as effective hole-transporting layers and a scaffold for the perovskite layer formation.

In this thesis, the author focuses on both charge-transporting polymers and the interfaces of the perovskite solar cells. The following three significant methodologies are suggested for obtaining highly efficient and usable solar cells: a innovative molecular design for hole-transporting materials, the application of redox polymers as scaffolds, and the formation of a homogeneous and durable polymer layer via an evaporation process.

First, arylamine derivatives and their addition condensation as a polymerization method are, for the first time, used to prepare robust, effective, and highly soluble hole-transporting polymers through a simple synthetic process. Second, a charge-transportable TEMPO polymer is firstly used as both an effective scaffold for forming high-quality perovskite grains without the reduction of the photocurrent, and as an eliminating agent of superoxide anion radical to enhance cell durability. Third, a thiophene polymer is applied to evaporated perovskite solar cells, resulting in a durable HTL even on textured substrates via an in-situ vapor phase polymerization method.

The author anticipates that this interfacial engineering approach utilizing organic polymers will certainly lead the perovskite solar cell to a game-changer in the field of photovoltaic devices.

## References

[1] A. Kojima, K. Teshima, Y. Shirai, T. Miyasaka, *J. Am. Chem. Soc.* **2009**, *131*, 6050–6051.

[2] J. H. Heo, S. H. Im, J. H. Noh, T. N. Mandal, C. Lim, J. A. Chang, Y. H. Lee, H. Kim, A. Sarkar, M. K. Nazeeruddin, et al., *Nat. Photonics* **2013**, *7*, 486–491.

[3] M. Liu, M. B. Johnston, H. J. Snaith, *Nature* **2013**, *501*, 395–398.

[4] H. S. Kim, C. R. Lee, J. H. Im, K. B. Lee, T. Moehl, A. Marchioro, S. J. Moon, R. Humphry-Baker, J. H. Yum, J. E. Moser, et al., *Sci. Rep.* **2012**, *2*, 1–7.

[5] M. I. Asghar, J. Zhang, H. Wang, P. D. Lund, *Renew. Sustain. Energy Rev.* **2017**, *77*, 131–146.

[6] S. Ameen, M. A. Rub, S. A. Kosa, K. A. Alamry, M. S. Akhtar, H. S. Shin, H. K. Seo, A. M. Asiri, M. K. Nazeeruddin, *ChemSusChem* **2016**, *9*, 10–27.

[7] M. Saliba, T. Matsui, J. Y. Seo, K. Domanski, J. P. Correa-Baena, M. K. Nazeeruddin, S. M. Zakeeruddin, W. Tress, A. Abate, A. Hagfeldt, et al., *Energy Environ. Sci.* **2016**, *9*, 1989–1997.

[8] S. S. Reddy, K. Gunasekar, J. H. Heo, S. H. Im, C. S. Kim, D. H. Kim, J. H. Moon, J. Y. Lee, M. Song, S. H. Jin, *Adv. Mater.* **2016**, *28*, 686–693.

[9] J. Idígoras, F. J. Aparicio, L. Contreras-Bernal, S. Ramos-Terrón, M. Alcaire, J. R. Sánchez-Valencia, A. Borras, Á. Barranco, J. A. Anta, *ACS Appl. Mater. Interfaces* **2018**, *10*, 11587–11594.

[10] Y. Cho, A. M. Soufiani, J. S. Yun, J. Kim, D. S. Lee, J. Seidel, X. Deng, M. A. Green, S. Huang, A. W. Y. Ho-Baillie, *Adv. Energy Mater.* **2018**, *1703392*.

[11] T. Han, J. Lee, C. Choi, S. Tan, C. Lee, Y. Zhao, Z. Dai, N. De Marco, S. Lee, S. Bae, et al., *Nat. Commun.* **2019**, *10*, 1–10.

[12] M. Anaya, G. Lozano, M. E. Calvo, H. Miguez, *Joule* **2017**, *1*, 769–793.

[13] G. Nogay, F. Sahli, J. Werner, R. Monnard, M. Boccard, M. Despeisse, F. Haug, Q. Jeangros, A. Ingenito, C. Ballif, et al., *ACS Energy Lett.* **2019**, 844–845.

[14] Q. Wali, N. K. Elumalai, Y. Iqbal, A. Uddin, R. Jose, *Renew. Sustain. Energy Rev.* **2018**, *84*, 89–110.

[15] P. Shen, Y. Chiang, M. Li, T. Guo, P. Chen, P. Shen, Y. Chiang, M. Li, T. Guo, *APL Mater.* **2016**, *4*, 091509.

[16] L. Cojocaru, K. Wienands, T. W. Kim, S. Uchida, A. J. Bett, S. Rafizadeh, J. C. Goldschmidt, S. W. Glunz, *ACS Appl. Mater. Interfaces* **2018**, *10*, 26293–26302.

[17] G. Longo, C. Momblona, M.-G. La-Placa, L. Gil-Escrig, M. Sessolo, H. J. Bolink, *ACS Energy Lett.* **2018**, *3*, 214–219.

[18] V. Coropceanu, J. Cornil, D. A. da Silva Filho, Y. Olivier, R. Silbey, J. L. Brédas, *Chem. Rev.* **2007**, *107*, 926–952.

[19] X. Guo, M. Baumgarten, K. Müllen, *Prog. Polym. Sci.* **2013**, *38*, 1832–1908.

[20] K. Oyaizu, H. Nishide, *Adv. Mater.* **2009**, *21*, 2339–2344.

[21] H. Nishide, K. Oyaizu, *Science* **2008**, *319*, 737–738.

[22] M. A. Green, *J. Mater. Sci.* **2007**, *18*, S15-19.

[23] T. Markvart, L. Castaner, in *Sol. Cells Mater. Manuf. Oper.* (Eds.: A. McEvoy, L. Castaner, T. Markvart), Elsevier Science & Technology, **2013**, pp. 3–68.

[24] NREL Chart: The plot is not copyrighted owing to the courtesy of the National Renewable Energy Laboratory, Golden, Co.

[25] M. A. Green, *Prog. Photovoltaics Res. Appl.* **2009**, *17*, 183–189.

[26] A. V. Shah, H. Schade, M. Vanecek, J. Meier, E. Vallat-Sauvain, N.Wyrsch, U. Kroll, C. Droz, J. Bailat, *Prog. Photovoltaics Res. Appl.* **2004**, *12*, 113–142.

[27] F. Ferrazza, in *Sol. Cells Mater. Manuf. Oper.* (Eds.: A. McEvoy, L. Castaner, T. Markvart), Elsevier Science & Technology, **2013**, pp. 69–158.

[28] H. J. Hovel, in *Semicond. Semimetals Vol. Sol. Cells*, Academic Press, **1975**, pp. 181–224.

[29] D. Pysch, A. Mette, S. W. Glunz, *Sol. Energy Mater. Sol. Cells* **2007**, *91*, 1698–1706.

[30] P. Reinhard, P. Blasch, F. Pianezzi, S. Nishiwaki, S. Buecheler, A. N. Tiwari, *IEEE J. Photovoltaics* **2012**, 10.1109/PVSC-Vol2.2012.6656789.

[31] C. P. Muzzillo, *Sol. Energy Mater. Sol. Cells* **2017**, *172*, 18–24.

[32] V. S. Saji, I. Choi, C. Lee, *Sol. Energy* **2011**, *85*, 2666–2678.

[33] G. A. Chamberlain, *Sol. Cells* **1983**, *8*, 47–83.

[34] B. P. Rand, J. Genoe, P. Heremans, J. Poortmans, *Prog. Photovoltaics Res. Appl.* **2007**, *15*, 659–676.

[35] D. D. S. Fung, W. C. H. Choy, *Organic Solar Cells Materials and Device Physics*, Springer, **2013**.

[36] B. O. Regan, M. Gratzelt, *Nature* **1991**, *353*, 737–740.

[37] M. Grätzel, *J. Photochem. Photobiol. C Photochem. Rev.* **2003**, *4*, 145–153.

[38] J. Gong, J. Liang, K. Sumathy, *Renew. Sustain. Energy Rev.* **2012**, *16*, 5848–5860.

[39] B. Li, L. W. Ã, B. Kang, P. Wang, Y. Q. Ã, *Sol. Energy Mater. Sol. Cells* **2006**, *90*, 549–573.

[40] L. Xiong, Y. Guo, J. Wen, H. Liu, G. Yang, P. Qin, G. Fang, *Adv. Funct. Mater.* **2018**, *28*, 1–18.

[41] C. H. Ng, H. N. Lim, S. Hayase, Z. Zainal, N. M. Huang, *Renew. Sustain. Energy Rev.* **2018**, *90*, 248–274.

[42] A. K. Jena, A. Kulkarni, T. Miyasaka, *Chem. Rev.* **2019**, *119*, 3036–3103.

[43] G. Niu, X. Guo, L. Wang, *J. Mater. Chem. A* **2015**, *3*, 8970–8980.

[44] A. S. Bhalla, R. Guo, R. Roy, *Mterials Res. Innov.* **2016**, *4*, 3–26.

[45] W.-J. Yin, J.-H. Yang, J. Kang, Y. Yan, S.-H. Wei, *J. Mater. Chem. A* **2015**, *3*, 8926–8942.

[46] H. Fu, *Sol. Energy Mater. Sol. Cells* **2019**, *193*, 107–132.

[47] S. Pang, H. Hu, J. Zhang, S. Lv, Y. Yu, F. Wei, T. Qin, H. Xu, Z. Liu, G. Cui, *Chem. Mater.* **2014**, *26*, 1485–1491.

[48] M. Saliba, T. Matsui, J.-Y. Seo, K. Domanski, J.-P. Correa-Baena, M. K. Nazeeruddin, S. M. Zakeeruddin, W. Tress, A. Abate, A. Hagfeldtd, et al., *Energy Environ. Sci.* **2016**, *9*, 1989–1997.

[49] F. Bella, G. Griffini, J. P. Correa-Baena, G. Saracco, M. Grätzel, A. Hagfeldt, S. Turri, C. Gerbaldi, *Science* **2016**, *354*, 203–206.

[50] C. Wu, Q. Zhang, Y. Liu, W. Luo, X. Guo, Z. Huang, H. Ting, W. Sun, X. Zhong, S. Wei, et al., *Adv. Sci.* **2018**, *5*, 2–9.

[51] O. Malinkiewicz, C. Roldán-carmona, A. Soriano, E. Bandiello, L. Camacho, M. K. Nazeeruddin, H. J. Bolink, *Adv. Energy Mater.* **2014**, *4*, 1400345.

[52] Y. H. Park, I. Jeong, S. Bae, H. J. Son, P. Lee, J. Lee, C. H. Lee, M. J. Ko, *Adv. Funct. Mater.* **2017**, *27*, 21–27.

[53] T. Jesper Jacobsson, J. P. Correa-Baena, M. Pazoki, M. Saliba, K. Schenk, M.

Grätzel, A. Hagfeldt, *Energy Environ. Sci.* **2016**, *9*, 1706–1724.
[54] A. Dubey, N. Adhikari, S. Mabrouk, F. Wu, K. Chen, *J. Mater. Chem. A* **2018**, *6*, 2406–2431.
[55] W. Nie, H. Tsai, R. Asadpour, A. J. Neukirch, G. Gupta, J. J. Crochet, M. Chhowalla, S. Tretiak, M. A. Alam, H. Wang, *Science* **2015**, *347*, 522–526.
[56] M. Yavari, M. Mazloum-ardakani, S. Gholipour, M. Grätzel, A. Hagfeldt, M. Saliba, *Adv. Energy Mater.* **2018**, 1800177.
[57] S. Paek, P. Schouwink, E. N. Athanasopoulou, K. T. Cho, G. Grancini, Y. Lee, Y. Zhang, F. Stellacci, M. K. Nazeeruddin, P. Gao, *Chem. Mater.* **2017**, *29*, 3490–3498.
[58] J.-H. Im, I.-H. Jang, N. Pellet, M. Grätzel, N.-G. Park, *Nat. Nanotechnol.* **2014**, *9*, 927–932.
[59] G. Zhou, J. Wu, Y. Zhao, Y. Li, J. Shi, Y. Li, H. Wu, D. Li, Y. Luo, Q. Meng, *ACS Appl. Mater. Interfaces* **2018**, *10*, 9503–9513.
[60] T. M. Schmidt, T. T. Larsen-olsen, J. E. Carlé, D. Angmo, F. C. Krebs, *Adv. Energy Mater.* **2015**, *5*, 1500569.
[61] M. Yang, Z. Li, M. O. Reese, O. G. Reid, D. H. Kim, S. Siol, T. R. Klein, Y. Yan, J. J. Berry, M. F. A. M. Van Hest, et al., *Nat. Energy* **2017**, *2*, 17038.
[62] R. Kottokkaran, H. A. Gaonkar, H. A. Abbas, M. Noack, V. Dalal, *J. Mater. Chem. A Mater. Electron.* **2019**, *30*, 5487–5494.
[63] T. Abzieher, S. Moghadamzadeh, F. Schackmar, H. Eggers, F. Sutterlüti, A. Farooq, D. Kojda, K. Habicht, R. Schmager, A. Mertens, et al., *Adv. Mater.* **2019**, *1802995*.
[64] D. Zhao, W. Ke, C. R. Grice, A. J. Cimaroli, X. Tan, M. Yang, R. W. Collins, H. Zhang, K. Zhu, Y. Yan, *Nano Energy* **2016**, *19*, 88–97.
[65] J. Avila, C. Momblona, P. Boix, M. Sessolo, M. Anaya, G. Lozano, K. Vandewal, H. Mıguez, H. J. Bolink, *Energy Environ. Sci.* **2018**, *11*, 3292–3297.
[66] R. Wang, M. Mujahid, Y. Duan, Z. Wang, J. Xue, *Adv. Funct. Mater.* **2019**, *1808843*.
[67] F. Giordano, A. Abate, J. P. Correa Baena, M. Saliba, T. Matsui, S. H. Im, S. M. Zakeeruddin, M. K. Nazeeruddin, A. Hagfeldt, M. Graetzel, *Nat. Commun.* **2016**, *7*, 10379.
[68] F. T. F. O'Mahony, Y. H. Lee, C. Jellett, S. Dmitrov, D. T. J. Bryant, J. R. Durrant, B. C. O'Regan, M. Graetzel, M. K. Nazeeruddin, S. A. Haque, *J. Mater. Chem. A* **2015**, *3*, 7219–7223.
[69] Q. Jiang, L. Zhang, H. Wang, X. Yang, J. Meng, H. Liu, Z. Yin, J. Wu, X. Zhang, J. You, *Nat. Energy* **2017**, *1*, 16177.
[70] S. Song, G. Kang, L. Pyeon, C. Lim, G. Y. Lee, T. Park, J. Choi, *ACS Energy Lett.* **2017**, *2*, 2667–2673.
[71] Q. Jiang, X. Zhang, J. You, *Small* **2018**, *14*, 1–14.
[72] S. S. Mali, J. V. Patil, H. Arandiyan, C. K. Hong, *J. Mater. Chem. A* **2019**, *7*, 17516–17528.
[73] C. Momblona, L. Gil-Escrig, E. Bandiello, E. M. Hutter, M. Sessolo, K. Lederer, J. Blochwitz-Nimoth, H. J. Bolink, *Energy Environ. Sci.* **2016**, *9*, 3456–3463.
[74] W. Gao, A. Kahn, *J. Appl. Phys.* **2003**, *94*, 359–366.
[75] Y. H. Lee, *Nat. Photonics* **2013**, *7*, 486–491.
[76] M. Abd, F. Aziz, A. Fauzi, W. Norharyati, W. Salleh, N. Yusof, J. Jaafar, T. Soga, M. Zainizan, N. Ahmad, *Appl. Mater. Today* **2018**, *13*, 69–82.
[77] Q. Wang, C. Bi, J. Huang, *Nano Energy* **2015**, *15*, 275–280.
[78] Z. Yu, L. Sun, *Adv. Energy Mater.* **2015**, *5*, 1500213.
[79] A. Dualeh, T. Moehl, N. Tétreault, J. Teuscher, P. Gao, M. K. Nazeeruddin, M. Grätzel, *ACS Nano* **2014**, *8*, 362–373.
[80] A. Isakova, P. D. Topham, *J. Polym. Sci. Part B Polym. Phys.* **2017**, *55*, 549–568.
[81] F. Yang, H. E. Lim, F. Wang, M. Ozaki, A. Shimazaki, J. Liu, N. B. Mohamed,

K. Shinokita, Y. Miyauchi, A. Wakamiya, et al., *Adv. Mater. Interfaces* **2018**, *5*, 1701256.
[82] W. Yan, S. Ye, Y. Li, W. Sun, H. Rao, Z. Liu, Z. Bian, C. Huang, *Adv. Energy Mater.* **2016**, *6*, 1–20.
[83] J. H. Heo, H. J. Han, D. Kim, T. K. Ahn, S. H. Im, *Energy Environ. Sci.* **2015**, *8*, 1602–1608.
[84] Y. Wang, X. Zheng, X. Liu, Y. Feng, H. Shan, L. Dong, G. Fang, Z. X. Xu, *Org. Electron. physics, Mater. Appl.* **2018**, *56*, 276–283.
[85] N. Shibayama, H. Kanda, T. W. Kim, H. Segawa, S. Ito, *APL Mater.* **2019**, *7*, 031117.
[86] D. B. Khadka, Y. Shirai, M. Yanagida, J. W. Ryan, K. Miyano, *J. Mater. Chem. C* **2017**, *5*, 8819–8827.
[87] L. Gil-Escrig, C. Momblona, D. Forgács, S. Pla, F. Fernández-Lázaro, M. Sessolo, Á. Sastre-Santos, H. J. Bolink, *Org. Electron. physics, Mater. Appl.* **2016**, *37*, 396–401.
[88] W. Wu, Q. Wang, Y. Fang, Y. Shao, S. Tang, Y. Deng, H. Lu, Y. Liu, T. Li, Z. Yang, et al., *Nat. Commun.* **2018**, 1625.
[89] D. Pérez-Del-Rey, P. P. Boix, M. Sessolo, A. Hadipour, H. J. Bolink, *J. Phys. Chem. Lett.* **2018**, *9*, 1041–1046.
[90] T. W. Kim, S. Uchida, T. Matsushita, L. Cojocaru, R. Jono, K. Kimura, D. Matsubara, M. Shirai, K. Ito, H. Matsumoto, et al., *Adv. Mater.* **2018**, *30*, 1705230.
[91] J. Wemer, F. Sahli, F. Fu, J. J. D. Leon, A. Walter, B. A. Kamino, B. Niesen, S. Nicolay, Q. Jeangros, C. Ballif, *ACS Energy Lett.* **2018**, *3*, 2052–2058.
[92] "Oxford PV, 'Oxford PV sets world record for perovskite solar cell' can be found under"https://www.oxfordpv.com/news/oxford-pv-sets-world-record-perovskite-solar-cell."
[93] C. O. R. Quiroz, Y. Shen, M. Salvador, K. Forberich, O. Ram, B. Wilkinson, T. Kirchartz, E. Spiecker, P. J. Verlinden, *J. Mater. Chem. A* **2018**, *6*, 3583–3592.
[94] L. Mazzarella, Y. H. Lin, S. Kirner, A. B. Morales-Vilches, L. Korte, S. Albrecht, E. Crossland, B. Stannowski, C. Case, H. J. Snaith, et al., *Adv. Energy Mater.* **2019**, *1803241*.
[95] H. Zhou, Q. Chen, G. Li, S. Luo, T. B. Song, H. S. Duan, Z. Hong, J. You, Y. Liu, Y. Yang, *Science* **2014**, *345*, 542–546.
[96] N. Tucher, O. Höhn, J. Murthy, J. C. Martinez, M. Steiner, A. Armbruster, E. Lorenz, B. Bläsi, J. C. Goldschmidt, *Opt. Express* **2019**, *27*, 1419–1430.
[97] N. Tucher, J. Eisenlohr, H. Gebrewold, P. Kiefel, H. Hauser, J. C. Goldschmidt, B. Bläsi, *Opt. Express* **2016**, *24*, 1083–1093.
[98] S. Hunter, J. Chen, T. D. Anthopoulos, *Adv. Funct. Mater.* **2014**, *24*, 5969–5976.
[99] Y. H. Lee, Y. P. Lee, C. J. Chiang, F. K. Wei, C. H. Wu, W. C. Chen, C. Shen, H. A. Jeng, L. Wang, M. W. Liu, et al., *J. Mater. Chem. A* **2014**, *2*, 14600–14612.
[100] J. Lee, A. R. Han, H. Yu, T. J. Shin, C. Yang, J. H. Oh, *J. Am. Chem. Soc.* **2013**, *135*, 9540–9547.
[101] N. Koch, in *Phys. Org. Semicond.* (Eds.: W. Brütting, C. Adachi), **2013**, pp. 35–64.
[102] B. Walker, A. B. Tamayo, X. D. Dang, P. Zalar, J. H. Seo, A. Garcia, M. Tantiwiwat, T. Q. Nguyen, *Adv. Funct. Mater.* **2009**, *19*, 3063–3069.
[103] H. Xiao, B. Leng, H. Tian, *Polymer* **2005**, *46*, 5707–5713.
[104] M. Gross, D. C. Müller, H.-G. Nothofer, U. Scherf, D. Neher, C. Bräuchle, K. Meerholz, *Nature* **2000**, *405*, 661–665.
[105] P. L. Qin, G. Yang, Z. W. Ren, S. H. Cheung, S. K. So, L. Chen, J. Hao, J. Hou, G. Li, *Adv. Mater.* **2018**, *30*, 1706126.
[106] J. Roncali, *Chem. Rev.* **1997**, *97*, 173–206.
[107] H. Derivatives, J. Louis, A. G. Macdiarmid, *J. Chem. Soc., Chem. Commun.* **1977**,

578–580.
[108] J. Yamamoto, Y. Furukawa, *J. Phys. Chem. B* **2015**, *119*, 4788–4794.
[109] A. M. Nardes, M. Kemerink, M. M. De Kok, E. Vinken, K. Maturova, R. A. J. Janssen, *Org. Electron.* **2008**, *9*, 727–734.
[110] W. Okada, T. Suga, K. Oyaizu, H. Segawa, H. Nishide, *ACS Appl. Energy Mater.* **2019**, *2*, 2848-2853.
[111] S. Kumar, Y. Choi, S. Kang, N. K. Oh, J. Lee, J. Seo, M. Jeong, H. W. Kwon, S. Il Seok, C. Yang, et al., *ACS Appl. Mater. Interfaces* **2019**, *11*, 38828–38837.
[112] D. C. Bobela, B. K. Hughes, W. A. Braunecker, T. W. Kemper, R. E. Larsen, T. Gennett, *J. Phys. Chem. Lett.* **2015**, *6*, 1414–1419.
[113] H. Nishide, S. Iwasa, Y. J. Pu, T. Suga, K. Nakahara, M. Satoh, *Electrochim. Acta* **2004**, *50*, 827–831.
[114] K. Nakahara, K. Oyaizu, H. Nishide, *Chem. Lett.* **2011**, *40*, 222–227.
[115] T. Suga, M. Sakata, K. Aoki, H. Nishide, *ACS Macro Lett.* **2014**, *3*, 703–707.
[116] Y. Yonekuta, K. Susuki, K. Oyaizu, K. Honda, H. Nishide, *J. Am. Chem. Soc.* **2007**, *129*, 14128–14129.
[117] S. H. Sung, B. M. Savoie, B. W. Boudouris, Y. Joo, V. Agarkar, *Science* **2018**, *359*, 1391–1395.
[118] Y. Zong, Y. Zhou, S. Pang, Y. Zong, Y. Zhou, Y. Zhang, Z. Li, L. Zhang, M. Ju, M. Chen, *Chem* **2018**, *4*, 1404–1415.
[119] B. Li, V. Ferguson, S. R. P. Silva, W. Zhang, *Adv. Mater. Interfaces* **2018**, 1800326.
[120] W.-J. Yin, T. Shi, Y. Yan, *Appl. Phys. Lett.* **2017**, *104*, 063903.
[121] A. Phys, M. Samiee, S. Konduri, B. Ganapathy, R. Kottokkaran, *Appl. Phys. Lett.* **2016**, *105*, 153502.
[122] A. G. Aberle, *Prog. Photovoltaics Res. Appl.* **2000**, *8*, 473–487.
[123] M. Wang, B. Li, J. Yuan, F. Huang, G. Cao, J. Tian, *ACS Appl. Mater. Interfaces* **2018**, *10*, 37005–37013.
[124] S. Wang, Y. Zhu, W. Sun, X. Miao, Z. Ma, C. Yang, B. Liu, S. Li, *Sol. Energy* **2018**, *176*, 118–125.
[125] Y. Hu, T. Qiu, F. Bai, W. Ruan, S. Zhang, *Adv. Energy Mater.* **2018**, 1703620.
[126] D. Bi, C. Yi, J. Luo, J. D. Décoppet, F. Zhang, S. M. Zakeeruddin, X. Li, A. Hagfeldt, M. Grätzel, *Nat. Energy* **2016**, *1*, 1–5.
[127] Y. Zhao, J. Wei, H. Li, Y. Yan, W. Zhou, D. Yu, Q. Zhao, *Nat. Commun.* **2016**, *7*, 1–9.
[128] A. Fakharuddin, M. Seybold, A. Agresti, S. Pescetelli, F. Matteocci, M. I. Haider, S. T. Birkhold, H. Hu, R. Giridharagopal, M. Sultan, et al., *ACS Appl. Mater. Interfaces* **2018**, *10*, 42542–42551.
[129] G. Yang, P. Qin, G. Fang, G. Li, *Sol. RRL* **2018**, 1800055.
[130] X. Cao, L. Zhi, Y. Li, F. Fang, X. Cui, Y. Yao, L. Ci, K. Dingd, J. Wei, *J. Mater. Chem. C* **2017**, *5*, 7458–7464.

# Chapter 2: Arylamine Polymers Prepared via Facile Paraldehyde-Addition Condensation as an Effective Hole-Transporting Material of Perovskite Solar Cells

## 2.1 Introduction

Arylamine derivatives and their polymers, especially triarylamine and phenylenediamine derivatives with wide $\pi$-conjugation, have often been applied as hole-transporting materials of electric or photoelectric devices, such as organic light-emitting diodes (OLEDs), organic field-effect transistors, and organic solar cells.[1–8] 2,2,7,7-Tetrakis(*N,N*-di-*p*-methoxyphenylamine)-9,9-spirobifluorene (Spiro-OMeTAD), the most representative hole-transporting material of perovskite solar cells, is also composed of four triarylamine units but is unstable for a practical use due to the highly reactive “spiro” substituent with a quaternary carbon atom and an addition of oxidative dopants.[9–12]

Hole-transporting polymers have also been tested as the hole-transporting layer without oxidizing agents, and exhibited high conversion efficiency and higher durability than low molecular weight hole-transporting materials owing to the stable molecular structure.[13–21] However, conductive arylamine polymers are still expensive to synthesis due to the multistep reaction including reductive couplings and twisted molecular structure for improving the low solubility in organic solvents due to their long $\pi$-conjugated structures.[22–25] For example, poly[bis(4-phenyl)(2,4,6-trimethylphenyl)amine] (PTAA), which is a representative commercially available triarylamine polymer used for the hole-transporting layer, has been prepared via multistep monomer preparation and reductive coupling polymerization using expensive rare-metal catalysts.[26–29] Methyl groups at 2- and 6-positions create twisting structure for improving its solubility. The reasonable molecular design and facile preparation of new arylamine polymers remain a topic of studies.[30–33]

Addition condensation is a famous and classical, but profound polymerization reaction, in which aromatic derivatives and aldehydes are reacted under moderate conditions to give thermosetting resins.[34–40] One of the characteristics of the polymers given by the addition condensation is easy purification by only removing the acidic or basic catalyst and the remaining amines and aldehydes.[41,42] One of the most important characteristics of addition condensation is relationship between the reaction condition and the given polymer structure: acidic condition gives rate-determining step of addition and aromatic end-groups, and basic condition gives rate-determining step of condensation and alcohol end-groups.[34,43] In acidic condition, the higher acidity promotes the reaction in *p*-position and suppresses the reaction in *o*-position, which is an another characteristic.[34] Phenolic resins with molecular weights of 1000 or less have often been obtained via addition condensation due to the trifunctional structure of the monomer: phenol.[44,45] On the other hand, arylamine derivatives, which are the difunctional structure, are needed to give polymers with both a high molecular weight and high solvent-solubility to form homogeneous thin films.[46] For example, poly(4-methyltriphenylamine-*co*-acetoaldehyde) (TPA-AA) with a molecular weight of $7.6 \times 10^4$ via addition condensation has been examined as a hole-transporting layer in OLEDs. [47]

In this chapter, new arylamine polymers, which could be prepared via a simple one-pot addition condensation reaction, were designed and yielded amorphous and stable hole-transporting polymers thin layer with tunable energy levels and high glass transition temperatures. The polymers exhibited appropriate HOMO levels as hole-transporting layers of the perovskite solar cells. The phenylenediamine structure with longer π-conjugation and methyl and methoxy (electron-donating) substituents were also introduced to the polymers for tuning their energy levels.[48–50] Paraldehyde was selected as a monomer of the addition condensation owing to the high reactivity and the small molecular structure as an aldehyde unit for realizing the highly soluble and hole-transportable polymers (Scheme 2.1).[51] The reaction condition including the feed ratio of arylamines and paraldehyde, reaction time, and temperature were severely tuned for increasing the molecular weight of the polymers. The perovskite solar cells fabricated with the arylamine polymers as the hole-transporting layers exhibited high photovoltaic conversion efficiency of over 16 % and high durability.

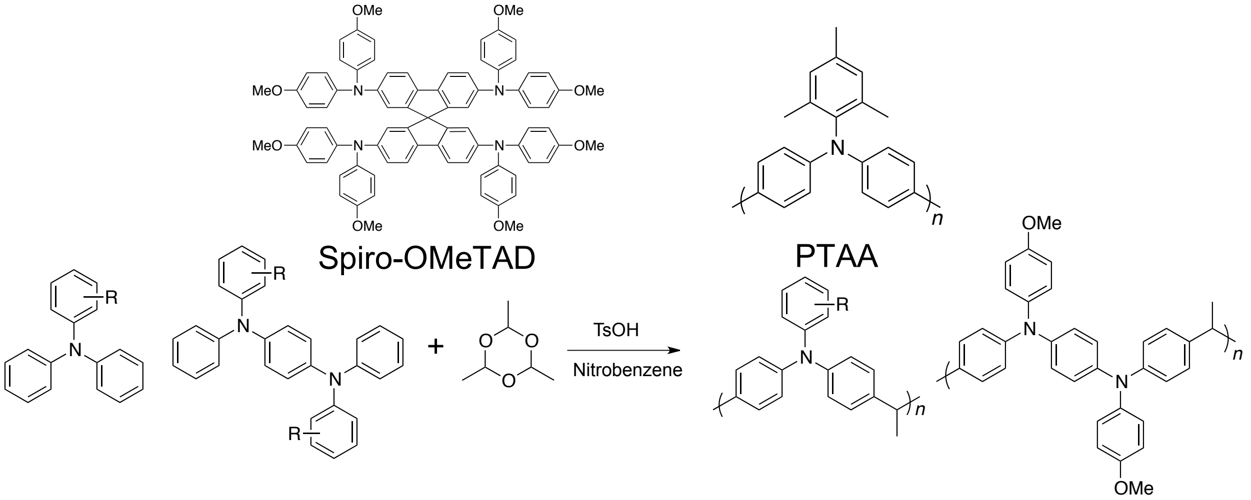

Scheme 2.1 Addition condensation of arylamine derivatives and a paraldehyde.

## 2.2 Addition Condensation of Arylamine Derivatives and a Paraldehyde

### 2.2.1 Monomer preparation

Arylamine monomers with tuned energy levels are necessary for a preparation of appropriate hole-transporting polymers as hole-transporting materials of the perovskite solar cells. Electron-donating methyl or methoxy substituents were introduced to triarylamine monomers via Buchwald-Hartwig reaction (Scheme 2.2).[32,52,53] Methoxy substituent worked as an electron-donating group at *o*- and *p*-position and as an electron-accepting group at *m*-position, which realized detailed energy levels tuning (by Hammet equation[54,55]). These substituents worked as not only energy level tuners but also molecular structure twisters. For example, 2,4,6-trimethyltriphenylamine showed a larger dihedral angle (55°) than 4-methyltriphenylamine's one (42°), which easily gave highly soluble polymers and amorphous polymer films.

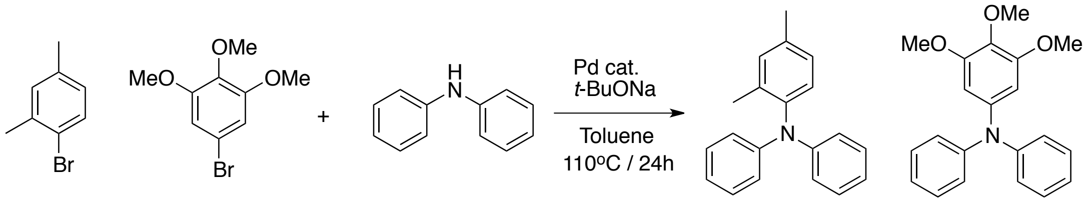

Scheme 2.2 Buchwald-Hartwig reactions of aryl bromide and secondary amines.

Phenylenediamine derivatives with a longer π-conjugated length than triarylamine generates bipolaron in a single unit, which might give higher hole mobility and shallower HOMO levels. Methyl- or methoxy-substituents could also be introduced to phenylenediamine monomers for energy level tuning by Buchwald-Hartwig reaction. On the other hand, the problem of synthesizing phenylenediamine monomers was the difficulty of purification due to intermediate products. The yields of the monomers were only 8 % of *N*,*N*′-diphenyl-*N*,*N*′-bis(2,4-dimethylphenyl)-1,4-phenylenediamine and 29 % of *N*,*N*′-diphenyl-*N*,*N*′-bis(4-methoxylphenyl)-1,4-phenylenediamine, respectively (Scheme 2.3). Finally, seven kinds of arylamine monomers were prepared (Figure 2.1)

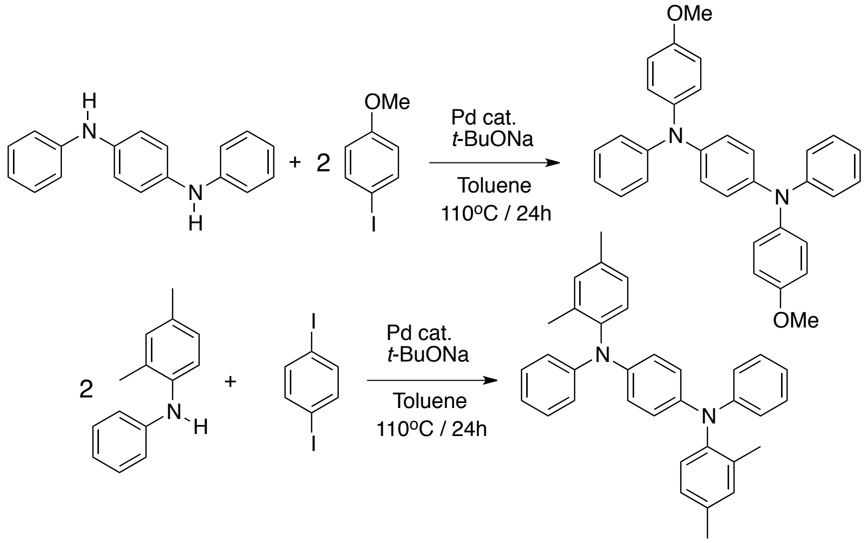

Scheme 2.3 Buchwald-Hartwig reactions of aryl iodide and secondary amines.

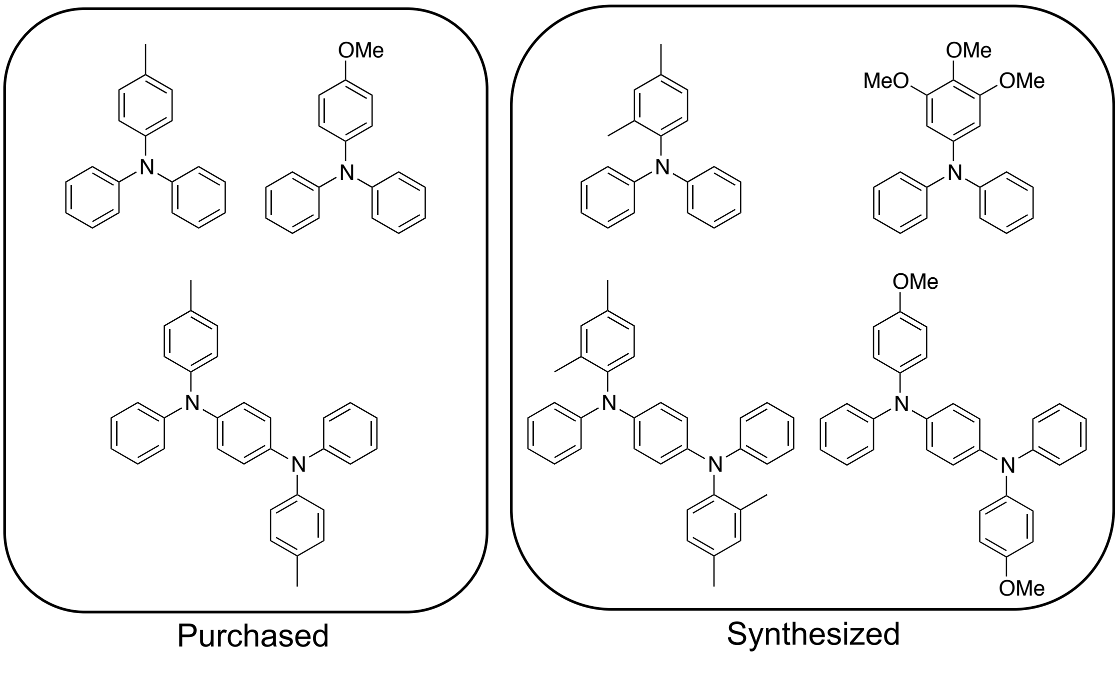

Figure 2.1 Prepared seven kinds of arylamine monomers.

### 2.2.2 Addition Condensation of Arylamine derivatives

The arylamine polymers were prepared by the seven kinds of arylamine monomers and the paraldehyde via addition condensation. (Scheme 2.1, Figure 2.2) Reaction conditions of the addition condensation were studied to obtain high molecular weight but solvent-soluble arylamine polymers. Acidic condition (pH < 2) was selected for a liner main chain structure and arylamine end-groups. The liner structure attributed the high solubility, and arylamine end-groups prevented decomposition of perovskite layer owing to water formed by dehydration condensation of hydroxyl end-groups. Steric hindrance of *o*-position also helped the liner structure formation (Figure 2.3). The feed ratio between the arylamines and the paraldehyde, and the reaction time were mainly tuned for obtaining high molecular weight. Purchasable *N*,*N*′-diphenyl-*N*,*N*′-bis(4-methylphenyl)-1,4-phenylenediamine was used for examination of polymerization conditions (polymer **5** in Figure 2.2, Table 2.1).

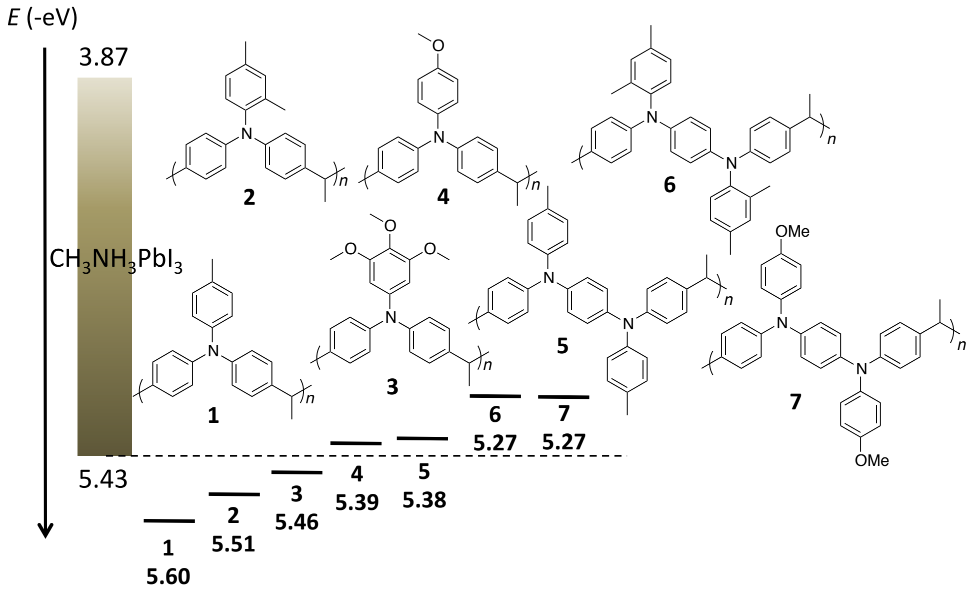

Figure 2.2 Energy level diagram of arylamine polymers.

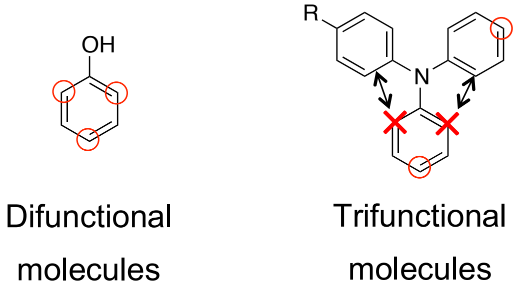

Figure 2.3 Reactivity of monomers

Generally, an elimination of addition reaction and a depolymerization reaction are causes of the decrease of the molecular weight during the addition condensation.[34,46] The excess paraldehyde realized higher molecular weight polymers than an equimolar feed ratio due to high reaction rate of a rate-determining addition step (Table 2.1). The reaction with a feed ratio of 1:4 and reaction time of 8 hours gave the highest molecular weight of >$10^4$ and small $M_w/M_n$ of < 2.0. Under the same reaction conditions, the most arylamine polymers also gave high molecular weight of over $1.0 \times 10^4$, which was attributed to the higher reactivity of the excess aldehyde and the electron-donating methyl and methoxy group, and they also showed higher solubility in the organic solvents (Table 2.2).

**Table 2.1** Polymerization condition of **5**

| Feed ratio [aldehyde]/[amine] | Reaction time (h) | Yield (%) | $M_w$ ($\times 10^3$) | $M_w/M_n$ |
|---|---|---|---|---|
| 1 | 4 | 49 | 2.2 | 1.1 |
| 2 | 4 | 58 | 4.1 | 1.5 |
| 4 | 4 | 56 | 10 | 1.4 |
| 4 | 8 | 61 | 12 | 1.7 |
| 4 | 12 | 23[a)] | 8.0[a)] | 1.4 |
| 6 | 8 | 60 | 11 | 1.6 |

[a)] Chloroform-soluble part.

**Table 2.2** Yield and molecular weight of prepared polymer

| Polymer | Yield (%) | $M_n$ ($\times 10^3$) | $M_w$ ($\times 10^4$) | $M_w/M_n$ |
|---|---|---|---|---|
| **1** | 28 | 9.0 | 1.8 | 2.0 |
| **2** | 26 | 7.7 | 1.0 | 1.4 |
| **3** | 35 | 6.7 | 1.2 | 1.7 |
| **4** | 36 | 8.4 | 1.6 | 1.9 |
| **5** | 61 | 6.9 | 1.2 | 1.7 |
| **6** | 42 | 5.3 | 0.69 | 1.3 |
| **7** | 36 | 10 | 1.6 | 1.5 |

## 2.3 Characteristics of Arylamine Polymers Prepared via Addition Condensation

The prepared arylamine polymers were soluble in organic solvents such as chloroform, chlorobenzene, and tetrahydrofuran. These solvents are used for forming the hole-transporting layer because they do not dissolve the perovskite layer. The solubility of the synthesized polymers was higher than those of previously reported arylamine polymers; for example, **4** dissolved in chloroform with a solubility of 0.11 g/mL, but PTAA, which even has a larger dihedral angle of 55° derived from a twisting structure owing to the alkyl substitutes than that of **4** of 42°, showed a solubility of only

0.08 mg/mL (Figure 2.4). The flexibility of the main chain structures with the ethylidene units increased the solubility even without alkyl side chains.

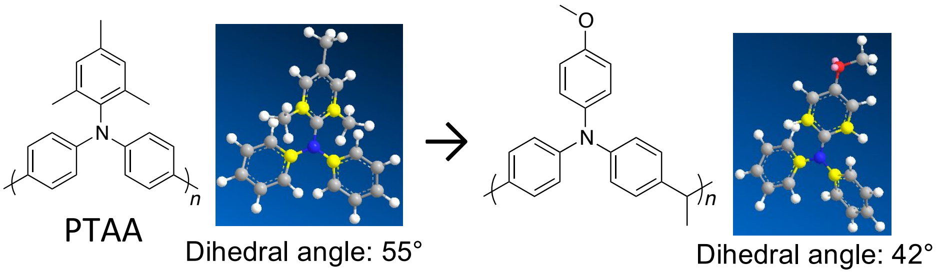

Figure 2.4 Dihedral angels of the arylamine polymers

Structures of the prepared polymers were characterized by $^1$H-NMR in dichloromethane (DCM) with tetramethylsilane (TMS). Aromatic compounds generally react with aldehydes at the *o*- and *p*-positions in the addition condensation.[34] Two methine proton signals from the crosslinking structures have been reported to appear around 4.0 ppm in the $^1$H-NMR spectra of the polymers obtained via addition condensation with aldehydes.[56] However, the polymers obtained in this chapter showed only one peak at around 4.0 ppm. The result strongly suggested that the ethylidene units were formed at only the *p*-position of the arylamines (Figure 2.5). The high acidity (pH < 2) of the reaction condition decreased the reactivity at the *o*-position of the arylamines; the reactivity at *p*-position was more than twice at *o*-position after addition of *p*-toluenesulfonic acid.[34] Moreover, lower steric hindrance might also be one reason for the predominant *p*-position reaction. In summary, these appropriate reaction condition gave the arylamine polymers with linear, high molecular weight, and high solubility. No hydroxyl peaks in $^1$H-NMR spectrum also suggested the arylamine end-groups. Normally, polymers obtained by addition condensation polymerization show wide molecular weight distributions, but all polymers obtained in this study exhibited narrow molecular weight distributions due to high selectivity of reaction at the *p*-position.

End-groups of the polymers were also estimated by an IR spectrum (Figure 2.5). No hydroxyl peaks around 3200–3700 cm$^{-1}$ strongly suggested the absence of the hydroxyl end-groups.

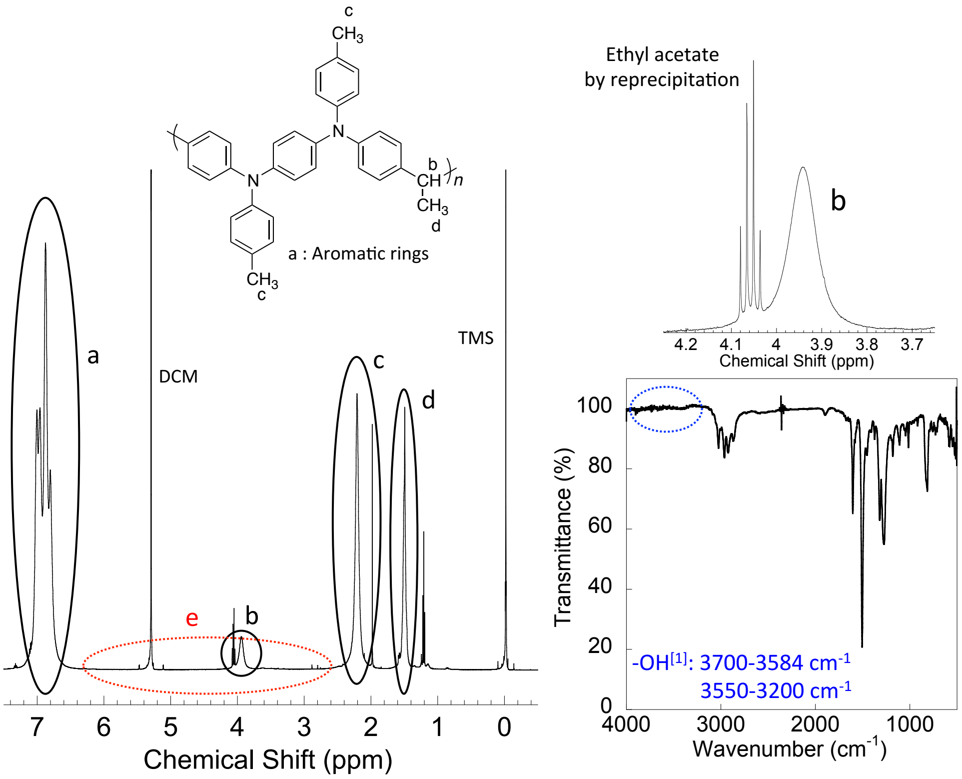

Figure 2.5 $^1$H-NMR spectrum, the enlarged spectrum around 4.0 ppm, and IR spectrum of the polymer **5**.

The glass transition temperatures of all polymers were over 180°C, which were higher than that of PTAA (163 °C), suggesting the higher thermal stability as hole-transporting materials (Table 2.3). The higher glass transition temperature of the polymers, especially the phenylenediamine polymers, could be ascribed to both the high molecular weight and strong intermolecular interaction owing to the great film formability.

Photo-electron spectroscopy in air (PESA) was used to estimate HOMO levels of each polymer layer formed on glass substrates (Table 2.3). The estimated HOMO levels of **4** (-5.39 eV) and **5** (-5.38 eV) were deeper than that of PTAA (-5.29 eV, or -5.14 eV as previously reported[57]), but shallower than the top energy level of the valence band of the perovskite compounds. The methoxy group of **4** as an electron-donating substituent and the longer π-conjugated phenylenediamine unit of **5** could realize these appropriate HOMO levels as the hole-transporting layers of the perovskite cells. The band gaps of the polymers were estimated from absorption edges of UV-vis spectra of the polymer layers. The estimated LUMO levels of all polymers were shallower than the bottom energy level of the conduction band of the perovskite layer (-3.75 eV[58]), which was also appropriate as the hole-transporting layers of the perovskite solar cells.

**Table 2.3** Glass transition temperature ($T_g$), HOMO, LUMO, and band gap of the arylamine polymers

| Polymer | $T_g$ (°C) | HOMO$^{a)}$ (-eV) | LUMO$^{b)}$ (-eV) | Band gap$^{c)}$ (eV) |
|---|---|---|---|---|
| **1** | 194 | 5.60 | 2.17 | 3.43 |
| **2** | 180 | 5.51 | 2.00 | 3.51 |
| **3** | 190 | 5.46 | 2.35 | 3.11 |
| **4** | 196 | 5.39 | 2.06 | 3.33 |
| **5** | 221 | 5.38 | 2.30 | 3.08 |
| **6** | 224 | 5.27 | 2.10 | 3.17 |
| **7** | 212 | 5.27 | 2.17 | 3.10 |
| PTAA | 163 | 5.29 (5.14$^{d)}$) | 2.31 | 2.98 (2.83$^{d)}$) |

$^{a)}$ Measured by PESA. $^{b)}$ Estimated by the HOMO levels and band gaps. $^{c)}$ Measured by UV-vis. $^{d)}$ Previously reported measurement$^{34}$

A cyclic voltammetry (vs. Ag/AgCl) with three electrode systems in acetonitrile solution of 0.1 M tetrabutylammonium perchlorate exhibited reversible redox responses at 0.44 and 0.99 V for **5**, and 0.77 V for **4** (Figure 2.6). The durable redox proposed that stable carriers might be generated also in the polymer films. The cyclic voltammogram of **5** showed a two-step reversible redox reaction; the first electron to arylammonium cation radical formation and the second electron to dication formation.[50] The polymers with phenylenediamine units possessed a possibility of higher hole mobility than triarylamine polymers because of the longer π-conjugated length and the stable bipolaron generation.

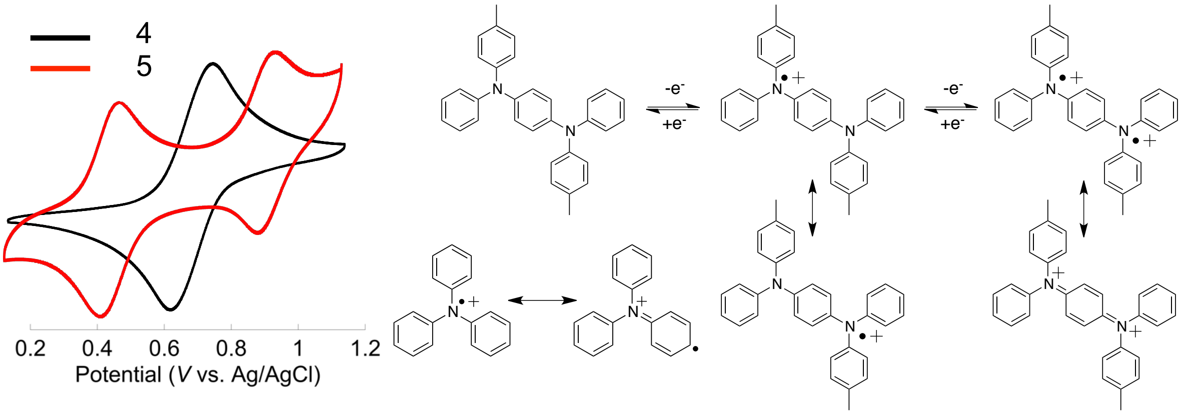

Figure 2.6 Cyclic voltammograms of **4** and **5**, and the redox mechanism of the arylamine and phenylenediamine units.

A simple spin-coating process formed the thin films of **4** and **5** on glass substrates. Atomic force microscope (AFM) surface images of these two polymer layers exhibited homogeneous layer formation with small roughness of under 10 nm (Figure 2.7). An x-ray diffraction (XRD) pattern of the thin film of **5** indicated the amorphous structure with no crystalline peaks, which was suitable for the components of the organic electric devices (Figure 2.8). On the other hand, the XRD pattern of **4** slightly contained crystalline peaks, and the crystallinity could decrease the hole-transporting ability owing to the existence of grain boundaries.

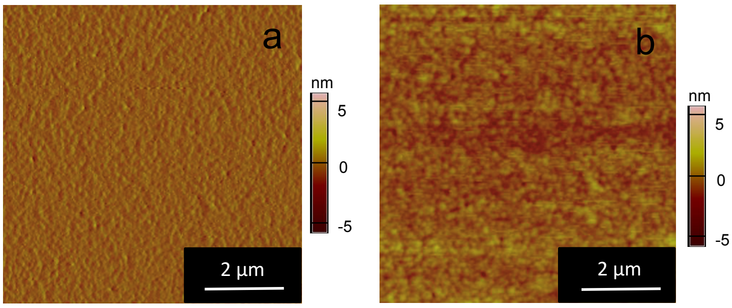

Figure 2.7 AFM surface images of the arylamine polymers cast on glass substrates (a: **5** and b: **4**).

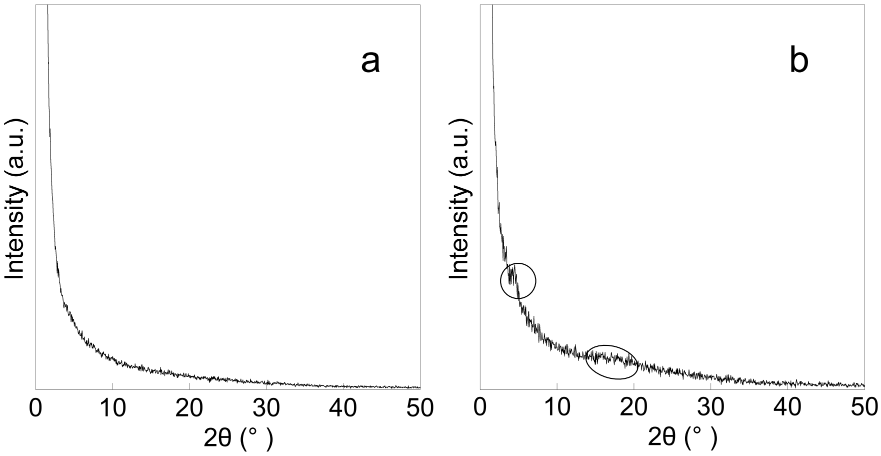

Figure 2.8 XRD patterns of the thin layers (a: **5** and b: **4**).

The hole mobility of **4** and **5** was measured by a space-charge-limited current (SCLC) method using a hole-only device (FTO/PEDOT:PSS [poly(3,4-ethylenedioxythiophene)-poly(styrenesulfonate)]/hole-transporting polymers/Au) (Figure 2.9). The hole mobility of **5** (μ = 5.4×$10^{-5}$ $cm^2$/Vs) was estimated to be almost same with that of PTAA (μ = 5.6×$10^{-5}$ $cm^2$/Vs). On the other hand, the hole mobility of **4** was lower than that of these two polymers (μ = 0.99×$10^{-5}$ $cm^2$/Vs), which might be derived from the charge recombination at the grain boundaries.

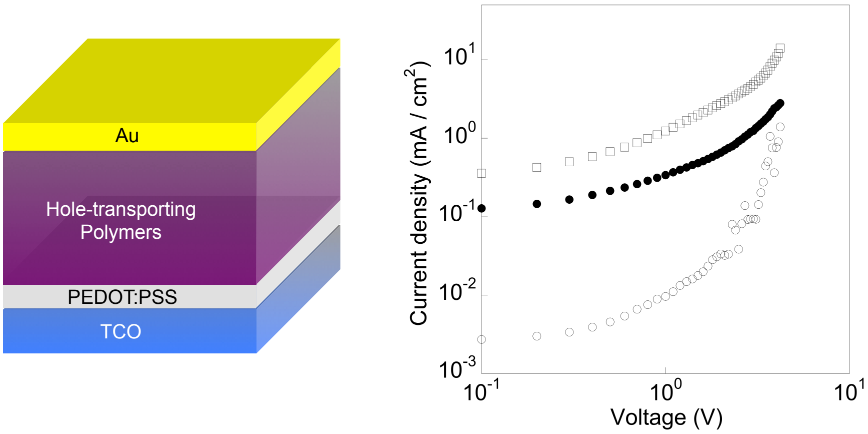

Figure 2.9 Configuration of a hole-only device and *J*-*V* plots of the arylamine polymers for the SCLC method (●: **5**, ○: **4**, and □: **PTAA**).

## 2.4 Perovskite Solar Cells Fabricated with Arylamine Polymers

The cell configuration of the perovskite solar cells fabricated with spin-coated arylamine polymers as the hole-transporting layers is shown in Figure 2.10 (detailed fabrication processes are written in Chapter 2.5).[59–63] A cross-sectional SEM image of the cells exhibited the homogenous polymer layer with suitable thickness of ca. 10 nm as the hole-transporting layer (Figure 2.10).

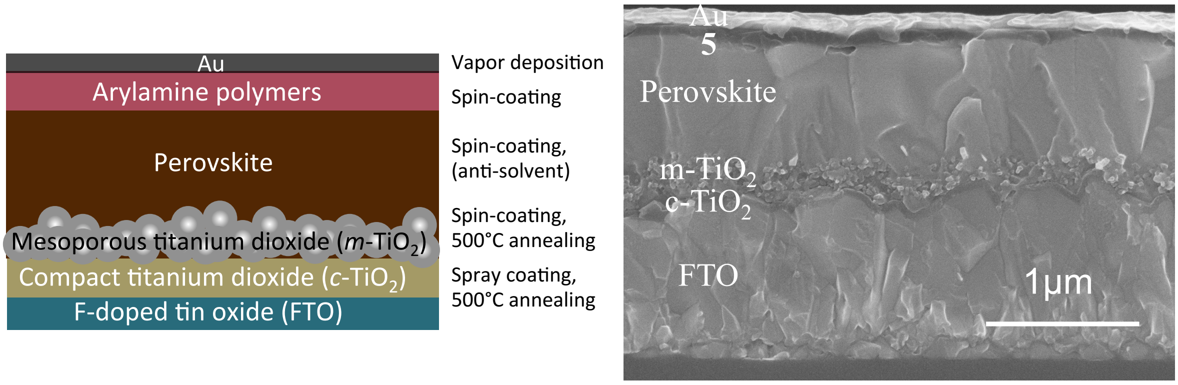

Figure 2.10 A cell configuration and a cross-sectional SEM image of the perovskite solar cell fabricated with **5** as the hole-transporting layer.

The perovskite solar cell fabricated with **5** exhibited the high photovoltaic conversion efficiency of 16.0% (Figure 2.11, Table 2.4), which was the almost same efficiency of the cell fabricated with PTAA. The deeper HOMO level of **5**, compared with PTAA, could yield a higher open-circuit voltage ($V_{OC}$). In contrast, the cell fabricated with **4** exhibited the lower efficiency probably because of the lower hole mobility of **4** estimated by SCLC method. The low hysteresis and high reproducibility were also observed on the cell fabricated with **5**. The average photovoltaic conversion efficiency of the cells with **4**, **5**, and PTAA in 8 cells were 9.0, 15.7, and 15.9 % and the standard deviations of them were 0.77, 0.34, and 0.24.

**Table 2.4** Short-circuit current density ($J_{SC}$), open-circuit voltage ($V_{OC}$), fill factor (*FF*), and photovoltaic conversion efficiency ($\eta$) of perovskite solar cells fabricated with the polymers

| Hole-transporting layer | $J_{sc}$ (mA/cm$^2$) | $V_{oc}$ (V) | *FF* (-) | $\eta$ (%) |
|---|---|---|---|---|
| **4** | 19.5 | 0.88 | 0.56 | 9.6 |
| **5** | 21.6 | 1.03 | 0.72 | 16.0 |
| **PTAA** | 21.9 | 1.02 | 0.72 | 16.1 |

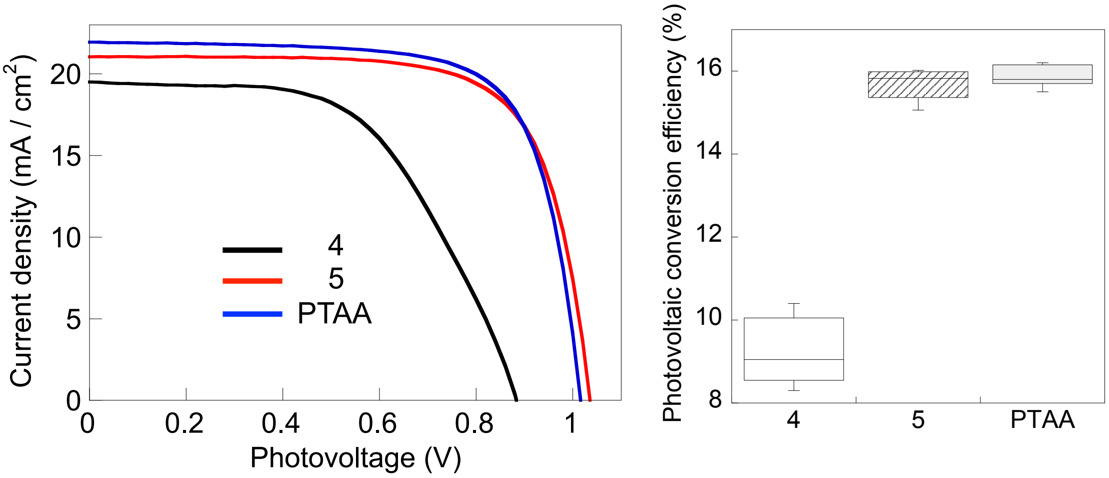

Figure 2.11 *J*-*V* curves and box plots for the photovoltaic conversion efficiency of the perovskite solar cells fabricated with **4**, **5**, and PTAA. Error bars represent maximum and minimum values. The middle line represents the median value. Upper and lower error bars in the box represent the third quartile and first quartile.

The cell fabricated with **5** exhibited high thermal stability and the cell performance improved over time during the durability test under accelerated conditions using a hot plate at 85 °C (Figure 2.12). The improved efficiency could be explained by doping of the **5** with ambient oxygen, which might increase hole carrier density to enhance the conductivity of the polymer layer. On the other hand, the efficiency of the standard cell with spiro-OMeTAD and additives, lithium bis(trifluoromethylsulphonyl) imide (LiTFSI), tris(2-(1*H*-pyrazol-1-yl)-4-*tert*-butylpyridine)cobalt(III) tri[bis(trifluoromethane)sulfonimide] (FK209), and *tert*-butylpyridine (*t*BP), was decreased dramatically, as previously reported.[64,65]

In conclusion, the facile addition condensation of arylamine derivatives and a paraldehyde, proposed in this chapter, realizes the new arylamine polymers with flexible molecular structures, tuned the energy levels via electro-donating substituents, and great film formability due to high molecular weight. The durability of the polymers proposed that they were appropriate as the hole-transporting materials of the efficient perovskite solar cells.

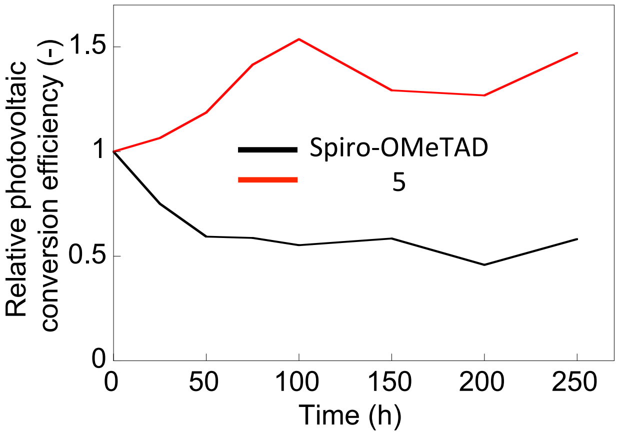

Figure 2.12 Time course of the relative photovoltaic conversion efficiency of the cells fabricated with **5** and spiro-OMeTAD (vs. the initial) of perovskite solar cells.

## 2.5 Experimental Section

### 2.5.1 Monomer preparation

4-Methyltriphenylamine, 4-methoxytriphenylamine, and *N*,*N*′-diphenyl-*N*,*N*′-bis(4-methylphenyl)-1,4-phenylenediamine were purchased by Tokyo Chemical Industry.

4-Bromo-*m*-xylene or 5-bromo-1,2,3-trimethoxybenzene (5.90 mmol, Tokyo Chemical Industry), diphenylamine (5.90 mmol, Tokyo Chemical Industry), sodium *tert*-butoxyde (1.8 mmol, Tokyo Chemical Industry), and [1,1′-bis(diphenylphosphino)ferrocene]dichloropalladium(II) (Pd(dppf)$Cl_2$) (0.59 mmol, Tokyo Chemical Industry) were dissolved in toluene (20 ml, Kanto Chemical) and were heated with stirring at 110°C (reflux) for 24 h under the nitrogen condition (Scheme 2.2). 2,4-Dimethyltriphenylamine and 3,4,5-trimethoxytriphenylamine were obtained (yield: 59% and 35%, respectively) after purifications by extraction (hexane/water), filtration, column chromatograph (chloroform:hexane = 1:3), and recrystallization (methanol/chloroform).

$^1$H-NMR for 2,4-dimethyltriphenylamine: 7.20−6.86 (13H, Ph), 2.35 (3H, *p*-$CH_3$), 1.99 (3H, *o*-$CH_3$). Melting point: 79°C. Mass spectrum: 273.0 (calculated), 273.0 (Measured). $^1$H-NMR for 3,4,5-trimethoxytriphenylamine: 7.23−6.71 (12H, Ph), 3.81 (6H, *m*-$CH_3O$), 3.69 (3H, *p*-$CH_3O$). Melting point: 69°C. Mass spectrum: 335.2 (calculated), 335.2 (measured).

2,4-Dimethyldiphenylamine (4.2 mmol, Tokyo Chemical Industry), 1,4-diiodobenzene (2.1 mmol, Tokyo Chemical Industry), sodium *tert*-butoxide (12 mmol), and Pd(dppf)$Cl_2$ (0.04 mmol) were dissolved in toluene (20 ml) and heated with stirring at 110°C (reflux) for 24 h under the nitrogen condition (Scheme 2.3). *N*,*N*′-Diphenyl-*N*,*N*′-bis(2,4-dimethylphenyl)-1,4-phenylenediamine was obtained (yield: 8%) after purifications by extraction (chloroform/water), filtration, column chromatograph (dichloromethane:hexane = 3:7), and recrystallization (methanol/chloroform).

$^1$H-NMR for *N*,*N*′-diphenyl-*N*,*N*′-bis(2,4-dimethylphenyl)-1,4-phenylenediamine: 7.15 (4H, Ph), 7.01 (6H, Ph), 6.87 (10H, Ph), 2.32 (6H, *p*-$CH_3$), 2.02 (6H, *o*-$CH_3$). Melting point: 182°C. Mass spectrum: 468.6 (calculated), 468.0 (measured).

*N*,*N*′-Diphenyl-1,4-phenylenediamine (2.0 mmol, Tokyo Chemical Industry), 4-iodomethoxybenzene (4.0 mmol, Tokyo Chemical Industry), sodium *tert*-butoxide (12 mmol), and Pd(dppf)$Cl_2$ (0.04 mmol) were dissolved in toluene (20ml) and heated with stirring at 110°C (reflux) for 24 h under the nitrogen condition (Scheme 2.3). *N*,*N*′-Diphenyl-*N*,*N*′-bis(4-methoxylphenyl)-1,4-phenylenediamine was obtained (yield:

29%) after purifications by extraction (chloroform/water), filtration, column chromatograph (dichloromethane:hexane = 1:3), and recrystallization (methanol/ chloroform).

$^1$H-NMR for *N*,*N′*-diphenyl-*N*,*N′*-bis(4-methoxylphenyl)-1,4-phenylenediamine: 7.18 (4H, Ph), 7.08 (4H, Ph), 7.01 (4H, Ph), 6.90(6H, Ph), 6.82 (4H, Ph), 3.77 (6H, $CH_3O$). Melting point: 135°C. Mass spectrum: 472.6 (calculated), 472.5 (measured).

### 2.5.2 Polymerization via addition-condensation

Arylamine monomers were polymerized with paraldehyde using a procedure similar to that in previous papers for polymerizing arylamines such as 4-methyltriphenylamine.[34,47]

4-Methyltriphenylamine, 2,4-dimethyltriphenylamine, 3,4,5-trimethoxytriphenylamine, 4-methoxytriphenylamine, *N*,*N′*-diphenyl-*N*,*N′*-bis(4-methylphenyl)-1,4-phenylenediamine, *N*,*N′*-diphenyl-*N*,*N′*-bis(2,4-dimethylphenyl)-1,4-phenylenediamine, or *N*,*N′*-diphenyl-*N*,*N′*-bis(4-methoxylphenyl)-1,4-phenylenediamine (5 mmol), paraldehyde (707 mg, 6.7 mmol, Tokyo Chemical Industry), and *p*-toluenesulfonic acid (147 mg, 0.80 mmol, Tokyo Chemical Industry) were dissolved in nitrobenzene (30 mL, Kanto Chemical Co.) and heated with stirring at 80 °C for 4 h under nitrogen condition. The reaction mixture was poured into methanol, and the precipitate was separated by filtration. The separated materials were washed with methanol and ethyl acetate. The powder was redissolved in chloroform and was poured into methanol again, which processes were repeated twice. The products were dried under low pressure to give polymers as white powders. The given polymers of poly(4-methyltriphenylamine-*co*-acetoaldehyde), poly(2,4-dimethyltriphenylamine-*co*-acetoaldehyde), poly(3,4,5-trimethoxytriphenylamine-*co*-acetoaldehyde), poly(4-methoxytriphenylamine-*co*-acetoaldehyde), poly(*N*,*N′*-diphenyl-*N*,*N′*-bis(4-methylphenyl)-1,4-phenylenediamine-*co*-acetoaldehyde), poly(*N*,*N′*-diphenyl-*N*,*N′*-bis(2,4-dimethylphenyl)-1,4-phenylenediamine-*co*-acetoaldehyde), or poly(*N*,*N′*-diphenyl-*N*,*N′*-bis(4-methoxylphenyl)-1,4-phenylenediamine-*co*-acetoaldehyde) were named as **1**-**7**, respectively. The yields and molecular weights of each polymer are listed in Table 2.2. The glass transition temperature and energy levels of each polymer are listed in Table 2.3.

$^1$H-NMR for **1**: 7.20−6.63 (12H, Ph), 4.08−3.92 (1H, CH), 2.37−2.04 (3H, *p*-$CH_3$), 1.58−1.43 (3H, $CH_3$). $^1$H-NMR for **2**: 7.09−6.65 (11H, Ph), 4.03−3.85 (1H, CH), 2.34−2.16 (3H, *p*-$CH_3$), 1.99−1.82 (3H, *o*-$CH_3$), 1.60−1.41 (3H, $CH_3$). $^1$H-NMR for **3**: 7.09−6.92 (8H, Ph), 6.28 (2H,*o*-Ph), 4.01−3.94 (1H, CH), 3.92−3.69 (3H, *p*-$CH_3O$), 3.69−3.52 (6H, *m*-$CH_3O$), 1.60−1.41 (3H, $CH_3$). $^1$H-NMR for **4**: 7.16−6.73 (11H, Ph), 4.04−3.90 (1H, CH), 3.79−3.65 (3H, $CH_3O$), 1.58−1.42 (3H, $CH_3$). $^1$H-NMR for **5**: 7.17−6.66 (20H, Ph), 4.10−3.82 (1H, CH), 2.32−2.11 (6H, *p*-$CH_3$), 1.57−1.45 (3H, $CH_3$). $^1$H-NMR for **6**: 7.17−6.63 (18H, Ph), 3.99−3.88 (1H, CH), 2.34−2.18 (6H, *p*-$CH_3$), 2.05−1.82 (6H, *o*-$CH_3$), 1.60−1.44 (3H, $CH_3$). $^1$H-NMR for **7**: 7.19−6.58 (20H, Ph), 4.05−3.85 (1H, CH), 3.84−3.46 (6H, $CH_3O$), 1.72−1.40 (3H, $CH_3$).

### 2.5.3 Fabrication of perovskite solar cells

Conductive glass substrates of fluorine-doped tin oxide (FTO; Atock Co.; sheet resistance of 30 $\Omega$ sq$^{-1}$) were patterned by an edging method using Zn powder and HCl aqueous solution and were cleaned by a sonication in water, acetone, and 2-propanol (IPA), respectively. A compact $TiO_2$ layer was sprayed on the edged and washed FTO substrates by an ethanol solution of titanium (IV) tetraacetylacetonate (Wako Pure Chemical Industries). The substrates were soaked in aqueous 0.2 M $TiCl_4$ solution at 70 °C for 45 min and then annealed at 500 °C for 1 h. An ethanol solution of Ti paste (150 mg/ml. PST-18NR, JGC Catalysts and Chemicals) was spin-coated on the compact $TiO_2$ layer at 4000 rpm for 20 s, the substrates were annealed at 100 °C for 10 min, and then annealed at 500 °C for 1 h. The substrates were soaked in aqueous 10 mM $TiCl_4$ solution at 70 °C for 45 min, and annealed at 500 °C for 1 h again.

The perovskite layer was fabricated based on previous papers.[11,66–70] The precursor solution was prepared by dissolving mixture of formamidine hydroiodide (172 mg), methylamine hydrobromide (22.4 mg), $PbI_2$ (507 mg), $PbBr_2$ (80.7 mg), CsI (16.3 mg), and RbI (13.4 mg) powders (Tokyo Chemical Industry) in mixed-solution of *N*,*N*-dimethylformamide (800 μL), dimethyl sulfoxide (114 μL), and acetonitrile (86 μL) (Kanto Chemical Co.). The precursor solution was spin-coated on the prepared substrates at 1000 rpm for 10 s and at 6000 rpm for 20 s. 100 ml chlorobenzen was drop-cast on the spin-coating substrates at 28 s after starting. Toluene solutions of arylamine polymers including PTAA (10 mg) were mixed with a solution of 520 mg/mL LiTFSI in acetonitrile (4.9 μL) and *t*BP (2.0 μL). The hole-transporting polymer solution was spin-coated on the perovskite layer at 4000 rpm for 20 s. Finally, a 100 nm Au layer was deposited at 0.1 nm/s rate on the hole-transporting polymer layer using a vacuum chamber (VPC-1100, ULVAC) for the electrode.

### 2.5.4 Measurements

$^1$H-NMR spectra were measured by an NMR spectrometer (JNM-ECX500, JEOL). Deuterated dichloromethane was used as a solvent of arylamine polymers for measuring $^1$H-NMR and chemical shifts of tetramethylsilane in the deuterated dichloromethane were used as a standard. UV-Vis spectra were performed with a spectrophotometer (V-670, JASCO) to determine the band gaps. X-Ray patterns of the polymer films were recorded with an x-ray diffractometer with the parallel beam method (LINT-Ultima III, Rigaku). Photoelectron spectroscopy in air was measured with a photoelectron spectrometer (AC-3E, Riken Keiki) to estimate HOMO levels of the polymers. LUMO levels were calculated by the values of the band gaps and HOMO levels.

An atomic force microscope (Dimension 3100, Dell) was used to observe the polymer layer surfaces. A scanning electron microscope (SU8000, Hitachi) was used for cross-sectional images of the completed cells.

The molecular weights of the prepared polymers were determined by gel permeation chromatography on a liquid chromatography system (HLC-8220GPC, Tosoh; TSKgel SuperMultiporeHZ-M column), with polystyrene as the standard and tetrahydrofuran as an eluent. The glass transition temperature was measured with a differential scanning calorimeter (Q200, TA Instruments). Cyclic voltammograms were measured with an electrochemical analyzer (ALS 760EW, BAS) in acetonitrile solution of 0.1 M tetrabutylammonium perchlorate. Dihedral angles were calculated by using Molecular Mechanics program 2 (MM2) calculator in Gaussian.

A current-voltage measurement under irradiation and a space-charge-limited current (SCLC) method were recorded with a solar cell evaluation system (YQ-2000, JASCO) and a solar simulator (CEP-2000MLQ, Bunkoukeiki).

### 2.5.5 Fabrication of hole-only device for SCLC measurements

1. ITO or FTO substrates (25 mm×15 mm) were edged via Zn powder and HCl

aqueous solution as mentioned above.

2. Edged substrates were washed by pure water, acetone, and IPA for 10 min by sonicator, respectively.
3. Surface of the substrates were treated by UV/$O_3$ washing for 15 min.
4. PEDOT:PSS solution (Clevious, Heraeus) was filtered by 0.1μm membrane filter for forming a homogeneous PEDOT:PSS layer.
5. Before spin-coating, KimWipes were placed around spin-coater and were wet by pure water for enhancing the ambient humidity.
6. 350μL PEDOT:PSS solution was spin-coated on the UV/$O_3$ treated substrates at 1500 rpm for 30 s. (The cover of the spin-coater should be closed.)
7. Spin-coated substrates were dried on the 150°C hotplate for 20 min. (After then, the substrates should be placed on reduced pressure condition for overnight.)
8. Hole-transporting material solution was prepared as concentrated as possible (over 20 mg/ml is better). (Dopants are not needed because SCLC method injects superabundant carriers; in other words, carrier concentration is not related to carrier mobility.)
9. Thick hole-transporting layer was formed by spin-coating 100 μL solution at 2000 (or lower) rpm for 20 s. (Depending on the solvent, annealing should be done.)
10. The substrates were dried satisfyingly at a dry room.
11. 80 nm Au or Al were deposited as counter electrode. The deposition rate should be slower than usual (ca. 0.05 nm/s).

### 2.5.6 SCLC measurement

1. SCLC can also be measured by a solar simulator. The condition of measurement is only forward 0-5 V without light irradiation.
2. The thickness of a target layer was measured by SEM or TENCOR (a thickness meter).
3. The results of SCLC measurements are arranged by an excel file for SCLC analysis. The voltage and current are filled in the cells to form a graph. $J/V^2$ is a tendency of the graph, $L$ is a thickness of the layer, and $\varepsilon$ is a relative permittivity.

$$\mu = \frac{8}{9}\frac{L^3}{\varepsilon\varepsilon_0}\frac{J}{V^2}\ (Child - Langmuir\ equation)$$

## References

[1] K. Tsuchiya, T. Shimomura, K. Ogino, *Polymer* **2009**, *50*, 95–101.

[2] G. Wang, Y. Wu, W. Ding, G. Yu, Z. Hu, H. Wang, S. Liu, Y. Zou, C. Pan, *J. Mater. Chem. A* **2015**, *3*, 14217–14227.

[3] S. O. Hacioglu, S. Toksabay, M. Sendur, L. Toppare, *J. Polym. Sci. Part A Polym. Chem.* **2014**, *52*, 537–544.

[4] C. Kvarnström, A. Petr, P. Damlin, T. Lindfors, A. Ivaska, L. Dunsch, *J. Solid State Electrochem.* **2002**, *6*, 505–512.

[5] M. Jikei, R. Mori, S. Kawauchi, M. Kakimoto, Y. Taniguchi, *Polym. J.* **2002**, *34*, 550–557.

[6] Y. Yang, Q. Zhang, S. Zhang, S. Li, *Polymer* **2013**, *54*, 5698–5702.

[7] T. Michinobu, *Macromol. Chem. Phys.* **2015**, *216*, 1387–1395.

[8] S. G. J. Mathijssen, M. Kemerink, A. Sharma, M. Cölle, P. A. Bobbert, R. A. J. Janssen, D. M. De Leeuw, *Adv. Mater.* **2008**, *20*, 975–979.

[9] S. Ameen, M. A. Rub, S. A. Kosa, K. A. Alamry, M. S. Akhtar, H. S. Shin, H. K. Seo, A. M. Asiri, M. K. Nazeeruddin, *ChemSusChem* **2016**, *9*, 10–27.

[10] A. Marchioro, J. Teuscher, D. Friedrich, M. Kunst, R. Van De Krol, T. Moehl, M. Grätzel, J. E. Moser, *Nat. Photonics* **2014**, *8*, 250–255.

[11] F. Bella, G. Griffini, J. P. Correa-Baena, G. Saracco, M. Grätzel, A. Hagfeldt, S. Turri, C. Gerbaldi, *Science* **2016**, *354*, 203–206.

[12] M. I. Asghar, J. Zhang, H. Wang, P. D. Lund, *Renew. Sustain. Energy Rev.* **2017**, *77*, 131–146.

[13] A. Isakova, P. D. Topham, *J. Polym. Sci. Part B Polym. Phys.* **2017**, *55*, 549–568.

[14] J. Lee, A. R. Han, H. Yu, T. J. Shin, C. Yang, J. H. Oh, *J. Am. Chem. Soc.* **2013**, *135*, 9540–9547.

[15] W. Yan, S. Ye, Y. Li, W. Sun, H. Rao, Z. Liu, Z. Bian, C. Huang, *Adv. Energy Mater.* **2016**, *6*, 1–20.

[16] Y. H. Lee, Y. P. Lee, C. J. Chiang, F. K. Wei, C. H. Wu, W. C. Chen, C. Shen, H. A. Jeng, L. Wang, M. W. Liu, et al., *J. Mater. Chem. A* **2014**, *2*, 14600–14612.

[17] S. N. Habisreutinger, T. Leijtens, G. E. Eperon, S. D. Stranks, R. J. Nicholas, H. J. Snaith, *Nano Lett.* **2014**, *14*, 5561–5568.

[18] Y. S. Kwon, J. Lim, H. J. Yun, Y. H. Kim, T. Park, *Energy Environ. Sci.* **2014**, *7*, 1454–1460.

[19] Q. Wang, C. Bi, J. Huang, *Nano Energy* **2015**, *15*, 275–280.

[20] R. Steyrleuthner, M. Schubert, F. Jaiser, J. C. Blakesley, Z. Chen, A. Facchetti, D. Neher, *Adv. Mater.* **2010**, *22*, 2799–2803.

[21] M. Gross, D. C. Müller, H.-G. Nothofer, U. Scherf, D. Neher, C. Bräuchle, K. Meerholz, *Nature* **2000**, *405*, 661–665.

[22] K. Ogino, A. Kanegae, R. Yamaguchi, H. Sato, J. Kurjata, *Macromol. Rapid Commun.* **1999**, *20*, 103–106.

[23] H. Xiao, B. Leng, H. Tian, *Polymer* **2005**, *46*, 5707–5713.

[24] A. Iwan, D. Sek, *Prog. Polym. Sci.* **2011**, *36*, 1277–1325.

[25] I. M. Christian, C. Lambert, *Langmuir* **2011**, *27*, 5029–5039.

[26] S. Hunter, J. Chen, T. D. Anthopoulos, *Adv. Funct. Mater.* **2014**, *24*, 5969–5976.

[27] J. H. Heo, H. J. Han, D. Kim, T. K. Ahn, S. H. Im, *Energy Environ. Sci.* **2015**, *8*, 1602–1608.

[28] N. J. Jeon, J. H. Noh, W. S. Yang, Y. C. Kim, S. Ryu, J. Seo, S. Il Seok, *Nature* **2015**, *517*, 476–480.
[29] Y. H. Lee, *Nat. Photonics* **2013**, *7*, 486–491.
[30] Z. Zhang, K. Zhang, G. Liu, C. Zhu, K. Neoh, *Macromolecules* **2009**, *42*, 3104–3111.
[31] M. Yan, J. Yuan, Y. Pi, J. Liang, Y. Liu, Q. Wu, X. Luo, S. Liu, J. Chen, X. Zhu, et al., *Org. Biomol. Chem* **2016**, *14*, 451–454.
[32] N. Kataoka, Q. Shelby, J. P. Stambuli, J. F. Hartwig, *J. Org. Chem.* **2002**, *8107*, 5553–5566.
[33] C. J. Chen, Y. C. Hu, G. S. Liou, *Chem. Commun.* **2013**, *49*, 2804–2806.
[34] L. Pilato, *Phenolic Resins: A Century of Progress*, **2010**.
[35] J. Huang, S. R. Turner, *Polym. Rev.* **2018**, *58*, 1–41.
[36] A. Ã. Effendi, H. Gerhauser, A. V Bridgwater, *Renew. Sustain. Energy Rev.* **2008**, *12*, 2092–2116.
[37] A. R. Moosavi-zare, M. A. Zolfigol, M. Daraei, *Synlett.* **2014**, 1173–1177.
[38] K. Hong, S. Park, *Mater. Chem. Phys.* **1999**, *58*, 128–131.
[39] W. Gindl, F. Zargar-Yaghubi, R. Wimmer, *Bioresour. Technol.* **2003**, *87*, 325–330.
[40] Y. Wu, S. Fang, Y. Jiang, *J. Mater. Chem.* **1998**, *8*, 2223–2227.
[41] M. G. Kim, L. W. Amos, E. Barnes, *Ind. Eng. Chem. Res.* **1990**, *0888*, 2032–2037.
[42] T. Ohishi, T. Kojima, T. Matsuoka, H. Kotsuki, *Tetrahedron Lett.* **2001**, *42*, 2493–2496.
[43] N.-E. Es-Safi, V. Cheynier, M. Mountounet, *J. Agric. Food Chem.* **2002**, *50*, 5571–5585.
[44] T. Furuno, Y. Imamura, H. Kajita, *Wood Sci. Technol.* **2004**, *37*, 349–361.
[45] H. Uyama, H. Kurioka, I. Kaneko, S. Kobayashi, *Chem. Lett.* **1994**, 423–426.
[46] J. M. Son, K. Ogino, N. Yonezawa, H. Sato, *Synth. Met.* **1998**, *98*, 71–77.
[47] Y. Nishikitani, N. Inokuchi, H. Nishide, S. Uchida, T. Shibanuma, S. Nishimura, *J. Phys. Chem. C* **2016**, *120*, 13976–13986.
[48] H. Cheng, K. Y. Chiu, S. H. Lu, C. Chen, Y. W. Lee, T. Yang, M. Y. Kuo, P. P. Chen, Y. O. Su, *J. Phys. Chem. A* **2015**, *10*, 1933-1942.
[49] Y. Nishikitani, M. Kobayashi, S. Uchida, T. Kubo, *Electrochim. Acta* **2001**, *46*, 2035–2040.
[50] X. Ma, H. Niu, H. Wen, S. Wang, Y. Lian, X. Jiang, C. Wang, X. Bai, W. Wang, *J. Mater. Chem. C* **2015**, *3*, 3482–3493.
[51] X. Fan, C. Rodríguez-Escrich, S. Sayalero, M. A. Pericàs, *Chem. Eur. J.* **2013**, *3*, 10814–10817.
[52] F. E. Goodson, S. I. Hauck, J. F. Hartwig, *J. Am. Chem. Soc.* **1999**, *121*, 7527–7539.
[53] J. Kuwabara, T. Yamagata, T. Kanbara, *Tetrahedron* **2010**, *66*, 3736–3741.
[54] L. P. Hammett, *J. Am. Chem. Soc.* **1937**, *59*, 96–103.
[55] A. Dijksman, A. Marino-González, A. Mairata i Payeras, I. W. C. E. Arends, R. A. Sheldon, *J. Am. Chem. Soc.* **2001**, *123*, 6826–6833.
[56] X. Wang, Z. Chen, K. Ogino, H. Sato, S. Miyata, H. Tan, *Polym. J.* **2000**, *32*, 778–783.

[57] S. Ryu, J. H. Noh, N. J. Jeon, Y. Chan Kim, W. S. Yang, J. Seo, S. Il Seok, *Energy Environ. Sci.* **2014**, *7*, 2614–2618.

[58] Huanping Zhou, Q. Chen, G. Li, S. Luo, T. Song, H.-S. Duan, Z. Hong, J. You, Y. Liu, Y. Yang, *Science* **2014**, *345*, 542.

[59] A. Kojima, K. Teshima, Y. Shirai, T. Miyasaka, *J. Am. Chem. Soc.* **2009**, *131*, 6050–6051.

[60] H. S. Kim, C. R. Lee, J. H. Im, K. B. Lee, T. Moehl, A. Marchioro, S. J. Moon, R. Humphry-Baker, J. H. Yum, J. E. Moser, et al., *Sci. Rep.* **2012**, *2*, 1–7.

[61] L. Cojocaru, S. Uchida, Y. Sanehira, J. Nakazaki, T. Kubo, H. Segawa, *Chem. Lett.* **2015**, *44*, 674–676.

[62] N. J. Jeon, J. H. Noh, Y. C. Kim, W. S. Yang, S. Ryu, S. Il Seok, *Nat. Mater.* **2014**, *13*, 897–903.

[63] H. Do Kim, H. Ohkita, H. Benten, S. Ito, *Adv. Mater.* **2016**, *28*, 917–922.

[64] T. Malinauskas, D. Tomkute-luksiene, R. Sens, M. Daskeviciene, R. Send, *ACS Appl. Mater. Interfaces* **2015**, *7*, 11107–11116.

[65] Q. Luo, Y. Zhang, C. Liu, J. Li, H. Lin, *J. Mater. Chem. A* **2015**, *3*, 15996–16004.

[66] W. S. Yang, B.-W. Park, E. H. Jung, N. J. Jeon, *Science* **2017**, *356*, 1376–1379.

[67] F. Giordano, A. Abate, J. P. Correa Baena, M. Saliba, T. Matsui, S. H. Im, S. M. Zakeeruddin, M. K. Nazeeruddin, A. Hagfeldt, M. Graetzel, *Nat. Commun.* **2016**, *7*, 10379.

[68] W. Okada, T. Suga, K. Oyaizu, H. Segawa, H. Nishide, *ACS Appl. Energy Mater.* **2019**, *2*, 2848-2853.

[69] H. Maruo, S. Tanaka, M. Takamura, K. Oyaizu, H. Segawa, H. Nishide, *MRS Commun.* **2018**, *8*, 122–126.

[70] H. Maruo, Y. Sasaki, K. Harada, K. Suwa, K. Oyaizu, H. Segawa, H. Nishide, *Polym. J.* **2019**, 91–96.

Figures, tables, and texts are partially adapted with permission from K. Suwa, S. Tanaka, K. Oyaizu, H. Nishide, *Polym. Int.* **2018**, *67*, 670-674. Published by John Wiley and Sons, New Jersey (2018).

# Chapter 3: Anti-Oxidizing TEMPO Polymer Incorporation for Highly Durable Perovskite Solar Cells

**3.1 Introduction**
**3.2 Polymer Incorporation as a Scaffold for High Quality Perovskite Layer Growth**
**3.3 Anti-Oxidizing TEMPO Polymer-Incorporated Perovskite Layer and its Solar Cells**
**3.4 Incorporation of Phenolic Antioxidants for Further Improvement of Cell Durability**
**3.5 Experimental Section**
**References**

## 3.1 Introduction

An incorporation of polymer additives in a perovskite precursor solution for enhancing the quality of the formed perovskite layer has been examined by some research groups.[1–7] For example, Grätzel *et al.* reported that a small amount of an addition of poly(methyl methacrylate) (PMMA) during the perovskite formation improved the quality of perovskite grains and gave a higher conversion efficiency.[8,9] On the other hand, Zhao *et al.* performed that an incorporation of poly(ethylene glycol) (PEG) as a self-healing scaffold of methylamine-lead chloride based perovskite formation improved the cell performance and durability.[10]

Processes of the perovskite layer formation could be considered as a crystal nucleation phase and a crystal growth phase, separately.[11–15] In the crystal nucleation phase, the incorporation of the polymer additives can decrease the surface energy of the crystal to promote the crystal nucleation, and nucleation simultaneously occurs in the entire phase owing to impure additives. In the crystal growth phase, the polymers with Lewis basic units (for example, O or N elements) form intermediates with $PbX_2$ of the perovskite precursor to decrease the growth rate of the nuclei produced by the above crystal nucleation step (Figure 3.1)[16–18] A homogeneous and high quality perovskite crystal layer with large grains and less grain boundaries can be formed by these two steps; the promoted crystal nucleation and the slow crystal growth.

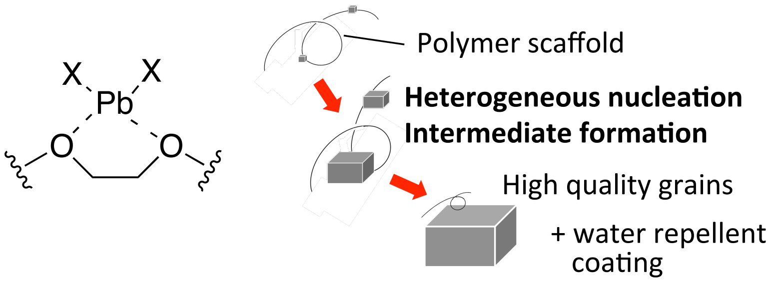

Figure 3.1 Intermediate of $PbX_2$ and Lewis base, and crystal growth with polymers

However, the most of conventional polymers are electrical insulators, and the addition of a certain amount of the polymers in the perovskite layers often suppressed their photovoltaic performance, especially the current density.

TEMPO, 1-oxy-2,2,6,6-tetramethylpiperidine, is a typical nitroxide radical characterized by redox-active via one-electron transfer reaction and robust under ambient air conditions.[19,20] The TEMPO molecule have been successfully enlarged to polymeric compounds, for example, poly(1-oxy-2,2,6,6-tetramethylpiperidin-4-yl methacrylate) (PTMA) and poly(1-oxy-2,2,6,6-tetramethylpiperidin-4-yl glycidyl ether) (PTGE), where the redox active nitroxide radical groups are densely introduced in the side chains of the polymers.[21–24] The TEMPO polymers have been applied as charge transporting and storing organic materials of secondary batteries.[25–32] The solid-state charge-transporting capability of the TEMPO polymers via a hopping conduction between the TEMPO substituents has also been described, for example, as a solid-type organic memory.[33–35] Boudouris *et al.* also proposed the extremely high charge-transporting capability of the TEMPO polymers in recent studies.[36–38] The TEMPO has also been used as a anti-oxidizing agent owing to its reactivity with free radicals, such as superoxide anion radical (Figure 3.2).[39–41]

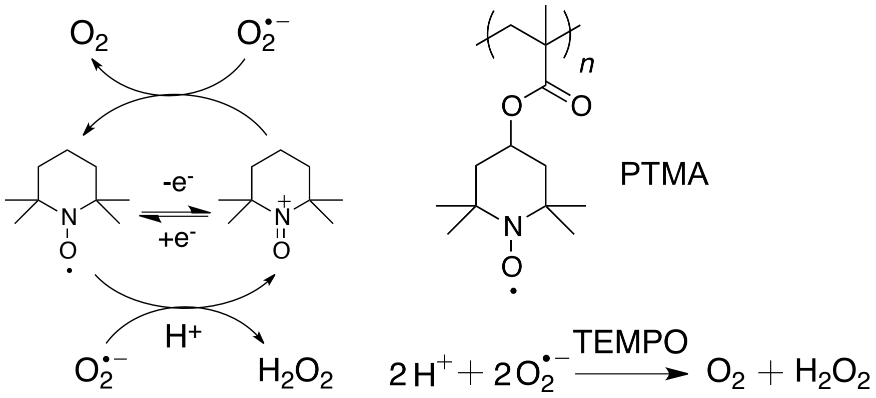

Figure 3.2 An anti-oxidizing mechanism of TEMPO and a molecular structure of PTMA

One remaining problem of the perovskite solar cells is the low durability derived from the decomposition of the perovskite compounds during exposing to ambient air.[42–47] Haque *et al.* pointed out the degradation of the organo-lead halide perovskite layer with ambient oxygen as an important issue.[48,49] They also proposed that the perovskite compounds were decomposed in an existence of only oxygen and light without any moisture, as follows: excited-electrons, in other words photocurrent, could be generated from the organo-lead halide perovskites, for example methylammonium lead triiodide ($CH_3NH_3PbI_3$), under light-irradiation, in which oxygen accepted the excited-electrons from the perovskite layer to generate superoxide anion radical ($O_2^{\bullet -}$). This superoxide anion radical decomposed the perovskite compounds to methylamine, lead iodide, and other materials (Figure 3.3).

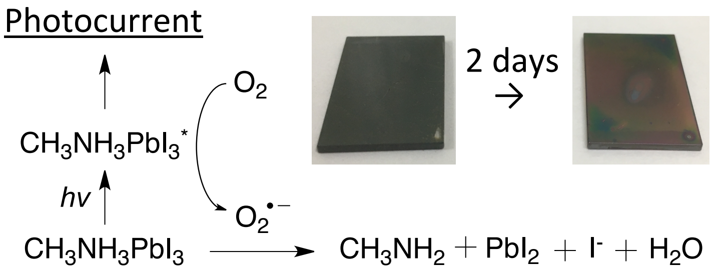

Figure 3.3 A degradation mechanism of the perovskite layers with oxygen and light.

An under layer of the perovskite solar cells is also one of the important factors to determine their photovoltaic performance and lifetime; in other words, a decomposition mechanism. Mesoporous titanium dioxide (*m*-$TiO_2$) is frequently applied as an effective under layer of a high quality perovskite layer and an electron-transporting layer of the cells.[50,51] On the other hand, $TiO_2$ is also well known as an oxidative catalyst of organic compounds to pollute organic materials by using ambient oxygen.[52–54] The decomposition of the perovskite compounds by oxygen on the surface of the *m*-$TiO_2$ layer under light-irradiation was one concern as an oxygen-triggered decomposition of the perovskite layer. Although $TiO_2$-free cells, such as the cells with planar tin oxide ($SnO_2$) as an under layer and an electron-transporting layer, have also been recently suggested as the high efficiency cells, the degradation of the perovskite compounds by ambient oxygen has remained an essential issue even in these cells.[55–57] The *m*-$TiO_2$ and planar $SnO_2$ were compared in terms of the causes of the perovskite decomposition (Figure 3.4).

In this chapter, the polymers with anti-oxidizing properties were incorporated in the perovskite layers to eliminate superoxide anion radical for enhancing the cell durability of the perovskite solar cells on *m*-$TiO_2$ and planar $SnO_2$ under layers.

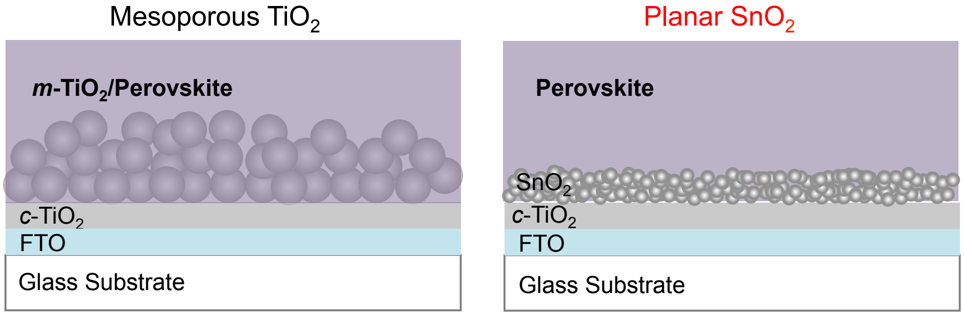

Figure 3.4 Perovskite solar cells with two types of under layers.

## 3.2 Polymer Incorporation as a Scaffold for High Quality Perovskite Layer Growth

For confirming a positive effect of the polymer-incorporation for forming high quality perovskite layers, ethylene glycol derivatives of 1,2-dimethylethane (DME), triethylene glycol dimethyl ether (TEGDME), and poly(ethylene glycol) (PEG) (molecular weight of 1,000 and 20,000) were added to $CH_3NH_3PbI_{3-x}Cl_x$ perovskite layer, which is formed by simple fabrication process but has a problem in homogeneous crystal formation.[10]

Two types of methods have been suggested about the incorporation of the polymers to the perovskite layers (Figure 3.5). One method is the polymer-incorporation in a poor solvent of an anti-solvent method, and the other method is in a perovskite precursor solution.[58–60] In a whole of this chapter, the latter method was selected because of the multiple applicability of fabrication processes, such as spin-coating, anti-solvent method, blade coating, and inkjet printing methods.

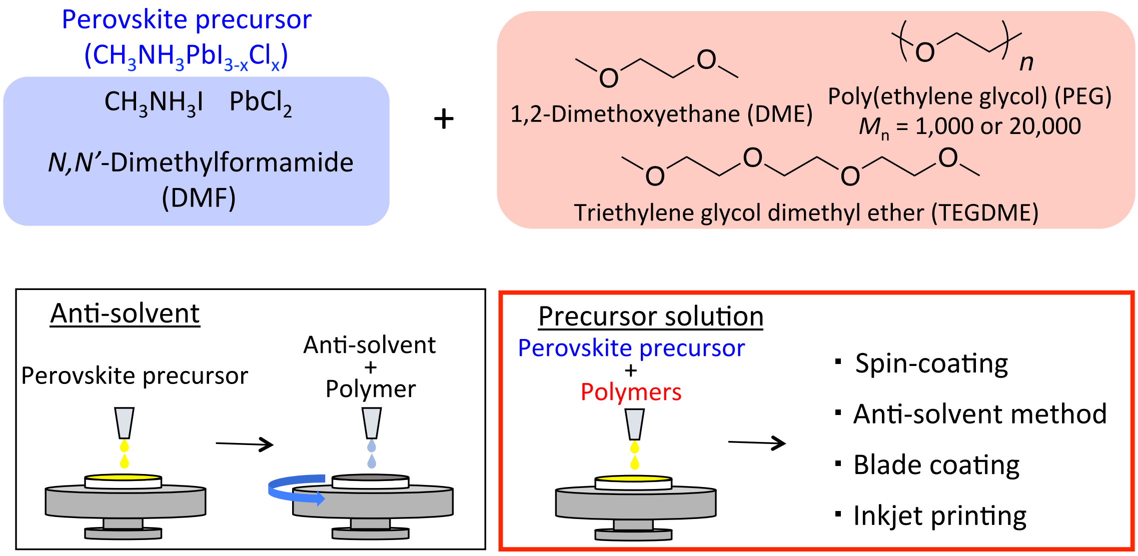

Figure 3.5 Molecular structures of ethylene glycol derivatives and schematic images of the two types of the perovskite layer formation.

The perovskite layers, which were formed by polymer-added $CH_3NH_3PbI_{3-x}Cl_x$ perovskite precursor solution by using the anti-solvent method, were microscopically observed by surface SEM images (Figure 3.6). DME, an example of low molecular weight ethylene glycol derivatives, gave an inhomogeneous perovskite layer; on the other hand, a homogeneous perovskite layer was obtained by the incorporation of PEG with a molecular weight of 20,000. The high molecular weight or poor solubility of the polymer contributed to the high quality perovskite crystal formation. The size of the perovskite crystallite was estimated by the full width of half maximum from X-ray diffraction (XRD) patterns (Figure 3.7).[61] The perovskite layers with the polymer additives showed the larger crystalline size than the layers without any additives and with low molecular weight derivatives (Table 3.1).

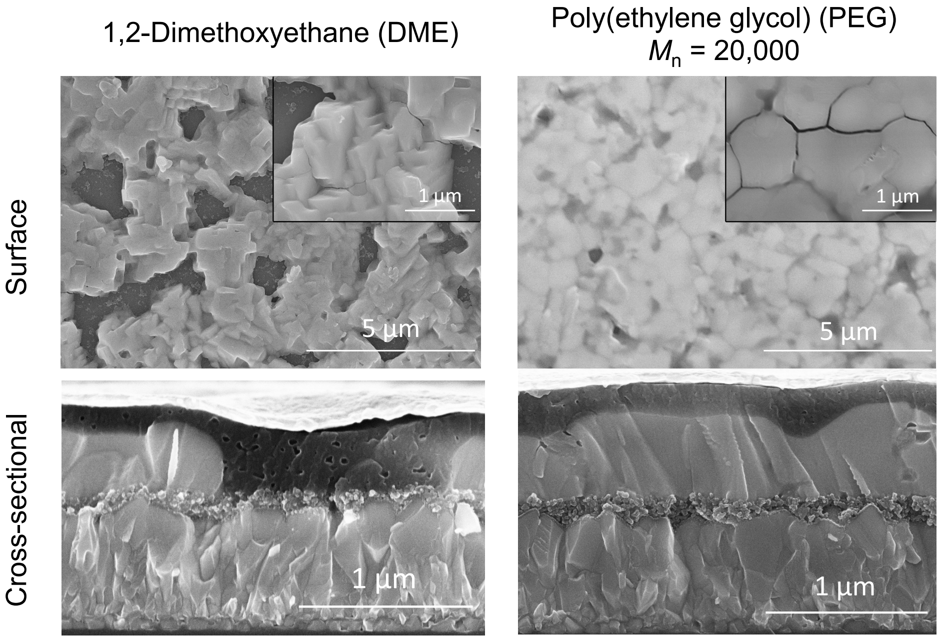

Figure 3.6 Surface and cross-sectional SEM images of perovskite layers fabricated with DME and $PEG_{20,000}$.

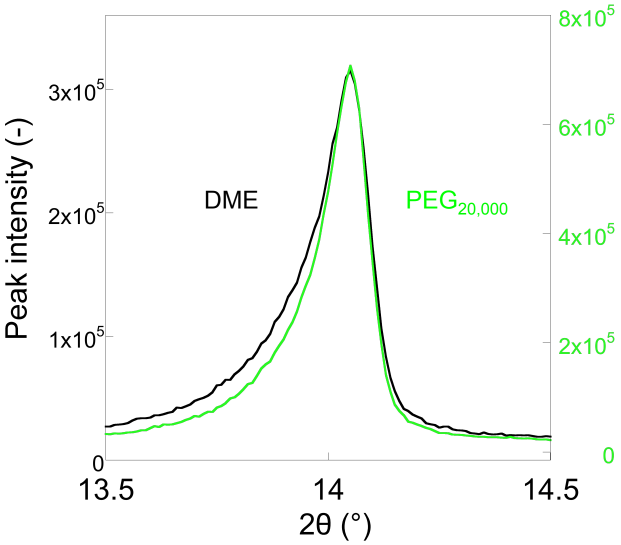

Figure 3.7 XRD patterns of the perovskite layers fabricated with DME and $PEG_{20,000}$.

The perovskite solar cells were fabricated with $CH_3NH_3PbI_{3-x}Cl_x$ perovskite layers including various ethylene glycol derivatives as additives. The highest photoelectric conversion efficiency of 11.1% was obtained with the incorporation of PEG with molecular weight of 20,000, which also possessed the largest and densest perovskite grains (Table 3.1, Figure 3.8). The short-circuit current density ($J_{SC}$) was particularly enhanced due to the dense perovskite layer and the open-circuit voltage ($V_{OC}$) was also improved owing to the large perovskite grain size. According to this result, the incorporation of the polymers with high molecular weight surely contributed to the superior photovoltaic conversion efficiency.

**Table 3.1** Crystal diameters and photovoltaic characteristics of perovskite solar cells fabricated with ethylene glycol derivatives

| Additives | $d$ (nm) | $J_{SC}$ (mA/cm$^2$) | $V_{OC}$ (V) | $FF$ (-) | $\eta$ (%) |
|---|---|---|---|---|---|
| - | 52 | 19.1 | 0.81 | 0.63 | 9.7 |
| DME | 51 | 18.8 | 0.76 | 0.66 | 9.4 |
| TEGDME | 47 | 17.6 | 0.73 | 0.67 | 8.7 |
| $PEG_{1,000}$ | 61 | 21.0 | 0.83 | 0.53 | 9.3 |
| $PEG_{20,000}$ | 67 | 20.7 | 0.96 | 0.56 | 11.1 |

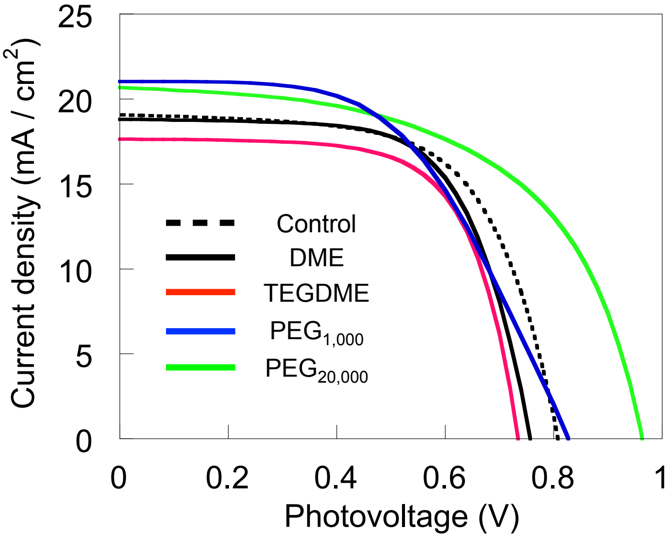

Figure 3.8 *J-V* curves of the perovskite solar cells fabricated with various ethylene glycol derivatives.

## 3.3 Anti-Oxidizing TEMPO Polymer-Incorporated Perovskite Layer and its Solar Cells

### 3.3.1 Perovskite layer fabricated with TEMPO polymers

$CH_3NH_3PbI_3$ perovskite layers with and without the incorporation of PTMA were prepared on *m*-$TiO_2$ or $SnO_2$ under layers: four specimens, respectively (Figure 3.9). In this chapter, poly[bis(4-phenyl)(2,4,6-trimethylphenyl)amine] (PTAA) was applied as a hole-transporting material of the cells. The existence of PTMA in the perovskite layer was confirmed by IR spectrum (Figure 3.10). A sharp and strong peak at 1714 $cm^{-1}$ was ascribed to the ester (C=O) substituents of PTMA, and was slightly shifted from the original location at 1725 $cm^{-1}$, which might show an interaction between PTMA and perovskite compounds, especially $PbI_2$.

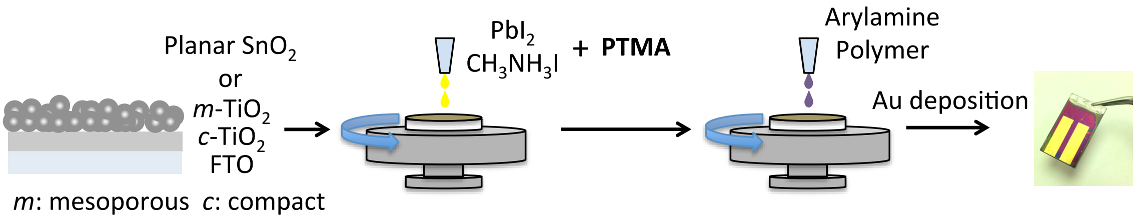

Figure 3.9 A fabrication process of the perovskite solar cells with the incorporation of PTMA.

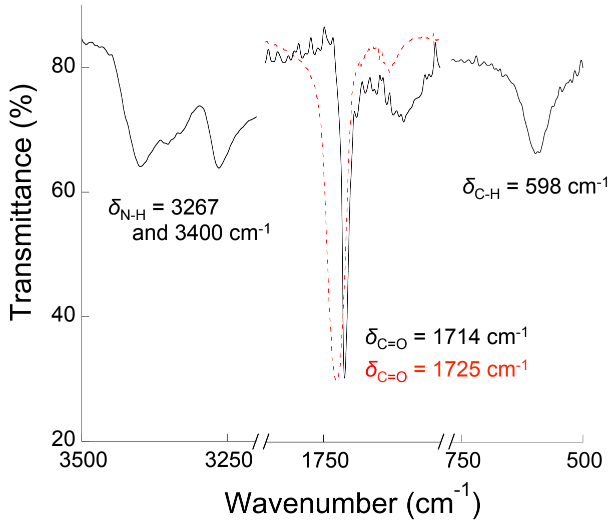

Figure 3.10 IR spectra of the perovskite layer fabricated with PTMA (black) and only PTMA (red).

The degradation of the perovskite layers was confirmed by using two types of detective methods of fluorometry and gas chromatography mass-spectrometry (GC-MS) (Figure 3.11). At the first method, the formation amounts of superoxide anion radical from the perovskite layers during 1 SUN irradiation in air condition were colorimetrically estimated by using a fluorescent probe, hydroethidine, which reacts with superoxide anion radical selectively and emits strong fluorescence light at 610−640 nm, as the previous paper.[48] A certain amount of superoxide anion radical was detected thorough the fluorescent light of 2-hydroethidium on the perovskite layers (Figure 3.12). Formation amounts and reaction rate of superoxide anion radical from the perovskite layer were calculated by using a standard curve of the fluorescent prove with known concentration (Table 3.2).

These results suggested that PTMA eliminated the generation of the superoxide anion radical dramatically, and the perovskite layer formed on *m*-$TiO_2$ emitted smaller amount of superoxide anion radical than the layer formed on $SnO_2$.

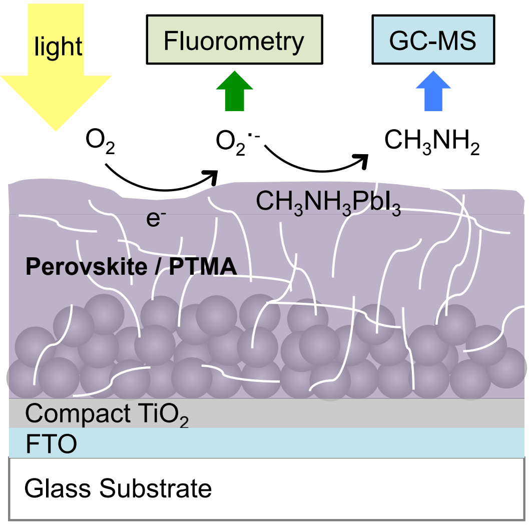

Figure 3.11 Schematic image of detective methods of the perovskite degradation.

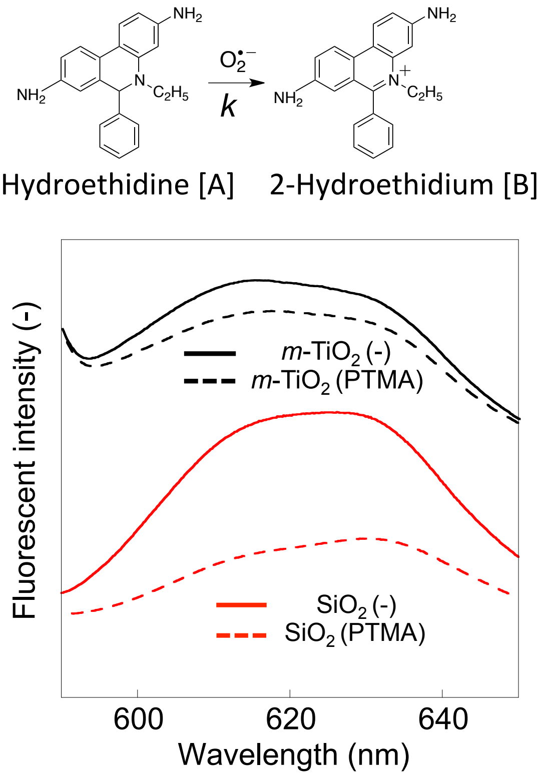

Figure 3.12 Elimination mechanism of superoxide anion radical by hydroethidine and fluorescent intensity of 2-hydroethidium on the perovskite layers.

**Table 3.2** Formation amounts (nmol/cm$^2$) and reaction rate (pmol/cm$^2$s) of superoxide anion radical from the perovskite layer

| Incorporation | Under layer | | | |
|---|---|---|---|---|
| | $m$-TiO$_2$ | $k$[A]$_{\mathrm{TiO2}}$ | SnO$_2$ | $k$[A]$_{\mathrm{SnO2}}$ |
| none | 11 | 2.0 | 24 | 4.4 |
| PTMA | 7.5 | 1.4 | 10 | 1.9 |

Methylamine, a gaseous decomposition fragment of the perovskite layer, was quantitatively monitored with gas chromatography. A standard peak of methylamine was detected by using a gaseous part of a bottle of 40 % methylamine solution in methanol. The time course of the generation amounts of methylamine from the perovskite layer of the four specimens placed in a sealed box under pure oxygen and 1 SUN irradiation is exhibited in Figure 3.13. Certain amounts of both superoxide anion radical and methylamine were significantly reduced with the incorporation of PTMA.

XRD patterns of the perovskite layers with and without the PTMA after 1 SUN irradiation in pure oxygen condition for 6 h were also recorded to confirm the progress of the degradation (inset of Figure 3.13). The perovskite layer without the incorporation of the PTMA showed the formation of $PbI_2$ decomposed from the perovskite compounds; on the other hand, the layer with PTMA did not indicate any obvious changes in the XRD.

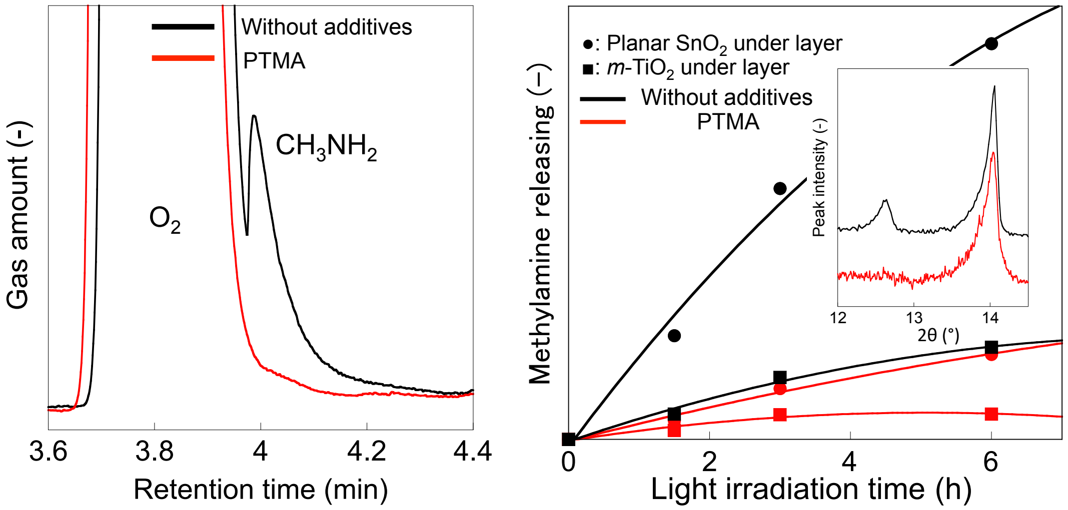

Figure 3.13 Left: GC-MS peaks of methylamine gas derived from the perovskite decomposition. Right: Generation amount of methylamine gas from the perovskite layer with different under layers. Inset: XRD patterns of the perovskite layers with and without PTMA after 1 SUN irradiation for 6 h under oxygen.

From the above results, a stoichiometric reaction equation for the degradation of $CH_3NH_3PbI_3$ perovskite under the light irradiation with ambient oxygen could be shown in Eq. 4.

$$\begin{aligned}&CH_3NH_3PbI_3 + h\nu \rightarrow CH_3NH_3PbI_3^{*} + O_2\\&\quad \rightarrow CH_3NH_3PbI_3 + O_2^{\cdot -} \rightarrow CH_3NH_2 + PbI_2 + 1/2I_2 + H_2O \quad \text{(Eq. 4)}\end{aligned}$$

Oxygen in ambient air reacts with electrons excited from the light-irradiated perovskite layer and generates the superoxide anion radical. The superoxide anion radical decomposes the perovskite compounds to fragments of methylamine gas, lead iodide, iodine, and water. The water might work as a proton for the eliminating cycle of TEMPO against superoxide anion radical.

The average sizes of the perovskite grains were estimated with full-width half maximum of the XRD patterns, which were 120 and 104 nm with and without the incorporation of PTMA on the *m*-$TiO_2$ under layer, and 72 and 51 nm with and without the incorporation of PTMA on the $SnO_2$ under layer, respectively (Figure 3.14). Incidentally, the perovskite grains formed with PMMA under same condition with PTMA, as a control experiment, gave an average size of 113 nm on the *m*-$TiO_2$ under layer in this chapter.[8] This larger grain boundary (smaller grain size) of the perovskite layers could be one reason for lower durability of them formed on the planar $SnO_2$ under layer because of more frequent oxygen-quenching or superoxide anion radical generation with the excited-electrons from the perovskite layer. Therefore, the perovskite layer on $SnO_2$ under layer decomposed harder than that on the *m*-$TiO_2$ under layer. An efficient charge-transporting behavior form the interface between perovskite grains to the mesoporous surface of the $TiO_2$ under layer might also contribute to the suppression of the superoxide anion radical formation due to the short lifetime of the excited-electrons. The surface SEM images of the perovskite layers with the PTMA incorporation also gave the large perovskite grains and the decreased grain boundaries (Figure 3.15). The small amount of the incorporation of PTMA was surely effective to obtain high quality perovskite grains with a larger grain size and smaller grain boundaries.

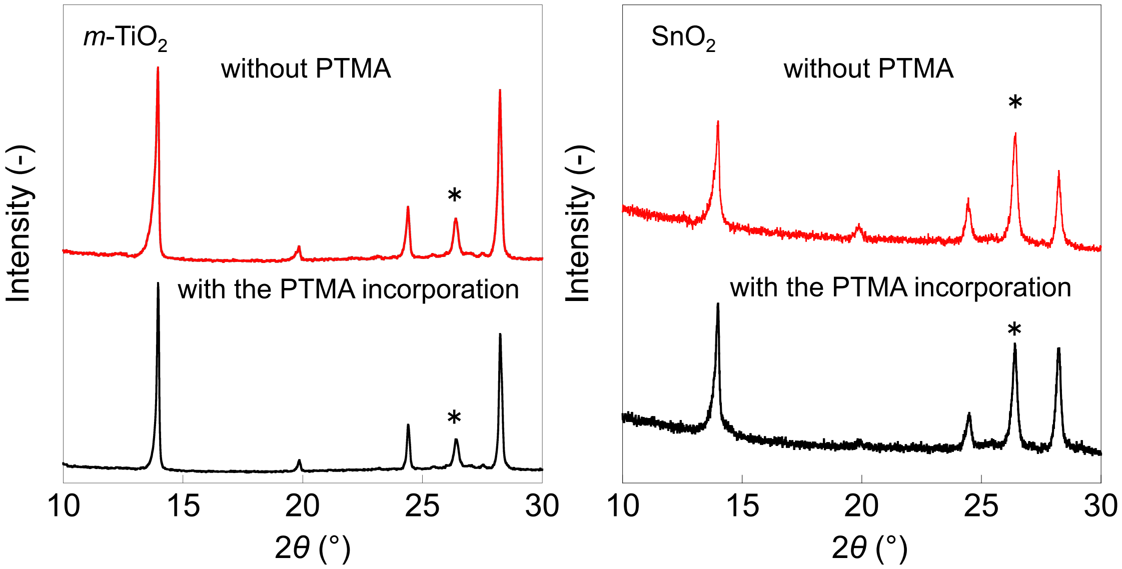

Figure 3.14 XRD patterns of the perovskite layers fabricated with and without PTMA on the $m$-$TiO_2$ and $SnO_2$ under layers.

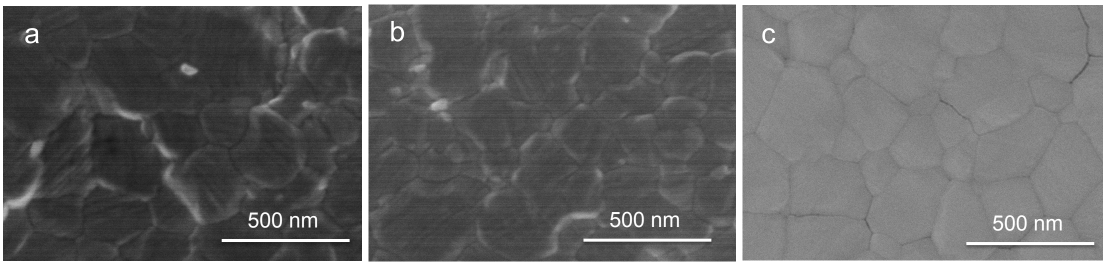

Figure 3.15 Surface SEM images of the perovskite layers (a: with PTMA, b: without any additives, and c: with PMMA).

PTMA is a typical organic material; therefore, its hydrophobic property enhanced the water-repelling property of the perovskite layer with the PTMA incorporation. The contact angles of the perovskite layer against water were increased from 40° to 64° and 80° by the incorporation of 0.3 and 1.0 wt% PTMA, respectively (Figure 3.16). Larger TEMPO substituents of PTMA in the side chains gave more hydrophobicity than the PMMA incorporation (68° with the incorporation of 1.0 wt% PMMA). The enhanced water-repellency might additionally improve the durability of the perovskite solar cells against ambient air including moisture.

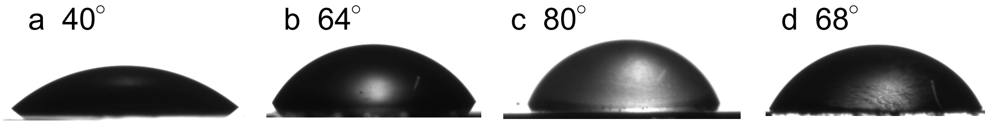

Figure 3.16 Contact angles of the perovskite layers against water (a: without any additives, b: with 0.3 wt% PTMA, c: with 1.0 wt% PTMA, and d: with 1.0 wt% PMMA).

The PTMA incorporated in the perovskite layer could capture superoxide anion radical formed by light-irradiation and oxygen exposure to suppress the degradation of the perovskite layer significantly, regardless of the under layers. As described above, the high quality perovskite grains with the incorporation of PTMA also contributed to the durability of the perovskite layer. Incidentally, nitroxide radical molecule, TEMPO itself, was also tried to be incorporated in the perovskite layer formation, but TEMPO is a sublimable material and is predicted to disappear during the perovskite formation, resulting low photovoltaic performance.

### 3.3.2 Photovoltaic performance of the cells with the incorporation of PTMA

The solar cells with a 4-cations perovskite layer consisted of methylamine, formamidine, cesium, and rubidium, which was also passivated with formamide hydrobromide, with the PTMA incorporation using the anti-solvent method were fabricated with the *m*-$TiO_2$ or $SnO_2$ under layer formed on a FTO/compact $TiO_2$ layer, a hole-transporting PTAA layer, and a deposited Au electrode.[62] The photovoltaic performance of the cells fabricated with the incorporation of the various polymers is listed in Table 3.3, and representative cells with and without the incorporation of 0.3 wt% PTMA on *m*-$TiO_2$ under layer are shown in Figure 3.17. The cell with PTMA exhibited the higher photovoltaic conversion efficiency of 18.8% than the control cell without PTMA: the efficiency of 18.2 %. A hysteresis in the *J*-*V* curves was not observed in the cells with the PTMA incorporation, probably owing to their high quality perovskite grains. The cells fabricated with the perovskite layers upon the planar $SnO_2$ under layer showed the conversion efficiency of 12.9 %. The cells with high efficiency on the planar structures were not obtained in this chapter, but the PTMA incorporation improved the photovoltaic performance and cell durability regardless of the under layer.

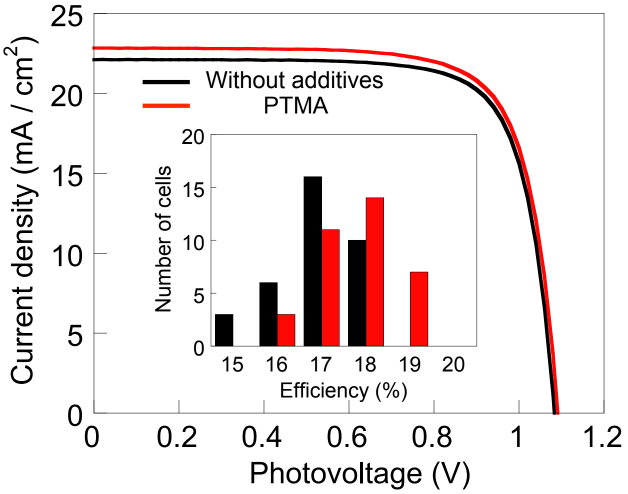

Figure 3.17 *J-V* curves of the perovskite solar cells fabricated with the PTMA on the *m*-$TiO_2$ layer. Inset: efficiency histogram of the perovskite cells fabricated with the PTMA incorporation and without PTMA.

**Table 3.3** Photovoltaic characteristics of the perovskite solar cells fabricated with the polymer incorporation

| Incorporation | wt%[b] | $J_{SC}$ (mA/cm$^2$) | $V_{OC}$ (V) | *FF* (-) | $\eta$ (%) |
|---|---|---|---|---|---|
| PTMA | 0 | 22.1 | 1.08 | 0.76 | 18.2 |
| | 0.1 | 22.5 | 1.08 | 0.75 | 18.3 |
| | 0.3 | 22.8 | 1.09 | 0.75 | 18.8 |
| | 0.6 | 22.5 | 1.05 | 0.74 | 17.6 |
| | 1 | 22.9 | 1.02 | 0.72 | 16.8 |
| PTAA | 0.3 | 16.2 | 0.85 | 0.36 | 4.9 |
| PTMA-H | 0.3 | 5.9 | 1.18 | 0.33 | 2.3 |
| PMMA | 0.3 | 19.6 | 1.01 | 0.73 | 14.5 |
| PTMA[a] | 0 | 22 | 0.96 | 0.53 | 11.3 |
| | 0.3 | 20.6 | 0.97 | 0.64 | 12.9 |

[a] The cells fabricated upon a planar $SnO_2$ under layer
[b] incorporation amount of the polymer vs. the perovskite.

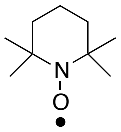
TEMPO

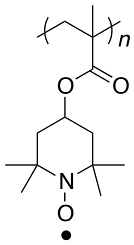
PTMA

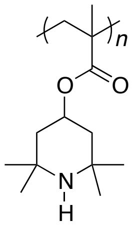
PTMA-H

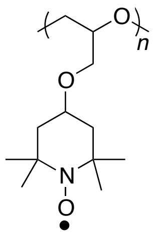
PTGE

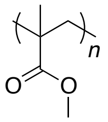
PMMA

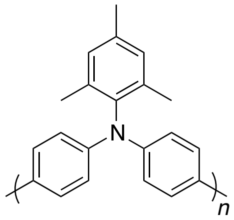
PTAA

Fluorescent intensity spectra of the perovskite layers formed with and without the incorporation of the PTMA and incident photon to current conversion efficiency (IPCE) spectra of the cells fabricated with the above perovskite layers also exhibited the increase of photocurrent and photovoltaic conversion efficiency owing to PTMA incorporation (Figure 3.18).

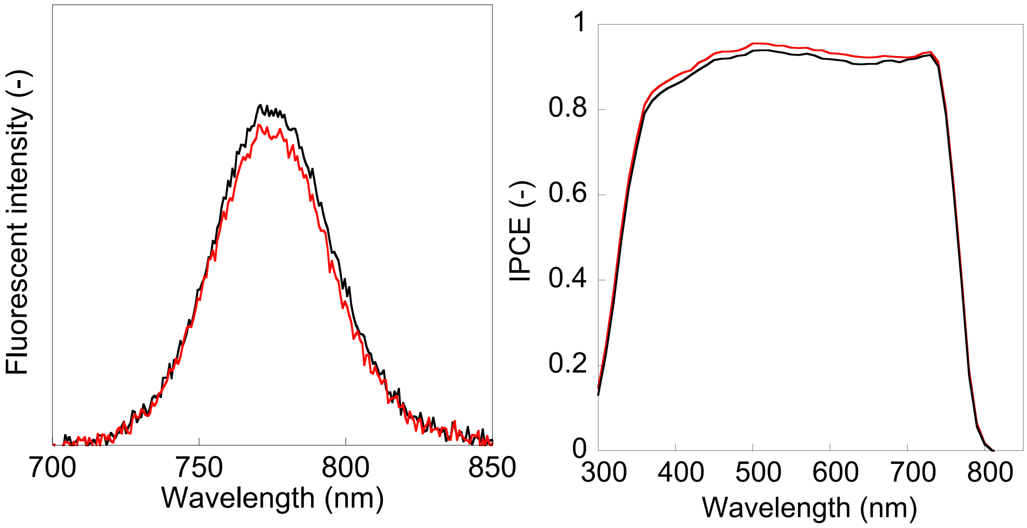

Figure 3.18 Fluorescent intensity and IPCE spectra of the perovskite layers (black: without any additives and red: with PTMA).

Other polymers have also been tried to incorporate in the perovskite layers. An incorporation of PTAA in the perovskite layer decreased the cell performance due to its work as a simple resistance in the perovskite layer (Table 3.3). The polymer with strict main chain structure might prevent the homogeneous perovskite layer formation. A non-radical precursor of PTMA, poly(2,2,6,6-tetramethylpiperidin-4-yl methacrylate) (PTMA-H), was also incorporated in the perovskite formation; its cell did also not work well. The XRD pattern also suggested to prevent the perovskite layer formation by PTMA-H probably because of an interaction between perovskite compounds and N-H groups of PTMA-H. Another TEMPO polymer, PTGE, was also examined, but the solubility of the polymer in the perovskite precursor solution, DMF, was lacked to apply. PMMA gave high quality perovskite grains as shown in Figure 3.15; however, the photovoltaic performance of the cell with a certain amount of PMMA was not improved.

The cell performance was also characterized by an impedance analysis of whole cells (Figure 3.19). The equivalent circuit consisted of three resistance, $R_{\mathrm{series}}$, $R_1$, and $R_2$, and two constant phase elements (CPE), $CPE_1$ and $CPE_2$, was selected.[63,64] $R_{\mathrm{series}}$ means the all resistances except for the resistances from the inside of the perovskite layer and each interlayer. The large semicircles, corresponding to $R_2$ and $CPE_2$, has been regarded to be determined by both a contact resistance between the perovskite layer and the electron-transporting layer and a resistance of the perovskite layer infiltrated into the mesoporous structure, as previously reported.[65] The incorporation of PTMA in the perovskite layer reduced the resistance of $R_2$ probably due to the polymeric charge-transporting capability as $R_{2,\,\mathrm{PTMA}} = 8.8\ \Omega$, $R_{2,\,\mathrm{without}} = 13\ \Omega$, and $R_{2,\,\mathrm{PMMA}} = 15\ \Omega$. These results proposed that the reduced resistance of the cells with the PTMA incorporation was ascribed to not the enlarged grain size but the chemical property of PTMA. As previously reported, the TEMPO polymers can transfer charges, mainly hole, via a hopping conduction governed by charge-coupling and reorganization energy (Marcus-Hush theory) using their redox substituents even in solid-state.[33-35] PTMA was expected to be located in the grain boundaries of the perovskite crystal layer; therefore, the charge-transportable PTMA could show the better electric properties than insulating cavity in the grain boundaries (Figure 3.19). $R_1$ and $CPE_1$ might be corresponded to the balk resistance in the perovskite layer, however there are a lot of hypotheses.

The cell durability was also analyzed by the impedance measurement. The impedance results of the light-irradiated cells showed higher $R_2$ value (control cell: 13.1 to 16.2 Ω and PTMA-incorporated cell: 8.8 to 11.3 Ω). On the other hand, $R_{\mathrm{series}}$ did not show obvious differences in the PTMA-incorporated cell (control cell: 11.1 to 14.8 Ω and PTMA-incorporated cell: 13.9 to 13.1 Ω), and $R_1$ also did not show meaningful values probably due to measurement inaccuracy in low-frequency region.

The fluorescence lifetime of the perovskite layer with the under layers (the simple device of FTO/compact $TiO_2$/*m*-$TiO_2$/perovskite with and without the PTMA) showed a significant decrease in the value of $\tau_1$: from 43 to 37 μs and $\tau_2$: from 143 to 120 μs with the incorporation of the PTMA (Figure 3.19). The TEMPO radical polymer acted as an efficient charge-carrier with a high conductivity based on its highly redox capability even in the solid-state devices, and it could improve the charge-transporting ability of the cells.

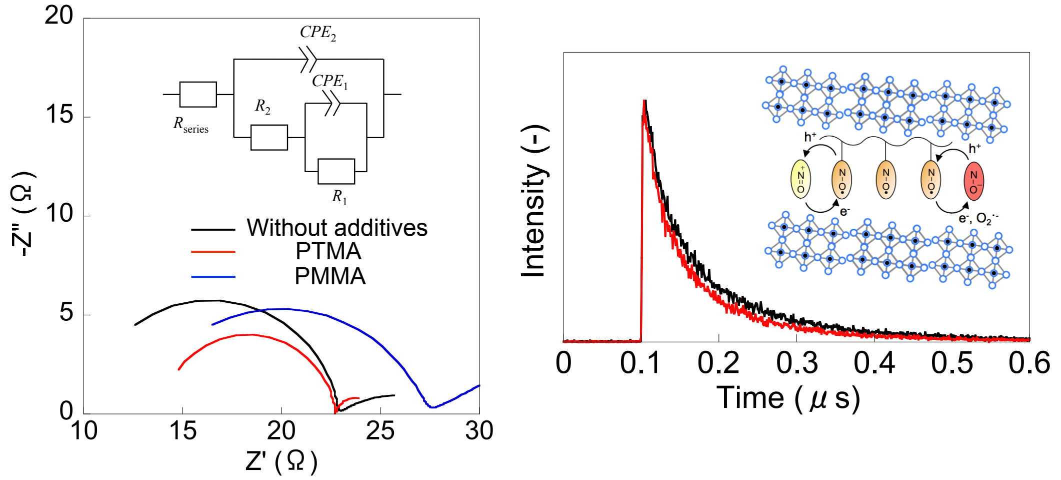

Figure 3.19 Left: Impedance spectra and an equivalent circuit of the perovskite solar cells measured under 1 SUN irradiation. Right: Fluorescence lifetime of the cells measured in emission wavelength of 760 nm and charge-transporting mechanism of PTMA in solid state.

**Table 3.4** Impedance data and fluorescent lifetime of the perovskite solar cells fabricated with PTMA

| Additives | $R_{series}$ (Ω) | $R_2$ (Ω) | $C_2$ (F) | $R_1$ (Ω) | $C_1$ (F) | $\tau_1$ (ns) | $\tau_2$ (ns) |
|---|---|---|---|---|---|---|---|
| - | 11 | 13 | 3.80E-08 | 3.3 | 1.60E-01 | 43 | 143 |
| PTMA | 14 | 8.8 | 1.10E-07 | 2 | 1.00E-01 | 37 | 120 |
| PMMA | 13 | 15 | 4.00E-08 | 3.7 | 3.90E+12 | - | - |

The perovskite solar cells fabricated with the incorporation of the PTMA exhibited much higher durability than the control cells without the PTMA under the condition of sequential light irradiation and air exposure without sealing of any layers (Table 3.5). The high durability and improved photovoltaic performance of the cells with the PTMA-incorporated perovskite layers could be ascribed to the multiple effects of the radical polymer, PTMA, as an anti-oxidizing agent, a water-repelling coating, and a scaffold for forming high quality perovskite layer with a sufficient charge-transporting capability.

**Table 3.5** Cell stability of the perovskite solar cells fabricated with PTMA

| Additives | Cell performance (%) | | Light→HTM |
|---|---|---|---|
| | 0 h | 250 h | (%) |
| - | 18.2 | 5.4 | 2.5 |
| PTMA | 18.8 | 13.2 | 6.1 |

## 3.4 Incorporation of Phenolic Antioxidants for Further Improvement of Cell Durability

### 3.4.1 Perovskite layers fabricated with anti-oxidizing phenolic compounds

Durability of the perovskite layer in ambient air is not enough for the practical use, even in dry air.[42] The organo-lead halide perovskite compounds were decomposed in the presence of only oxygen without any moisture under light irradiation, as described above (Figure 3.20).[48]

Phenolic antioxidants have been widely used in not only chemical products but also food and commodities due to their low environmental load and small affect for human bodies.[66,67] In this chapter, these phenolic antioxidants were also applied as additives in the perovskite precursor solution for further improvement of the durability of the perovskite solar cells. A well-known anti-oxidizing mechanism of the phenolic antioxidants is shown in Figure 3.20.[68,69] One molecule of the phenolic antioxidants reacts with two molecules of superoxide anion radical to eliminate the oxidation of the products. These antioxidants show a possibility to play an important role in the field of the perovskite solar cells, which have a problem of the degradation by ambient oxygen.

$$CH_3NH_3PbI_3 \xrightarrow{O_2^{\bullet -}} CH_3NH_2 + PbI_2 + I^- + H_2O$$

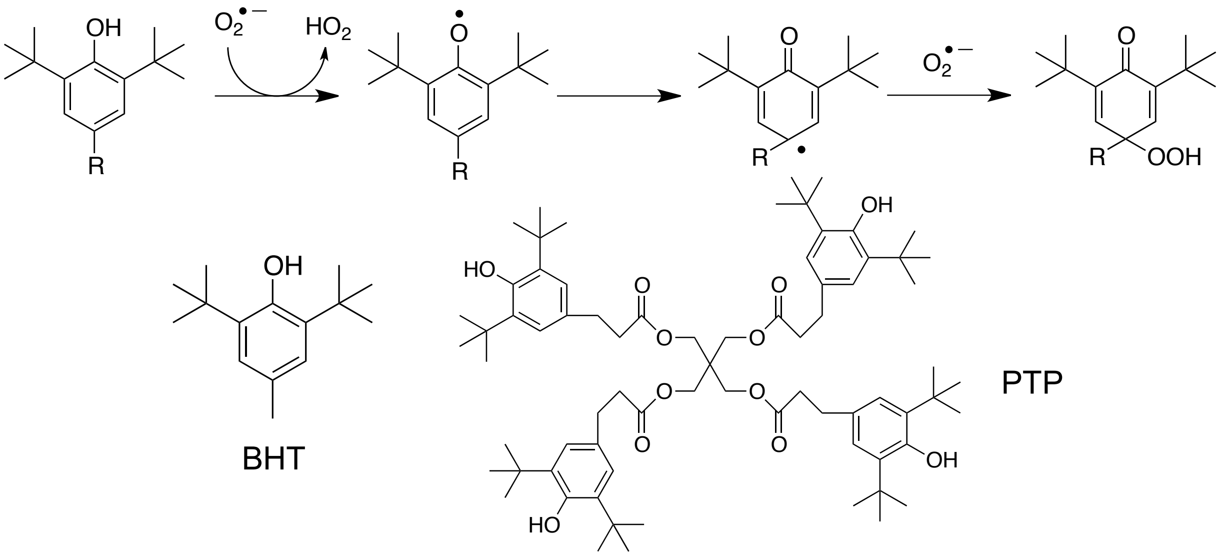

Figure 3.20 Degradation mechanism of the perovskite compounds with superoxide anion radical, elimination mechanism of superoxide anion radical with the phenolic antioxidants, and chemical structure of phenolic antioxidants.

Phenolic antioxidants, 2,6-di-*tert*-butyl-*p*-cresol (BHT) and pentaerythritol tetrakis[3-(3,5-di-*tert*-butyl-4-hydroxyphenyl)propionate] (PTP), were simply added to *N,N'*-dimethylformamide (DMF) solution of the perovskite precursor and was spin-coated to form the perovskite layers on *m*-$TiO_2$ under layer. A small amount (0.1 wt% vs. perovskite compounds) of antioxidants did not impede the perovskite layer formation and showed dense perovskite grains (Figure 3.21).

The hydrophobic phenolic antioxidants also improved the water-repelling property of the perovskite layers. Contact angles against water upon the perovskite layer were enhanced from 54° to 71° and 82° with the incorporation of BHT and PTP, respectively (Figure 3.22). The large molecular structure of PTP might contribute to the high water repellency. The water-repellency of the perovskite layers could additionally contribute to the durability of the perovskite cells in the humid condition.

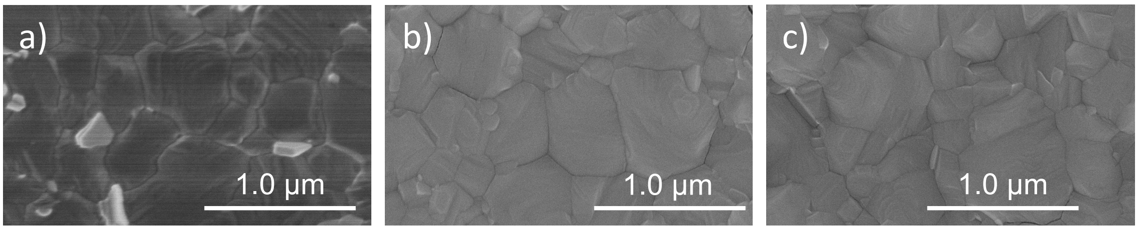

Figure 3.21 Surface SEM images of the perovskite layers fabricated with phenolic antioxidants (a: without any additives, b: with BHT, and c: PTP).

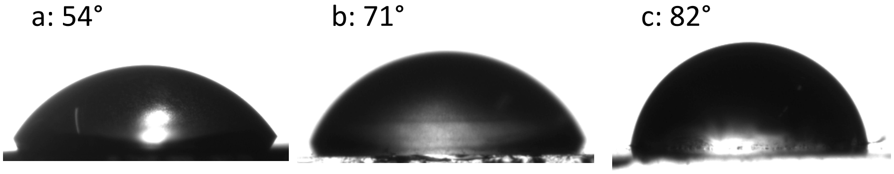

Figure 3.22 Contact angles of water upon the perovskite layers (a: without any additives, b: with the 1.0 wt% BHT, and c: with the 1.0 wt% PTP).

The average sizes of the perovskite crystallites estimated from the full width at half maximum of XRD patterns were not changed in the presence or absence of the anti-oxidizing additives; without any additives: 61 nm, with BHT: 61 nm, and with PTP: 57 nm. XRD patterns of the perovskite layers after 1 SUN irradiation for 12 h in oxygen condition are also shown in Figure 3.23. A generation amount of lead iodide, which is one of the decomposed fragments of the perovskite compounds, observed by

XRD patterns was suppressed owing to the antioxidant incorporation, whereas the perovskite layer without any additives indicated the significant formation of $PbI_2$ decomposed from the perovskite compounds. One molecule of the phenolic antioxidants could capture two molecules of superoxide anion radical to suppress the reaction of ambient oxygen with the perovskite compounds.

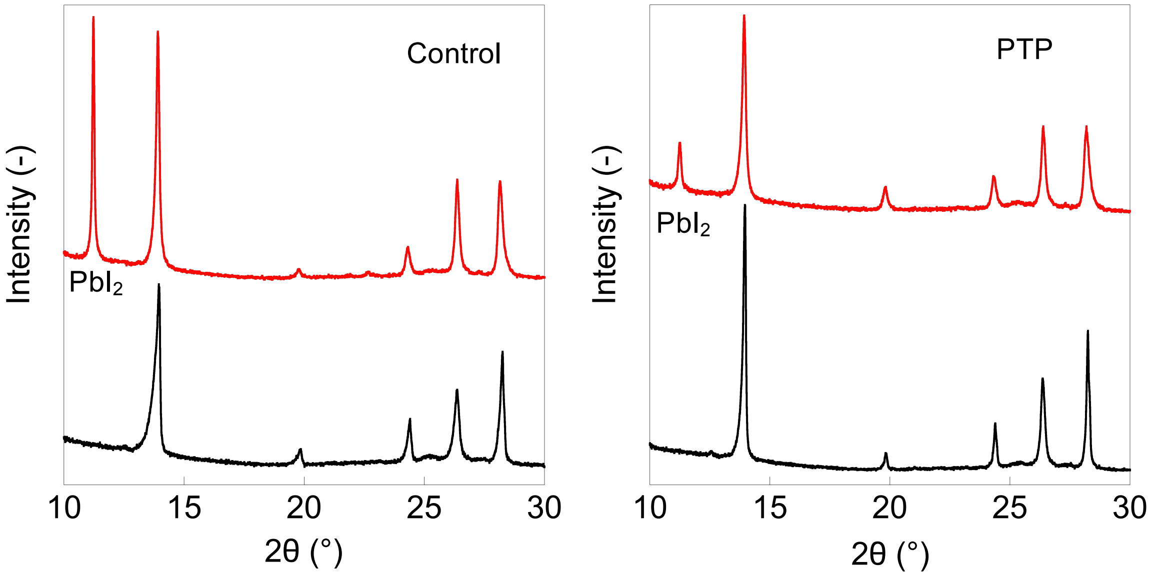

Figure 3.23 XRD patterns of the perovskite layers fabricated with PTP (black: before 1 SUN light irradiation and red: after light irradiation for 12 h).

### 3.4.2 Perovskite solar cells with phenolic antioxidants and their durability

The perovskite layers with the corporation of the phenolic antioxidants (using anti-solvent methods: a 4-cations perovskite formed with methylamine, formamidine, cesium, and rubidium) were formed on the *m*-$TiO_2$ under layer on the fluorine-doped tin oxide (FTO) covered with the compact $TiO_2$ layer. A hole-transporting layer of 2,2,7,7-tetrakis(*N,N*-di-*p*-methoxyphenylamine)-9,9-spirobifluorene (spiro-OMeTAD) and an Au electrode were spin-coated and deposited on the perovskite layer to fabricate the perovskite solar cells (Figure 3.24). As described above, the perovskite layer with the incorporation of the phenolic antioxidants did not impede the perovskite layer formation, and dense perovskite grains could be observed also in the cross-sectional SEM images (Figure 3.25). The photovoltaic performance of the cells with and without antioxidants is shown in Figure 3.26 and Table 3.6, representatively. The conversion efficiency was not largely reduced due to the incorporation of the small amount of insulating antioxidants, and their reproducibility was also confirmed (Inset of Figure 3.26).

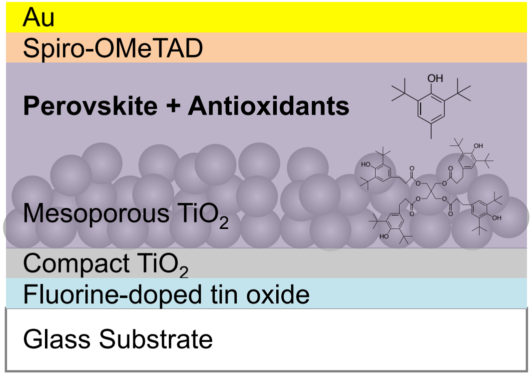

Figure 3.24 Schematic structure of the perovskite solar cells fabricated with the phenolic antioxidants.

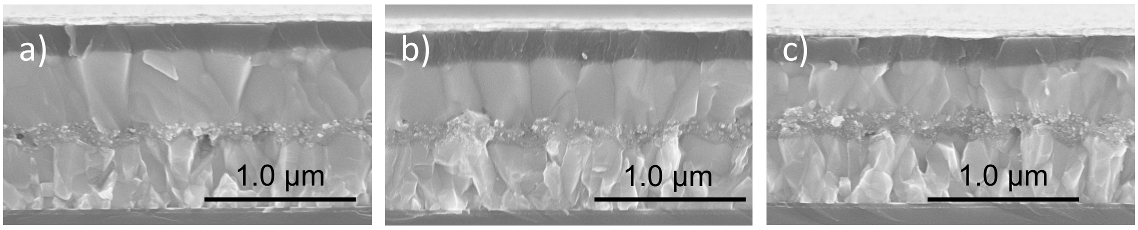

Figure 3.25 Cross-sectional SEM images of the perovskite solar cells fabricated with phenolic antioxidants (a: without any additives, b: with BHT, and c: PTP).

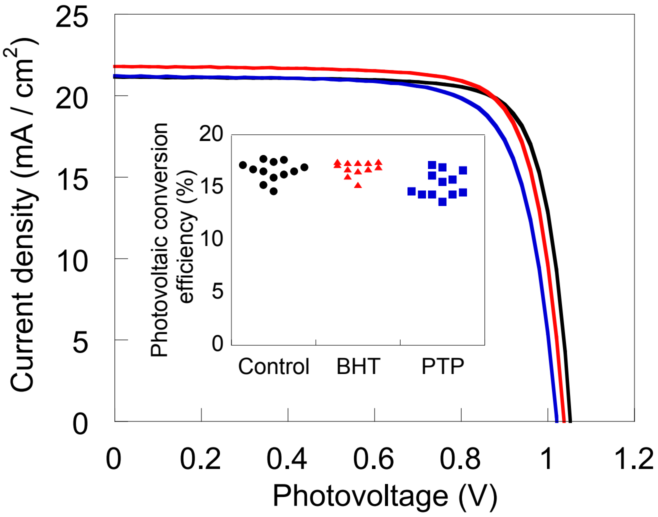

Figure 3.26 *J*-*V* curves of the perovskite solar cells fabricated with the phenolic antioxidants (black: without any additives, red: with BHT, and blue: with PTP). Inset: photovoltaic conversion efficiency of 12 cells in each condition.

**Table 3.6** The best photovoltaic conversion efficiency of the perovskite solar cells fabricated with the phenolic antioxidants.

| Additives | $J_{sc}$ (mA/cm$^2$) | $V_{oc}$ (V) | *FF* (-) | $\eta$ (%) |
|---|---|---|---|---|
| - | 21.3 | 1.06 | 0.79 | 17.8 |
| BHT | 21.7 | 1.06 | 0.76 | 17.5 |
| PTP | 20.6 | 1.06 | 0.79 | 17.2 |

The durability of the unsealed cells fabricated with the perovskite layers with the phenolic antioxidants under 1 SUN light-irradiation and dry air condition was shown in Figure 3.27. The cell durability was clearly enhanced with the incorporation of the phenolic antioxidants probably owing to the elimination of the superoxide anion radical and enhancement of the water repellency.

In conclusion, the small amount of the incorporation of phenolic antioxidants, BHT and PTP, in the mixed-cations perovskite layer did not decrease the quality of perovskite grains and its photovoltaic conversion performance, and, more importantly, suppressed the degradation of perovskite compounds and enhanced the cell durability by capturing superoxide anion radical generated from ambient air. This facile method provided a possibility for realizing durable and highly efficient perovskite solar cells. The incorporation of the antioxidants can be one candidate for enhancing photovoltaic characteristics of every perovskite solar cells.

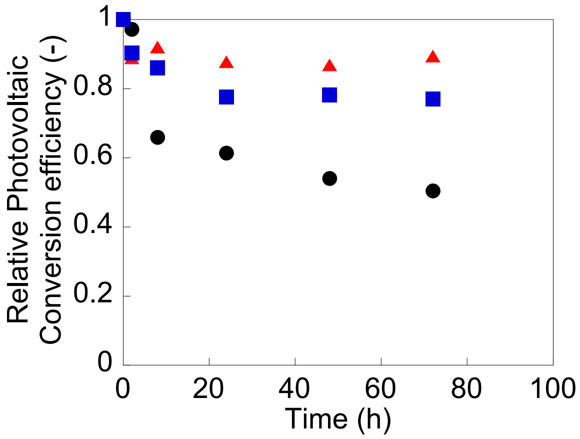

Figure 3.27 Durability of the unsealed perovskite solar cells under 1 SUN light irradiation and dry air exposure. (●: Control, ▲: BHT, and ■:PTP)

## 3.5 Experimental Section

### 3.5.1 Materials

PTMA (molecular weight of 46,000), PTMA-H (molecular weight of 46,000), and PTGE (molecular weight of 23,000) were prepared along previously reported methods.[25,27] PTAA (molecular weight of 7,000−10,000) and PMMA (molecular weight of 120,000) were purchased from Sigma-Aldrich Co.

### 3.5.2 Analysis of the perovskite decomposition

For analyzing of the decomposition of the perovskite layer, superoxide anion radical generated from the perovskite layers was estimated by the fluorescent intensity of a fluorescent probe, hydroethidine (dipping in 0.317 μM toluene solution), which reacts with superoxide to yield 2-hydroethidium with a fluorescence light emission from an excitation wavelength of 520 nm to 610−640 nm using a fluorescence spectrophotometer (F-7000, Hitachi, Ldt.), after 90 min of 1 SUN irradiation and oxygen exposure.[48] The formation amount of superoxide anion radical from the perovskite layer was calculated by using the calibration curve, which was created from the model solution in toluene of hydroethidine.

For measuring a gas chromatography-mass spectrometry (GC-MS), the perovskite layers (active area of 3.75 cm$^2$ and a thickness of ca. 0.5 μm) were decomposed by 1 SUN irradiation in a transparent cylindrical container (3 cm of the radius and 6 cm of the height) filled with pure oxygen. Methylamine gas generated from the perovskite layers was monitored with GC-MS system (78908-5977B, Aglient Technologies Ltd.), and a standard peak of methylamine was detected by using a gaseous part of a bottle of 40 % methylamine solution in methanol (Tokyo Chemical Industry).

### 3.5.3 Fabrication of the perovskite solar cells and their photovoltaic performance measurements

The perovskite solar cells were fabricated by referring a previous chapter.[62,70–72] A compact $TiO_2$ layer was deposited by spraying an ethanol solution of titanium diisopropoxide bis(acetylacetonate) of 4:1 volume ratio (Sigma-Aldrich Co.) on patterned FTO substrates by Zn powder and HCl aqueous solution. The *m*-$TiO_2$ under layer was formed by spin-coating of an ethanol solution of Ti paste (150 mg/ml, PST-18NR, JGC Catalysts and Chemicals Ltd.) on the compact $TiO_2$ layer at 4000 rpm for 20 s. After then, the substrates were annealed at 100 °C for 10 min, and immediately annealed at 500 °C for 1 h. The $SnO_2$ under layer was also formed by spin-coating of a 1.3 wt% $SnO_2$ colloidal solution (15% dispersion in water, Alfa Aesar Co.) diluted with pure water on the compact $TiO_2$ layer at 3000 rpm for 30 s. After then, the substrates were annealed at 150 °C for 30 min.

Three types of the perovskite layers, $CH_3NH_3PbI_{3-x}Cl_x$, $CH_3NH_3PbI_3$, and 4-cations perovskite, were prepared as described below. Firstly, methylamine hydroiodide (430 mg) and $PbCl_2$ (250 mg) were dissolved in *N*,*N*-dimethylformamide (DMF) for $CH_3NH_3PbI_{3-x}Cl_x$ precursor solution.[10] Secondly, methylamine hydroiodide (200 mg) and $PbI_2$ (578 mg) were dissolved in DMF (1 mL) for $CH_3NH_3PbI_3$ precursor solution. Finally, formamidine hydroiodide (172 mg), methylamine hydrobromide (22.4 mg), $PbI_2$ (507 mg), $PbBr_2$ (80.7 mg), CsI (16.3 mg) and RbI (13.4 mg) powders at a molar ratio of 1:0.2:1.1:0.22:0.063:0.066 were dissolved in a mixture of DMF (800 μL), dimethyl sulfoxide (114 μL) and acetonitrile (86 μL) for a 4-cations perovskite precursor solution. PTMA, phenolic antioxidants, and other polymers (0−1.0 wt% vs. the perovskite compounds) were simply added to these perovskite precursor solutions and stirred for 1 h. The perovskite solution was spin-coated on the under layers of *m*-$TiO_2$ or planar $SnO_2$ at 1000 rpm for 10 s to 6000 rpm for 20 s to form the perovskite layer by anti-solvent method using chlorobenzene drop-casting at 28 s from beginning. A formamidine hydrobromide solution (5.0 mg/mL in 2-propanol) was spin-coated at 5000 rpm for 30 s to reform the perovskite layer at chapter 3.3. PTAA (10 mg in 1 mL toluene) with 7.5 μL lithium bis-(trifluoromethylsulfonyl) imide (170 mg/mL in acetonitrile) and 4.0 μL tert-butylpyridine as a hole-transporting layer was spin-coated on the perovskite layer at 4000 rpm for 20 s. Finally, a 100 nm Au electrode was deposited on the hole-transporting PTAA layer using a vacuum chamber (VPC-1100, ULVAC, Inc.). The completed cells were kept for a few days in a dry room before their performance analysis.

The current–voltage measurements under AM 1.5 standard solar irradiation were performed with a solar cell evaluation system (YQ-2000, JASCO Co.) and a solar simulator (CEP-2000MLQ, Bunkoukeiki Co.).

### 3.5.4 Measurements

X-Ray patterns were measured with an X-ray diffractometer using a focused beam method (LINT-UltimaIII, Rigaku Co.). IR spectrum of a KBr pellet formed with the curbed perovskite compounds was measured with an IR spectrophotometer (V670, JASCO Co.). The fluorescence lifetime of the simple device (FTO/compact $TiO_2$/$m$-$TiO_2$/perovskite with and without the incorporation of PTMA) was measured using a fluorescence lifetime spectrometer (C11367, Hamamatsu Photonics Co.). A scanning electron microscope (SU8000, Hitachi, Ldt.) was used to obtain surface and cross-sectional SEM images of the perovskite layers and the solar cells. The contact angles vs. water were observed with a contact angle analyzer (DSA-25S, KRÜSS GmbH). Impedance spectra were analysed with impedance analyser (SI 1260, TOYO Co.), and the equivalent circuit was referred by previous paper.[63–65]

### 3.5.5 Detail of the impedance measurement

0. Preparation

Whole or a part of solar cells were fabricated as usual.

1. Setting

Two impedance analyzers (TOYO Co.) need to wait for 10 min, and a solar simulator needs to wait for 30 min. (If you do not need a solar simulator, you can measure impedance spectra in Waseda)

●The solar simulator was turned on by rising a breaker and turning ON/OFF switch and a shutter ON.

●The sunlight rises the temperature in the chamber; therefore, environment chamber should be turned on at 25°C.

●Turning on two impedance analyzers (TOYO Co.). The order is not important. Power switch is back side of the upper analyzer, and left of front side of lower analyzer.

●Turning on the PC. User name and password are put on a monitor of the PC.

2. Measurement preparation

●Opening a software “Zplot”. A measurement condition should be optimized on each perovskite compounds or cell configurations. (An example of the measurement condition of 4-cations perovskite solar cells and $m$-$TiO_2$ under layer is written below.)

Ctrl E Sweep Freq.: Constant voltage and swept frequency

DC Potential:

a. 0.8-1.0 V vs. Reference in dark condition, depending on the reference publication.

b. vs. Open circuit in sun light irradiation. ✓ on Monitor Cell Potential gives Voc.

AC Amplitude: 10mV

Initial Frequency: 10×E6or7 Hz Logarithmic

Final Frequency: 0.1 Hz Steps/Decade Interval 10

●Connecting the cell via using additional clips on green board (All equipment is on the chamber.)

Au side connects Working and FTO side connects Reference.

## 3. Measurement

Pushing semi-circle button started the measurements.

"Z View" on desktop of PC showed a real-time Cole-Cole plot. Appearing semi-circle means success, if not, the connection should be retried. (right click and "Autoscale" can show the appropriate plot.)

The data of low frequency is generally hard to take.

After measuring, save the measurement in Z data and right-click on Cole-Cole plot and Bode plot to save as text files.

Turn off the equipment and PC at the end.

## 4. Analysis (ZspimWin 3.2)

4.1 Create a text file for software by an excel file of "solartron_analysis (Made by Dr. Kan Hatakeyama" Only choose the Z file (auto).

4.2 Open ZsimpWin and file created in 4.1. Cut the outliers by operating txt file directly.

4.3 Set equivalent circuit by yellow bottom of "circuit". (resistance: R capacitance: C CPE: Q)

4.4 Save the fitting data, which is broadly similar with actual data. "Save parameters" can save each value. "Save impedance data" can save fitting curve. Save results with this filename should be "No".

5. Data application

If CPE (Q) was used for equivalent circuit, the capacitance could be calculated by below equation.

$$C = Q^{\frac{1}{n}} \cdot R^{\frac{1-n}{n}}$$

Comparison of resistance is quite simple.

Some cells show inductance with additional curves (often in dark condition).

## References

[1] A. Fakharuddin, M. Seybold, A. Agresti, S. Pescetelli, F. Matteocci, M. I. Haider, S. T. Birkhold, H. Hu, R. Giridharagopal, M. Sultan, et al., *ACS Appl. Mater. Interfaces* **2018**, *10*, 42542–42551.
[2] C. Sun, Y. Guo, B. Fang, J. Yang, B. Qin, H. Duan, Y. Chen, H. Li, H. Liu, *J. Phys. Chem. C* **2016**, *120*, 12980–12988.
[3] Q. Liang, J. Liu, Y. Han, *Org. Electron.* **2018**, *62*, 26–34.
[4] B. R. Sutherland, *Joule* **2018**, *2*, 820–822.
[5] B. Li, Y. Zhang, L. Fu, T. Yu, S. Zhou, L. Zhang, L. Yin, *Nat. Commun.* **2018**, *9*, 1–8.
[6] Z. Huang, X. Hu, C. Liu, L. Tan, Y. Chen, *Adv. Funct. Mater.* **2017**, *1703061.*
[7] J. Jiang, Q. Wang, Z. Jin, X. Zhang, J. Lei, H. Bin, Z. Zhang, *Adv. Energy Mater.* **2017**, *1701757.*
[8] D. Bi, C. Yi, J. Luo, J. D. Décoppet, F. Zhang, S. M. Zakeeruddin, X. Li, A. Hagfeldt, M. Grätzel, *Nat. Energy* **2016**, *1*, 1–5.
[9] X. Jia, Z. Hu, J. Xu, L. Huang, J. Zhang, J. Zhang, Y. Zhu, *Mater. Res. Bull.* **2017**, *95*, 216–222.
[10] Y. Zhao, J. Wei, H. Li, Y. Yan, W. Zhou, D. Yu, Q. Zhao, *Nat. Commun.* **2016**, *7*, 1–9.
[11] T. Udayabhaskararao, M. Kazes, L. Houben, H. Lin, D. Oron, *Chem. Mater.* **2017**, *29*, 1302–1308.
[12] S. C. Watthage, Z. Song, G. K. Liyanage, A. B. Phillips, M. J. Heben, *2016 IEEE 43rd Photovolt. Spec. Conf.* **2016**, *2*, 831–834.
[13] Y. Zhou, O. S. Game, S. Pang, N. P. Padture, *J. Phys. Chem. Lett.* **2015**, *6*, 4827–4839.
[14] K. Sangwal, *Nucleation and Crystal Growth : Metastability of Solutions and Melts*, Hoboken, NJ : John Wiley & Sons, **2018**.
[15] J. W. P. Schmelzer, *Nucleation Theory and Applications*, Weinheim : Wiley-VCH, **2005**.
[16] J. J. Choi, M. R. Alpert, A. F. Harper, D. Smilgies, *J. Mater. Chem. A* **2017**, *5*, 113-123.
[17] T. Han, J. Lee, C. Choi, S. Tan, C. Lee, Y. Zhao, Z. Dai, N. De Marco, S. Lee, S. Bae, et al., *Nat. Commun.* **2019**, *10*, 1–10.
[18] Y. Zong, Y. Zhou, S. Pang, Y. Zong, Y. Zhou, Y. Zhang, Z. Li, L. Zhang, M. Ju, M. Chen, *Chem* **2018**, *4*, 1404–1415.

[19] P. L. Bragd, A. C. Besemer, H. Van Bekkum, *J. Mol. Catal. A Chem.* **2001**, *170*, 35–42.
[20] M. V. N. De Souza, *TEMPO (2,2,6,6-Tetramethylpiperidine-N-Oxyl) an Important Reagent in Alcohol Oxidation and Its Application in Synthesis of Natural Products*, **2006**.
[21] K. Oyaizu, H. Nishide, in *Handb. Conduct. Polym.* (Eds.: Reynolds J.R., T. Skotheim, B. Thompson), CRC Press/Taylor & Francis, Boca Raton, **2019**, pp. 587–594.
[22] H. Nishide, K. Oyaizu, *Science* **2008**, *319*, 737–738.
[23] K. Oyaizu, H. Nishide, *Adv. Mater.* **2009**, *21*, 2339–2344.
[24] K. Nakahara, K. Oyaizu, H. Nishide, *Chem. Lett.* **2011**, *40*, 222–227.
[25] H. Nishide, S. Iwasa, Y. J. Pu, T. Suga, K. Nakahara, M. Satoh, *Electrochim. Acta* **2004**, *50*, 827–831.
[26] X. Lang, J. Zhao, X. Chen, *Angew. Chem. Int. Ed.* **2016**, *55*, 4697–4700.
[27] T. Sukegawa, K. Sato, K. Oyaizu, H. Nishide, *RSC Adv.* **2015**, *5*, 15448–15452.
[28] Y. Yonekuta, K. Susuki, K. Oyaizu, K. Honda, H. Nishide, *J. Am. Chem. Soc.* **2007**, *129*, 14128–14129.
[29] K. Sato, R. Ichinoi, R. Mizukami, T. Serikawa, Y. Sasaki, J. Lutkenhaus, H. Nishide, K. Oyaizu, *J. Am. Chem. Soc.* **2018**, *140*, 1049–1056.
[30] K. Sato, T. Mizuma, H. Nishide, K. Oyaizu, *J. Am. Chem. Soc.* **2017**, *139*, 13600–13603.
[31] T. Sukegawa, I. Masuko, K. Oyaizu, H. Nishide, *Macromolecules* **2014**, *47*, 8611–8617.
[32] T. Suga, H. Ohshiro, S. Ugita, K. Oyaizu, H. Nishide, *Adv. Mater.* **2009**, *21*, 1627–1630.
[33] T. Suga, S. Takeuchi, T. Ozaki, M. Sakata, K. Oyaizu, H. Nishide, *Chem. Lett.* **2009**, *38*, 1160–1161.
[34] K. Saito, K. Hirose, T. Okayasu, H. Nishide, M. T. W. Hearn, *RSC Adv.* **2013**, *3*, 9752–9756.
[35] T. Suga, M. Sakata, K. Aoki, H. Nishide, *ACS Macro Lett.* **2014**, *3*, 703–707.
[36] S. H. Sung, B. M. Savoie, B. W. Boudouris, Y. Joo, V. Agarkar, *Science* **2018**, *359*, 1391–1395.
[37] L. Zheng, S. Mukherjee, K. Wang, M. E. Hay, B. W. Boudouris, X. Gong, *J. Mater. Chem. A* **2017**, *5*, 23831–23839.
[38] L. Rostro, S. H. Wong, B. W. Boudouris, *Macromolecules* **2014**, *47*, 3713–3719.
[39] T. Yoshitomi, Y. Yamaguchi, A. Kikuchi, Y. Nagasaki, *Acta Biomater.* **2012**, *8*, 1323–1329.
[40] M. C. Krishna, D. A. Grahame, A. Samuni, J. B. Mitchell, A. Russo, *Proc. Natl. Acad. Sci.* **1992**, *89*, 5537–5541.
[41] T. Yoshitomi, A. Hirayama, Y. Nagasaki, *Biomaterials* **2011**, *32*, 8021–8028.
[42] M. I. Asghar, J. Zhang, H. Wang, P. D. Lund, *Renew. Sustain. Energy Rev.* **2017**, *77*, 131–146.
[43] G. Niu, X. Guo, L. Wang, *J. Mater. Chem. A* **2015**, *3*, 8970–8980.
[44] Y. Han, S. Meyer, Y. Dkhissi, K. Weber, J. M. Pringle, U. Bach, L. Spiccia, Y.-B. Cheng, *J. Mater. Chem. A* **2015**, *3*, 8139–8147.
[45] J. Wei, H. Li, Y. Zhao, W. Zhou, R. Fu, Y. Leprince-Wang, D. Yu, Q. Zhao,

*Nano Energy* **2016**, *26*, 139–147.
[46] W. Luo, C. Wu, D. Wang, Y. Zhang, Z. Zhang, X. Qi, N. Zhu, X. Guo, B. Qu, L. Xiao, et al., *ACS Appl. Mater. Interfaces* **2019**, *11*, 9149–9155.
[47] A. K. Baranwal, S. Kanaya, T. A. N. Peiris, G. Mizuta, T. Nishina, H. Kanda, T. Miyasaka, H. Segawa, S. Ito, *ChemSusChem* **2016**, *9*, 2604–2608.
[48] N. Aristidou, I. Sanchez-Molina, T. Chotchuangchutchaval, M. Brown, L. Martinez, T. Rath, S. A. Haque, *Angew. Chem. Int. Ed.* **2015**, *54*, 8208–8212.
[49] D. Bryant, N. Aristidou, S. Pont, I. Sanchez-molina, T. Chotchunangatchaval, S. Wheeler, R. Durrant, S. A. Haque, *Energy Environ. Sci.* **2016**, *9*, 1655–1660.
[50] F. T. F. O'Mahony, Y. H. Lee, C. Jellett, S. Dmitrov, D. T. J. Bryant, J. R. Durrant, B. C. O'Regan, M. Graetzel, M. K. Nazeeruddin, S. A. Haque, *J. Mater. Chem. A* **2015**, *3*, 7219–7223.
[51] F. Giordano, A. Abate, J. P. Correa Baena, M. Saliba, T. Matsui, S. H. Im, S. M. Zakeeruddin, M. K. Nazeeruddin, A. Hagfeldt, M. Graetzel, *Nat. Commun.* **2016**, *7*, 10379.
[52] K. Hashimoto, H. Irie, A. Fujishima, *Japanese J. Appl. Physics, Part 1 Regul. Pap. Short Notes Rev. Pap.* **2005**, *44*, 8269–8285.
[53] A. Fujishima, T. N. Rao, D. A. Tryk, *J. Photochem. Photobiol. C Photochem. Rev.* **2000**, *1*, 1–21.
[54] M. Pelaez, N. T. Nolan, S. C. Pillai, M. K. Seery, P. Falaras, A. G. Kontos, P. S. M. Dunlop, J. W. J. Hamilton, J. A. Byrne, K. O'Shea, et al., *Appl. Catal. B Environ.* **2012**, *125*, 331–349.
[55] Q. Jiang, X. Zhang, J. You, *Small* **2018**, *14*, 1–14.
[56] L. Xiong, Y. Guo, J. Wen, H. Liu, G. Yang, P. Qin, G. Fang, *Adv. Funct. Mater.* **2018**, *28*, 1–18.
[57] Y. Lee, S. Lee, G. Seo, S. Paek, K. T. Cho, A. J. Huckaba, M. Calizzi, D. won Choi, J. S. Park, D. Lee, et al., *Adv. Sci.* **2018**, *5*, 1–6.
[58] Y. Cai, Z. Zhang, Y. Zhou, H. Liu, Q. Qin, X. Lu, X. Gao, L. Shui, S. Wu, J. Liu, *Electrochim. Acta* **2018**, *261*, 445–453.
[59] F. Li, J. Yuan, X. Ling, Y. Zhang, Y. Yang, S. H. Cheung, *Adv. Funct. Mater.* **2018**, *1706377*.
[60] P. Qin, G. Yang, Z. Ren, S. H. Cheung, S. K. So, L. Chen, *Adv. Mater.* **2018**, *1706126*, 1–12.
[61] Y. Ding, X. Yao, X. Zhang, C. Wei, Y. Zhao, *J. Power Sources* **2014**, *272*, 351–355.
[62] F. Bella, G. Griffini, J. P. Correa-Baena, G. Saracco, M. Grätzel, A. Hagfeldt, S. Turri, C. Gerbaldi, *Science* **2016**, *354*, 203–206.
[63] A. Todinova, L. Contreras-Bernal, M. Salado, S. Ahmad, N. Morillo, J. Idígoras, J. J. A. Anta, *ChemElectroChem* **2017**, *4*, 2891–2901.
[64] M. Anaya, W. Zhang, B. C. Hames, Y. Li, F. Fabregat-Santiago, M. E. Calvo, H. J. Snaith, H. Míguez, I. Mora-Seró, *J. Mater. Chem. C* **2017**, *5*, 634–644.
[65] A. Dualeh, T. Moehl, N. Tétreault, J. Teuscher, P. Gao, M. K. Nazeeruddin, M. Grätzel, *ACS Nano* **2014**, *8*, 362–373.
[66] S. Kumar, Y. Choi, S. Kang, N. K. Oh, J. Lee, J. Seo, M. Jeong, H. W. Kwon, S. Il Seok, C. Yang, et al., *ACS Appl. Mater. Interfaces* **2019**, *11*, 38828–38837.
[67] B. Dimitrios, *Trends Food Technol.* **2006**, *17*, 505–512.

[68] F. Shahidi, P. K. Janitha, P. D. Wanasundara, *Crit. Rev. Food Sci. Nutr.* **1992**, *32*, 67–103.
[69] M. C. Foti, *J. Pharm. Pharmacol.* **2007**, *59*, 1673–1685.
[70] K. Suwa, S. Tanaka, K. Oyaizu, H. Nishide, *Polym. Int.* **2018**, *67*, 670–674.
[71] W. Okada, T. Suga, K. Oyaizu, H. Segawa, H. Nishide, *ACS Appl. Energy Mater.* **2019**, *2*, 2848-2853.
[72] H. Maruo, Y. Sasaki, K. Harada, K. Suwa, *Polym. J.* **2019**, *51*, 91–96.

Figures, tables, and texts are partially adapted with permission from K. Suwa, K. Oyaizu, H. Segawa, H. Nishide, *ChemSusChem* **2019**, *12*, 5207: Published by Wiley-VCH, Weinheim (2019).

# Chapter 4: Vapor-Phase Formation of Hole-Transporting Polymer Layers and their Applications for Evaporated Perovskite Solar Cells

## 4.1 Introduction

Fully evaporated perovskite solar cells with co-evaporated perovskite layers have been reported by some research groups.[1–6] The co-evaporated perovskite layers are formed with evaporating both methylamine hydroiodide (MAI) and $PbI_2$ simultaneously (Figure 4.1).[7–11] The evaporation conditions including evaporating ratio, rate, temperature, pressure, rotating speed, and annealing method should be severely controlled for forming high quality perovskite layers; therefore, these parameters and controlling recipe are individually determined on each evaporation chamber. However, after optimizing these parameters once, the evaporation process provide homogeneous and clean perovskite layers automatically. Vapor deposition methods also allow for easy upscaling of the cell area and residual-free layer formation due to unnecessity of any organic solvents in industrial technology.[12,13] From the above, the evaporation method is one effective technique for a practical use. Moreover, the co-evaporated perovskite layers can be formed on textured substrates homogeneously (Figure 4.1).[14–16] The homogeneous perovskite layer formed on the textured silicon substrates can be suggested as one promising candidate for a top cell of perovskite/silicon tandem solar cells. [17,18]

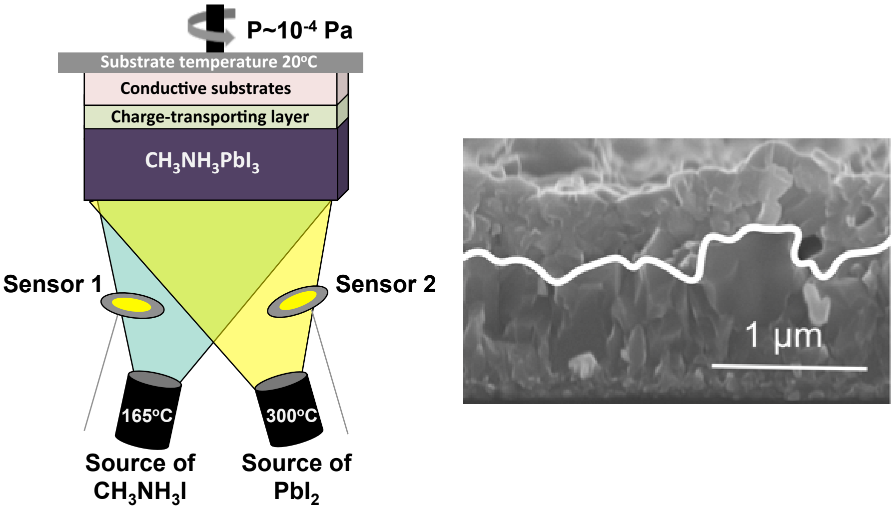

Figure 4.1 Left: Schematic image of forming the co-evaporated perovskite layer. Right: Cross-sectional SEM image of the co-evaporated perovskite layer on a rough FTO substrate.

One of remaining problems of the fully evaporated perovskite solar cells is hole-transporting material. Hole-transporting materials, which can be applied for fully evaporated perovskite solar cells, have been limited to evaporable low molecular weight organic compounds and inorganic materials.[19,20] For example, *N*4,*N*4,*N*4",*N*4"-tetra([1,1'-biphenyl]-4-yl)-[1,1':4',1"-terphenyl]-4,4"-diamine (TaTm) and *N,N*'-bis(naphthalene-1-yl)-*N,N*'-bis(phenyl)-benzidine (NPB) are examples of evaporable low molecular weight hole-transporting materials, which, however, need dopants of 2,2'-(perfluoronaphthalene-2,6-diylidene) dimalononitrile (F6-TCNNQ) or $MoO_3$, respectively, for sufficient hole mobility as hole-transporting materials of the perovskite solar cells (Figure 4.2).[21–25] However, controlling the deposition ratio of TaTm and F6-TCNNQ during co-evaporation processes is quite difficult, and low molecular weight hole-transporting materials show low durability owing to their high reactivity and the existence of the dopants.[26] Hole-transporting polymers, such as poly[bis(4-phenyl)(2,4,6-trimethylphenyl)amine] (PTAA), poly (3,4-ethylenedioxythiophene) doped with poly (4-styrenesulfonate) (PEDOT:PSS), poly(4-butylphenyldiphenylamine (polyTPD), and poly[*N*-9′-heptadecanyl-2,7-carbazole-alt-5,5-(4′,7′-di-2-thienyl-2′,1′,3′-benzothiadiazole)] (PCDTBT), have been used as hole-transporting materials with significant potentials as the high quality and cost-effective perovskite solar cells, even as top cells of perovskite/silicon tandem cells, due to the their high hole mobility and structural stability (Figure 4.2).[27–33] However, the hole-transporting polymers have not been applied by the vapor deposition because of their strong intermolecular interactions via van der Waals forces.

One strategy, for overcoming this problem, is the application of the vapor-phase polymerization method for directly preparing the hole-transporting polymers on the substrates, regardless of its roughness.[34,35] This method enables the application of π-conjugated hole-transporting polymers, which have higher mobility and durability than purchasable hole-transporting materials due to the unnecessity of alkyl side chains or flexible main chain structures for improving solubility in organic solvents, in the fully evaporated perovskite solar cells.[36–38] For in-situ vapor-phase polymerization, the pure polymer layers can directly be synthesized on the substrates by a sequential evaporation of both monomers and reaction initiators; for example, metal-free evaporable oxidants, iodine ($I_2$).

In this chapter, a representative, sublimable, and solid thiophene monomer of 2,2':5',2"-terthiophene (TTh) and the $I_2$ were sequentially deposited to give poly(terthiophene) (PTTh) layers on the substrates directly. The formed PTTh layer showed homogeneous film morphology, high hole mobility as dopant-free hole-transporting materials, and appropriate energy levels as the component of the perovskite solar cells. PTTh was applied as the hole-transporting layer of co-evaporated perovskite solar cells to yield reasonable photovoltaic conversion performance, and higher cell durability compared to cells with existing low molecular weight hole-transporting materials.

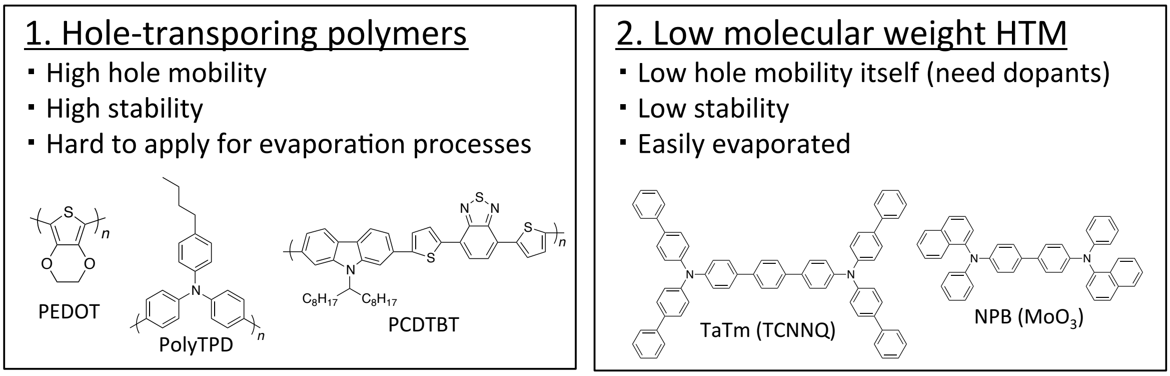

Figure 4.2 Comparison of hole-transporting polymers and low molecular weight hole-transporting materials.

## 4.2 Poly(terthiophene) Layer Formation via in-situ Vapor-Phase Polymerization

### 4.2.1 Monomer layer deposition (first step)

A thin layer of 2,2’:5’,2”-terthiophene (TTh) was formed on the cleaned substrates via two vapor deposition methods (Figure 4.3), named a bottle method and a chamber method. For the bottle method, the substrate was attached to the cover of a beaker and the TTh monomer was on the bottom of the beaker. The beaker was placed on a hotplate at various temperatures for 1 hour. The monomer film formation using a bottle method was facilely performed in atmospheric pressure but without real-time film thickness measurements, such as using a quartz crystal microbalance (QCM) sensor. In other words, this method could not be used to observe the growth of the layer. Therefore, TTh films with the bottle method was roughly controlled by adjusting only process temperature (in this chapter, 90, 110, 130, and 145 °C) for a fixed time of 1 hour.

On the other hand, the TTh deposition was performed in a vacuum chamber via thermal control at a low pressure of ~$10^{-6}$ mbar on the chamber method. The layer thicknesses were monitored by a calibrated QCM sensor.

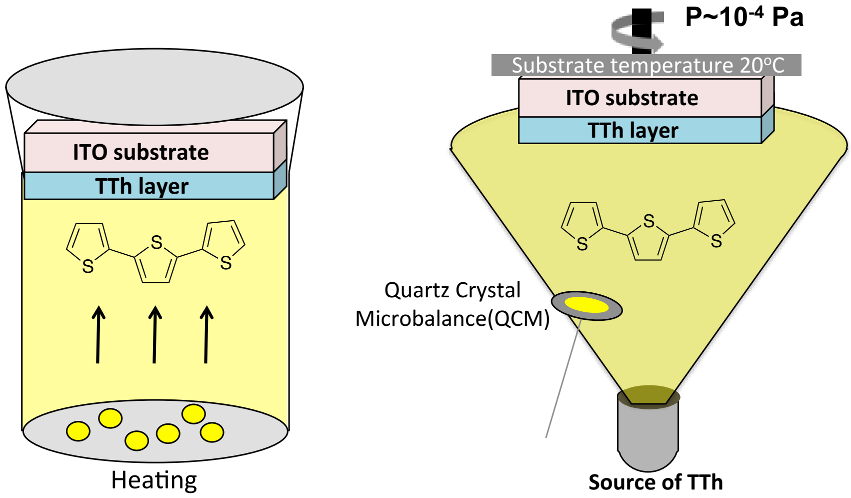

Figure 4.3 Scheme for TTh layer formation. Left: the bottle method and right: the chamber method.

### 4.2.2 In-situ vapor-phase polymerization (second step)

In the following steps, the substrates with the TTh layer fabricated by both methods (the bottle method and the chamber method) were transferred to another container with the evaporable oxidants: iodine ($I_2$). The substrates were attached to the cover of the container again and the container was sealed to avoid pollutions. The polymerization reaction was completed and a PTTh layer was obtained after 1 hour on a hotplate at 90 °C. After the process, the remained $I_2$ should be washed by methanol twice.

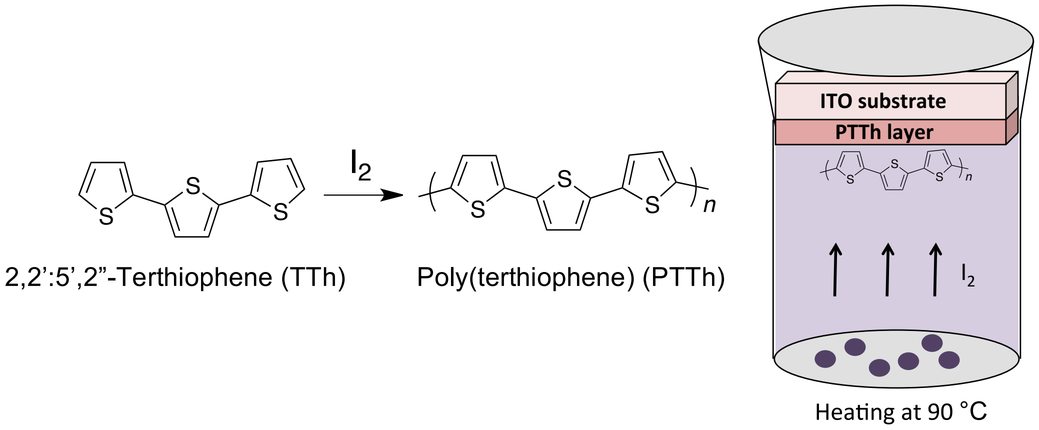

Figure 4.4 Schematic image of oxidative polymerization of TTh.

### 4.2.3 Characteristics of the vapor-phase polymerized poly(terthiophene)

The TTh layers fabricated by above two methods, the bottle method and the chamber method, and the vapor-phase oxidative polymerization, were observed by atomic force microscopy (AFM) (Figure 4.5). The TTh layers formed by the bottle method at low temperature of 90 and 110 °C on top of ITO substrates were relatively homogeneous with small roughness under 10 nm for 90 °C and 5 nm for 110 °C. At high temperature of 130 and 145 °C, the TTh films drastically changed to become more inhomogeneous with high roughnesses of over 20 nm and 100 nm, respectively, probably because the high deposition rate of TTh created the agglomeration of organic compounds. A careful determination of the appropriate temperature was necessity for the bottle method.

The chamber method realized aimed layer thickness of ca. 30 nm with less roughness (< 5 nm) comparing to the beaker method. The chamber method was not facile, needed high pressure, but easy to form thickness-controlled and homogeneous monomer layers; therefore, the chamber method was selected for forming all PTTh layer in this chapter.

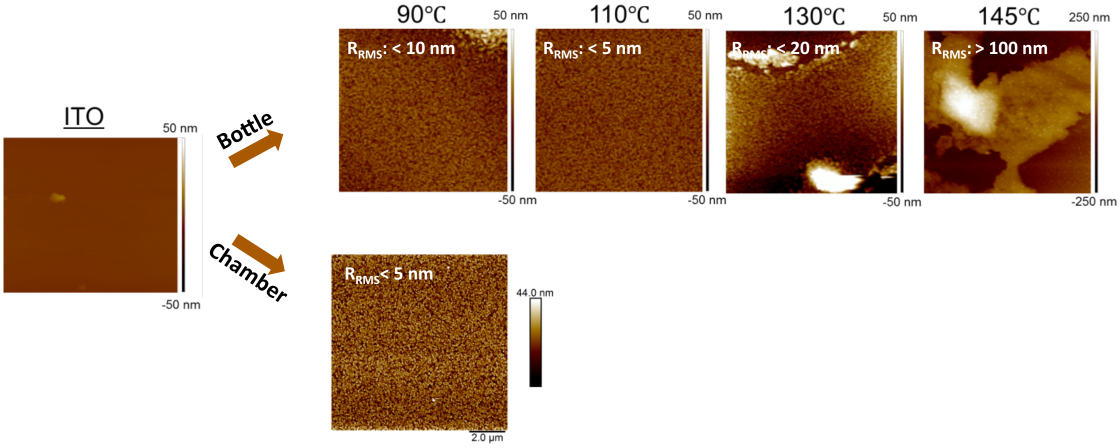

Figure 4.5 AFM images of TTh films formed via two types of evaporation methods.

The PTTh layers with high molecular weight were insoluble in all tested organic solvents of ethanol, acetone, chloroform, and DMF, due to their strong intermolecular interactions ascribed to their π-conjugated molecular structure and lack of alkyl side chains for enhancing their solubility. This less solubility realized the application of PTTh films as a hole-transporting material of inverted perovskite solar cells not only by dry processes but also solution processes for the perovskite formation. Anyway, the molecular weight of the PTTh could not be determined by a gel permeation chromatography as usual owing to the less solubility, therefore, was determined by matrix-assisted laser desorption ionization time-of-flight mass spectrometry

(MALDI-TOFMS) in the film state (Figure 4.6). The molecular weight of solid PTTh layer formed via the in-situ vapor-phase polymerization method proposed in this chapter was calculated to be ca. 2,700 (degree of polymerization of 10).

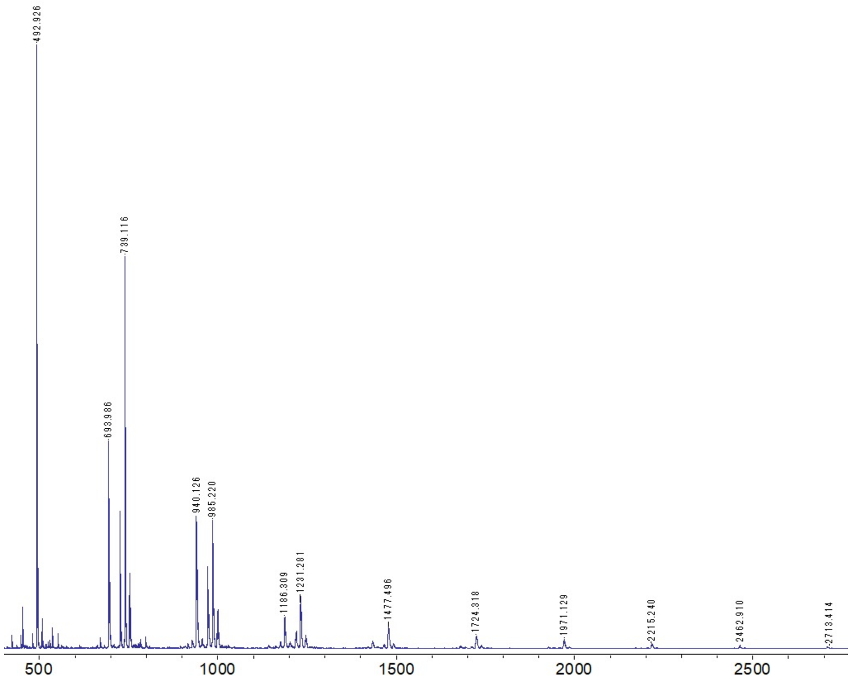

Figure 4.6 Molecular weight of the in-situ vapor-phase polymerized PTTh determined by a MALDI-TOFMS measurement.

The energy levels of the PTTh: the HOMO level estimated by photoelectron spectroscopy in air (PESA) method, the band gap energy measured by the absorption edge of the UV-Vis spectrum, and the LUMO level calculated by these two values, were -5.26, 1.94, and -3.32 eV, respectively (Table 4.1, Figure 4.7). The narrower band gap suggested an extension of the π-conjugated length due to satisfyingly polymerization. The appropriate HOMO and LUMO levels fit with the band alignment as an effective hole-transporting material of the perovskite solar cells.

**Table 4.1** Characteristics of TTh, PTTh, TaTm

| HTL | $E_{\mathrm{HOMO}}$ (-eV) | $E_{\mathrm{LUMO}}$ (-eV) | $E_{\mathrm{g}}$ (eV) | Absorption edge (nm) | $\mu$ (cm$^2$/Vs) |
|---|---|---|---|---|---|
| TTh | 5.48 | 2.57 | 2.91 | 426 | - |
| PTTh | 5.26 | 3.32 | 1.94 | 638 | $1.2 \times 10^{-3}$ |
| TaTm | 5.38 | 2.50 | 2.88 | 416 | $4.0 \times 10^{-3}$ |

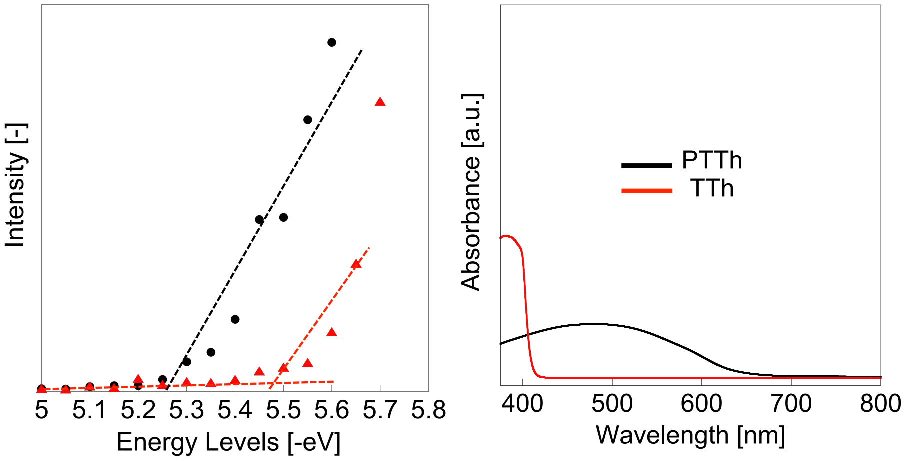

Figure 4.7 Left: Photo-electron spectroscopy in air (PESA) spectra of PTTh (black) and TTh (red). Right: UV-vis spectra of PTTh (black) and TTh (red)

The hole mobility of the PTTh thin layer estimated by a space-charge-limited current (SCLC) method was $1.2 \times 10^{-3}$ $cm^2$/Vs. The outstanding high value as undoped hole-transporting materials could be ascribed to the strong intermolecular π-π stacking and the unnecessity of insulating side chains for the solubility (Table 1, Figure 4.8). As comparison, the hole mobility of PTTh is quite close to the doped-TaTm and doped-spiro-OMeTAD generally used as hole-transporting materials of the fully evaporated perovskite solar cells and/or the solution processed perovskite solar cells. The in-situ vapor-phase polymerized PTTh could also exhibit significant advantages as a hole-transporting material in the evaporated perovskite solar cells.

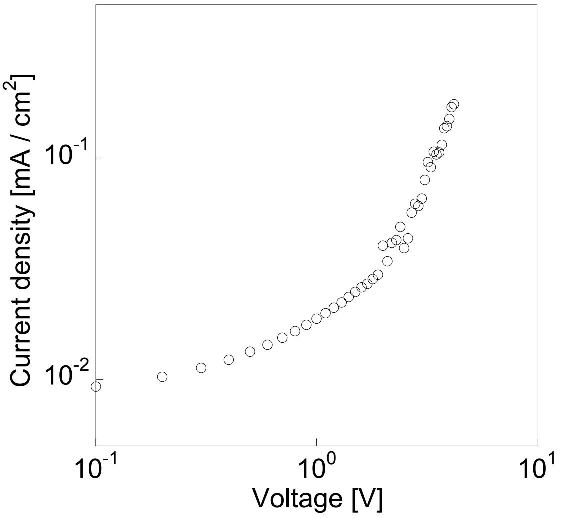

Figure 4.8 Space-charge-limited current result of PTTh using a hole-only device (FTO/PEDOT:PSS/PTTh/Au).

The PTTh and TaTm layers were prepared on bare glass substrates by evaporation processes with the thickness of about 20 nm, and their absorption and transmission were measured (Figure 4.9). The absorption of PTTh layer was lower than TaTm layer. This reduction might lead to an advantage in terms of light absorption, resulting in an increase of the short circuit current density ($J_{SC}$) of the solar cells. Moreover, good transmittance of PTTh from 400 nm to 1300 nm can also be a valuable advantage for tandem applications using silicon cells.

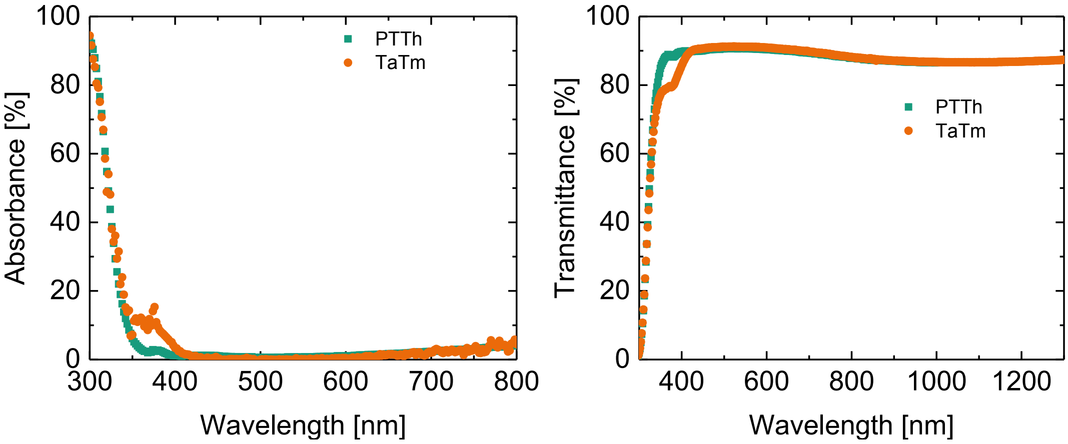

Figure 4.9 Absorbance and transmittance spectra of PTTh and TaTm films on glass substrates prepared by the chamber method.

## 4.3 Perovskite Solar Cells with in-situ Vapor-Phase Polymerized Thiophene Layers

The band diagram and the cross-sectional SEM image of an inverted (*p-i-n*) structure perovskite solar cell with in-situ vapor-phase polymerized PTTh are shown in Figure 4.10. The perovskite solar cells with the PTTh as a hole-transporting material and the co-evaporation $CH_3NH_3PbI_3$ perovskite layer showed a homogeneous layer formation with controlled film thickness. The layers composed of the *p-i-n* cells: 26 nm of PTTh, 303 nm of co-evaporated $CH_3NH_3PbI_3$, 77 nm of PCBM/AZO, and 95 nm of Au layer as a top electrode, were prepared on ITO substrates sequentially. Evaporated PTTh layer in the perovskite solar cells played a role of the hole-transporting layer and the spin-coated PCBM/AZO also played a role of the electron-transporting layers.

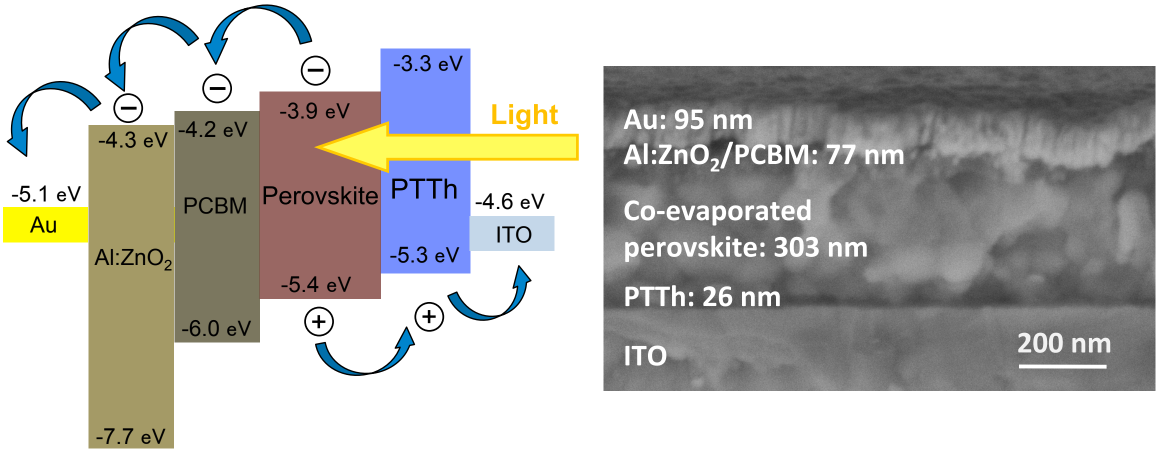

Figure 4.10 The energy level diagram and the cross-sectional SEM image of the perovskite solar cell with PTTh as hole-transporting materials.

The *J*-*V* curves of the perovskite solar cells with hole-transporting PTTh and TaTm are shown in Figure 4.11 and Table 4.2. The low fill factor (*FF*) of the cells fabricated with the both of them might be ascribed to a physical mismatch between each layer or small grains of the co-evaporated perovskite layer. The cells with the PTTh layer gave higher durability than the cells fabricated with a molecular weight hole-transporting material, TaTm, as a result of a fixed-voltage stability test (Figure 4.11). Although the cell fabricated with PTTh showed lower photovoltaic conversion efficiency, PTTh worked as a durable hole-transporting material probably because of its structural stability and dense layer formation owing to the strong interactions. Both cells also exhibited the small hysteresis (Figure 4.12). This high durability proposed the advantage of hole-transporting polymers for industrial fabrications of both the perovskite solar cells itself and the tandem cells with silicon solar cells. Morphological, optical, and electrical characterization of PTTh suggested that the hole-transporting polymers were successfully formed on the substrates using controllable and relatively easy evaporation process.

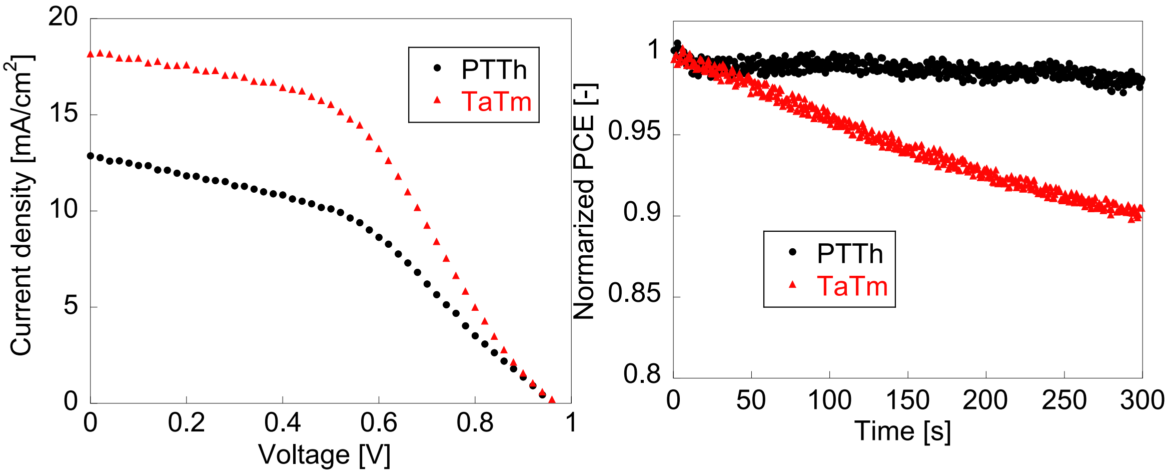

Figure 4.11 *J*-*V* curves and fixed-voltage stability results of the perovskite solar cells with the hole-transporting materials of PTTh and TaTm.

**Table 4.2** Photovoltaic characteristics of perovskite solar cells fabricated with evaporated HTMs

| HTM | $J_{SC}$ (mA/cm$^2$) | $V_{OC}$ (V) | *FF* (-) | $\eta$ (%) |
|---|---|---|---|---|
| PTTh | 13.7 | 0.96 | 0.45 | 5.9 |
| TaTm | 18.2 | 0.97 | 0.46 | 8.1 |

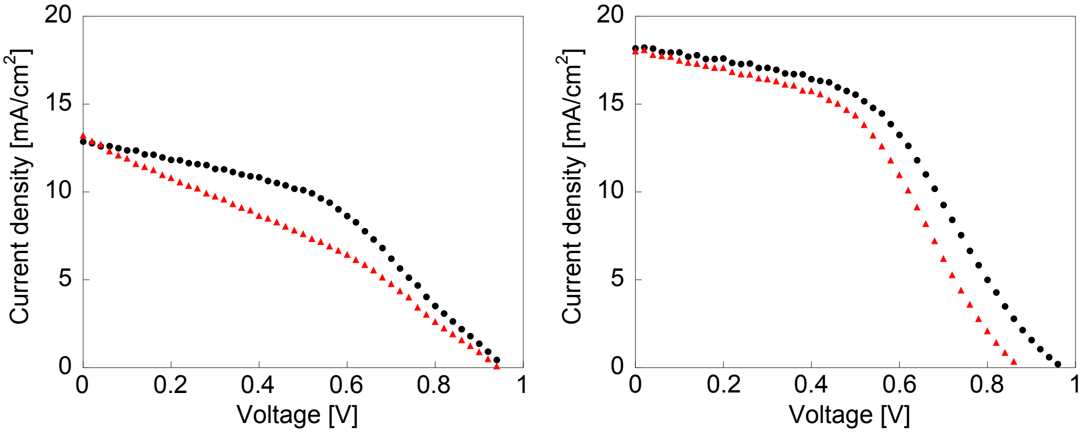

Figure 4.12 Hysteresis of the *J*-*V* curves of the cells fabricated with PTTh (left) and TaTm (right) (black dots: reverse scans and red triangles: forward scans).

## 4.4 Experimental Section

### 4.4.1 Polymer layer formation via an in-situ vapor-phase method

Indium doped tin oxide (ITO) substrates (AMG) were cleaned with detergent (2% aqueous solution of Hellmanex solution), water, isopropanol, and acetone, then dried at 150 °C on a hotplate for at least 1 hour. A thin layer of 2,2’:5’,2”-Terthiophene (TTh) (TCI) was formed on the cleaned ITO substrates via two different vapor deposition methods, named a bottle method and a chamber method. For the bottle method, the substrate was attached to the lid of a bottle. The bottom of the beaker was covered with TTh powder and the beaker was subsequently closed (and sealed by a parafilm) and placed on a hotplate for 1 hour. Sublimated TTh filled the bottle and attached to the surface of the ITO substrates. For the chamber method, the TTh deposition was performed in a Mini Spectros vacuum system (Kurt J. Lesker, U.K.) with a rate control at a negative pressure of ca. $10^{-6}$ mbar. The layer thicknesses were monitored by a calibrated QCM sensor.

In the following step, the TTh-coated substrates of both methods were transferred to a second bottle containing the oxidizing agent of iodine ($I_2$). The substrates were again attached to the lid of the bottle and the bottle was closed and sealed with parafilm for avoiding any vapor leakage. After 1 hour on a hotplate at 90 °C, the polymerization reaction was completed and a PTTh layer was obtained. The samples were subsequently washed in ethanol twice to remove excess iodine.

### 4.4.2 A fabrication of inverted perovskite solar cells

The PTTh layer formed by the vapor-phase polymerization method could only be applied for the *p-i-n* perovskite solar cells because the oxidant, in this case $I_2$, would decompose the most of the perovskite compounds in the *n-i-p* structure (the problem was the order of the layer formation). Photovoltaic cells with the *p-i-n* structure of ITO/PTTh/co-evaporated $CH_3NH_3PbI_3$/[6,6]-phenyl-$C_{61}$-butyric acid methyl ester (PCBM)/aluminum doped zinc oxide (AZO)/Au were prepared and the efficiency was measured. The PTTh layer on the ITO substrate were fabricated by sublimation method as shown in above section. A co-evaporation of $PbI_2$ and $CH_3NH_3I$ on top of the ITO/PTTh substrates was executed to form a homogeneous $CH_3NH_3PbI_3$ layer. A detail condition of the co-evaporation execution was written in chapter 4.4.4. After the evaporation step, the substrates with ITO/PTTh/$CH_3NH_3PbI_3$ were annealed at 100°C for 30 min under a nitrogen condition. For the electron-transporting layer, a solution of PCBM (Sigma Aldrich, 10 mg in 1 ml chloroform) was prepared and stirred for 2 hours and 70 μL of PCBM solution was drop-cast on the substrates while the substrates were spinning at 5000 rpm. An additional *n*-type conductive layer was prepared from a solution of AZO (Avantama N-21X, 2.5 wt% in mixture of alcohols) and also drop-cast on the substrates during spinning at 4000 rpm. Finally, 80 nm Au electrode was deposited by an evaporation chamber.

### 4.4.3 Characterization methods

The surfaces of TTh were observed by an atomic force microscope (Bruker Dimension Edge AFM). A scanning electron microscope (Zeiss Auriga) was also used to show the cross-sectional images of the cells, and each film thickness was measured by the SEM images. The HOMO levels of hole-transporting materials were measured by PESA method using a photoelectron spectrometer (AC-3E, Riken Keiki). The UV-Vis spectra were performed with a spectrophotometer (V-670, JASCO) to determine their optical band gaps. The LUMO levels of the materials could be calculated via each HOMO level and band gap. A molecular weight of the insoluble polymer directly formed on substrates was measured by MALDI-TOFMS using 2,5-dihydroxybenzoic acid as a matrix (autoflex, Bruker). Hole mobility of the PTTh was estimated by a space-charge-limited current (SCLC) method using a hole-only device (FTO/PEDOT:PSS/PTTh/Au), which was fabricated by spin-coating of PEDOT:PSS (Heraeus) solution at 1500 rpm for 30 s on a washed FTO substrate by an UV-ozone treatment (Atock Co.; sheet resistance of 30 Ω/sq), PTTh using the in-situ vapor-phase polymerization methods, and 80 nm Au deposited at 0.05 nm/s by the evaporation chamber. The *J*-*V* measurements under 1 SUN and SCLC measurements were executed with a solar cell evaluation system with an active area of 0.25 $cm^2$ defined by a black shadow mask. The intensity of sunlight was set using a Si reference solar cell. The voltage was varied for the reverse and forward scans from 1.2 to −0.1 V and −0.1 to 1.2 V, respectively, with a scan rate of 43 mV/s.

### 4.4.4 Operation method of an evaporation system for forming perovskite layers

1. A cooling system (chiller) and an evaporation pump for a reflux were turned on at first. (Both are under the glove box.)
2. Nitrogen gas was introduced from $N_2$ pipe for opening the chamber. (The pressure should be equal as outside. Turning on LV2: N2)
3. The chamber was opened from outside and enough materials were placed in evenly. (When you open the chamber from outside, a gas mask and a white robe should be put on for your safety.)
4. When the co-evaporation, the film thickness sensors should be covered by cylindrical aluminum foil for preventing the interference each other.
5. The chamber was evacuated roughly until -100.0. (Turning on RP and RV.)
6. Gas was introduced from glove box. (The pressure should be equal as the inside of the glove box. Turning off RV and turning on LV1: GB)
7. The substrates with under layers were introduced into the evaporation chamber through a glove box by using Kapton tapes or evaporation masks.
8. The chamber was evacuated roughly again. (Turning on RV.)
9. Turbo molecular pump (TMP) was turned on and wait for the standby. (Turing off RV, and turning on FV and TMP)
10. The chamber was evacuated by rough pump satisfyingly as monitoring the pressure. (Turing off FV, and turning on RV and VG)
11. After turning on SP1, the chamber was evacuated by TMP. (Turing off RV, and turning on FV and MV)
12. After turning on SP2, the evaporation could be done. (Refer to the “Deposition setting” and “Deposition execution” sections)
13. After evaporation, the plates or the crucibles were cooled for enough time. (Turning off MV, FV, and TMP)
14. The chamber was washed by dry Nitrogen gas (introducing $N_2$ gas and evacuating roughly) once or twice for your safety.
15. The substrates were removed through the inside of the glove box. Finally, the chamber was evacuated roughly at ca. -100.0, and RV and RP were turned off.
16. After turning off TMP completely (after braking), the cooling machine and the pump for cooling water were turned off.

**Deposition settings**

Waseda evaporation machine possesses two plates (Inorganic 1 and 2) and three crucibles (Organic 1, 2 and 3). Inorganic 1 is on the front left and inorganic 2 is on the front right. Organic 1 (left) and 2 (right) are on the back left, and organic 3 is on the back right. Inorganic 1 and organic 3 are controlled by SS1 (heater). Each sensor numbers is inorganic 1: SS1-(1) and organic 3: SS1-(2). Inorganic 2, organic 1, and 2 are controlled by SS2. Each sensor numbers is inorganic 2: SS2-(1) and organic 1 and 2: SS2-(2). SS1 and SS2 can be set at different temperature control (Figure 4.13).

Density and tooling factors of the evaporated materials should be determined before an evaporation execution. The decision of the tooling factor is one of the most important parts of evaporation settings. Tooling factor means a correction coefficient between a monitored film thickness and a real film thickness. Two main factors, distance from evaporation sources and absorption efficiency of the substrate surface, strongly affects the tooling factor. Tooling factor is determined via dividing a real value estimated by cross-sectional SEM image or thickness meter, for example, provided by KLA-TENCOR Co., by a monitored value. Density is not quite important after determining tooling factor, because tooling factor can involve density tolerance. Tooling factors will be changed when the material or shape of substrates are changed even only setting of cylindrical aluminum foil. Tooling factors are generally related to the distance between materials and substrates, therefore, it might be ca. 0.50 in our system.

After determining the tooling factor, “deposition programs” should be decided. First of all, “MENU”, “2”, and “2” were pushed to display “deposition program menu”. “Deposition program No.” was entered to move another program after pushing “EDIT”. (128 kinds of programs can be saved in our system. Comments can be written in each program for identification.)

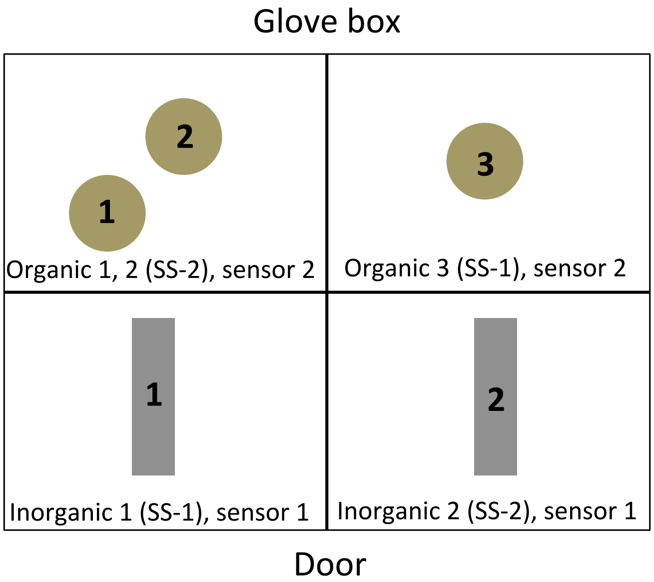

Figure 4.13 Setting of the evaporation chamber in Waseda lab.

### a. Deposition programs

First function and event should be “ready” and “PORT01H” or “PORT05H” for turning on the heater. Heater number should be set as 01 on the sources of “inorganic 1” and “organic 3”, and as 05 on “inorganic 2” and “organic 1 and 2”.

PWR RAMP: Power will linearly go up until set power in a set time.
PWR CNST: Set power will be kept for a set time.
RATE RAMP: Rate will linearly go up until a set rate in a set time. However, “the set rate” is an unknown factor, therefore, it does often not work well.
RATE CNST: Set rate will be kept until a set layer thickness.

PWR RAMP and PWR CNST should be basically used to pre-heat the materials slowly at the temperature slightly lower than the deposition temperature. The deposition rate can be controlled by only RATE CNST. The shutter should be released when hunting is settled.

### b. Deposition parameters

DENSITY: Density of evaporated materials should be entered.

Z-RATIO: Deposited materials show their own resonant frequency on QCM, which was used for determining the film thickness. Therefore, resonant impedance of each material on QCM should be set when you need strict film thickness.

TOOLING 1, 2: Tooling factor should be set. (1 and 2 are same values.)

“FEED BACK”, “GAIN”, “TIME-C”, “LIMIT”, “DIFFERENTATION” should be determined after reading the “Evaporation control” section.

MAX POWER: When you use PID control, exceeding this value forcibly cut all systems.

MIN POWER: You must set this value “0” as usual.

SENSOR SHUTTER OPEN: You can open of the shatter by time controlling.

SENSOR SHUTTER CLOSE: You can close of the shatter by time controlling.

FULL SCALE THK: Order of film thickness can be set. 0.0 should be entered for autoscale.

FULL SCALE RATE: Order of deposition rate can be set. In our case, 0.1 nm/s is sufficient.

FILTER TC: Time constant ($\tau$) of sampling time of the material deposition. 1 s is sufficient.

SENSOR NO.: Sensor No. should be set as inorganic = 1 and organic = 2.

XTAL CHANGE FREQ: You can set the lifetime of sensor. 4.00 MHz is my recommendation.

HEARTH NO.: Heater number should be set as 1 on the sources of “inorganic 1” and “organic 3”, and as 5 on “inorganic 2” and “organic 1 and 2”.

THK CHANGE LIMIT: You can set some value when you want to evaporate materials, which are easily peeled. As usual, 0.0 should be set.

### c. Deposition equipment

#### ・Quartz crystal microbalance (QCM)

Quartz crystal microbalance (QCM) is a kind of thickness meter using quartz crystal unit. A weight change of the crystal unit, which shows fixed resonance frequency in fixed AC electric field, decreases its resonance frequency and the difference between a former and a later resonance frequency gives the weight of deposited materials. The film thickness can be easily calculated by the estimated weight and the area of QCM. The first resonance frequency of QCM is generally 5.00 MHz and is gradually decreasing. When the resonance frequency becomes under 4.50 MHz, the QCM should be changed for accurate measurements. (If exact thickness is needed, 4.80 MHz may be enough to change.)

- **Evaporation boat**

Thermostable materials, such as tungsten, are used as a material holder. In our system, evaporation boats are used for inorganic source 1 and 2. Evaporation boat has an advantage of detailed temperature controlling by its better controllability due to the small heat capacity. However, this method also has a disadvantage of affecting bad influence for QCM and another boats because evaporation materials are fully exposed. Therefore, cylindrical aluminum foil should be used for covering QCM. High temperature may also stretch the boat to break it during the processing (if this problem becomes serious, Cosmo Science Co. can solve it by exchanging a stopper of boats).

- **Crucible**

Ceramic crucibles are used as a material holder of organic source 1, 2, and 3 in our systems. The crucible can contain a huge amount of materials, but the heat capacity is too large to control temperature by PID control. When you use the crucibles, long time pre-heating and severe temperature controlling are needed. These problems can be improved by changing the internal structure of heater or crucible itself. On the other hand, the crucible has advantages of a little influence on each materials and a little risk of breaking it.

**d. Process program**

After setting “depo program”, the program should be set in process program menu (press 2 → 3) by pressing the program number. Inorganic 1 and organic 3 should be set in SS-1, and inorganic 2 and organic 1 and 2 should be set in SS-2.

**Deposition execution**

Substrates were moved to “evaporated location” from “prepared location” and were rotated as slow as possible. The evaporation was automatically started by turning on the evaporation power source buttons, for example metal source 1, and pushing an “evaporation” button. The shutters of the organic sources should be opened at first. The inorganic sources do not have a shutter. (Automatical setting: the substrate shutters can be opened when the Rate CNST. Manual setting: you can open the shutter whenever you want.) The evaporation processes can be stopped by pushing an "evaporation" button again. After the evaporation process, the rotation of the substrate can also be stopped and moved to "prepared location". The substrates can be removed after several decade minutes for cooling.

**Evaporation control (Advanced)**

Our evaporation system is controlled by PI or PID controls. The PID control, a kind of feed back control, is divided for P control, I control, and D control. The basis of the feed back control is governed by below equation, which means that a present power can be determined by a difference between a set point of deposition rate and the present deposition rate.

$$e(t) = r(t) - y(t)$$

*r*(t): a set point of deposition rate, *y*(t): a present deposition rate, and *e*(t): a present power

**P control**

The P control means "proportional control". The operation amount is controlled as a linear function by the *e*(t) and P gain.

$$u(t) = Kp \cdot e(t)$$

*u*(t): operation amount and *K*p: P gain (a proportionality constant)

The above equation means when the difference between a set point of deposition rate and the present deposition rate is large, the operation amount is increased. Too large *K*p leads overshoot and hunting control (impossible to evaporate). Too small *K*p takes long time to arrive the set point and makes error.

**PD control**

The D control means "differential control". The differential term works as a brake against sudden changes of a *K*p・*e*(t) term.

$$u(t) = Kp \cdot e(t) - Kd\frac{de(t)}{dt}$$

*K*d: D gain (a proportionality constant)

D control can suppress the overshoots and hunting control, therefore, *K*p can be increased to make process time short and error small.

## PI control

The I control means "Integral control". The integral term works as supplementation of the error between the set point and the present power.

$$u(t) = Kp \cdot e(t) + Ki \int_0^T e(t)\, dt$$

*K*i: I gain (a proportionality constant)

I control can suppress the error of the set point (offset). The large *K*i takes long time to settle and gives a huge effect for present power to present overshoots.

## PID control

The PID control is the combination of the P, I, and D controls. The appropriate proportionality constants can control the deposition rate well. In our systems, *K*p, *K*d, and *K*i can be set as below.

$$u(t) = Kp \cdot e(t) + Ki \int_0^T e(t)\, dt - Kd \frac{de(t)}{dt}$$

FEED BACK: PI or PID controls can be selected.
GAIN: *K*p (0.1-2)
TIME-C: 1/*K*i (5-10)
LIMIT: Limit of terms of $Ki \int_0^T e(t)\, dt$ for restricting the change of the value.
DIFFERENTATION: *K*d (1-10)

## References

[1] G. Longo, C. Momblona, M.-G. La-Placa, L. Gil-Escrig, M. Sessolo, H. J. Bolink, *ACS Energy Lett.* **2018**, *3*, 214–219.
[2] W. Ke, D. Zhao, C. R. Grice, A. J. Cimaroli, G. Fang, Y. Yan, *J. Mater. Chem. A Mater. Energy Sustain.* **2015**, *3*, 23888–23894.
[3] R. Kottokkaran, H. A. Gaonkar, H. A. Abbas, M. Noack, V. Dalal, *J. Mater. Chem. A Mater. Electron.* **2019**, *30*, 5487–5494.
[4] J. Ávila, C. Momblona, P. P. Boix, M. Sessolo, H. J. Bolink, *Joule* **2017**, *1*, 431–442.
[5] L. Calió, C. Momblona, L. Gil-escrig, S. Kazim, M. Sessolo, *Sol. Energy Mater.*

*Sol. Cells* **2017**, *163*, 237–241.

[6] F. Sahli, J. Werner, B. A. Kamino, M. Bräuninger, R. Monnard, B. Paviet-salomon, L. Barraud, L. Ding, J. J. D. Leon, D. Sacchetto, et al., *Nat. Mater.* **2018**, *17*, 820–826.

[7] R. Kottokkaran, H. A. Gaonkar, H. A. Abbas, M. Noack, V. Dalal, *J. Mater. Sci. Mater. Electron.* **2019**, *30*, 5487–5494.

[8] L. Cojocaru, K. Wienands, T. W. Kim, S. Uchida, A. J. Bett, S. Rafizadeh, J. C. Goldschmidt, S. W. Glunz, *ACS Appl. Mater. Interfaces* **2018**, *10*, 26293–26302.

[9] L. Cojocaru, K. Wienands, U. Erdil, P. S. C. Schulze, L. E. Mundt, A. J. Bett, M. Breitwieser, F. Lombeck, M. Prescher, L. Kirste, S. Vierrath, J. C. Goldschmidt, S. W. Glunz, *IEEE J. Photovoltaic* **2019**, *10*, 276-286.

[10] D. Pérez-Del-Rey, P. P. Boix, M. Sessolo, A. Hadipour, H. J. Bolink, *J. Phys. Chem. Lett.* **2018**, *9*, 1041–1046.

[11] M. Liu, M. B. Johnston, H. J. Snaith, *Nature* **2013**, *501*, 395–398.

[12] L. K. Ono, M. R. Leyden, S. Wang, Y. Qi, *J. Mater. Chem. A* **2016**, *4*, 6693–6713.

[13] P. Shen, Y. Chiang, M. Li, T. Guo, P. Chen, P. Shen, Y. Chiang, M. Li, T. Guo, *APL Mater.* **2016**, *4*, 091509.

[14] N. Tucher, J. Eisenlohr, P. Kiefel, O. Höhn, H. Hauser, M. Peters, C. Müller, J. C. Goldschmidt, B. Bläsi, *Opt. Express* **2015**, *23*, 302–307.

[15] B. W. Schneider, N. N. Lal, S. Baker-finch, T. P. White, *Opt. Express* **2014**, *22*, 1422–1430.

[16] M. Filipi, P. Löper, B. Niesen, S. De Wolf, J. Kr, C. Ballif, M. Topi, *Opt. Express* **2015**, *23*, 480–484.

[17] J. Wemer, F. Sahli, F. Fu, J. J. D. Leon, A. Walter, B. A. Kamino, B. Niesen, S. Nicolay, Q. Jeangros, C. Ballif, *ACS Energy Lett.* **2018**, *3*, 2052–2058.

[18] G. Nogay, F. Sahli, J. Werner, R. Monnard, M. Boccard, M. Despeisse, F. Haug, Q. Jeangros, A. Ingenito, C. Ballif, et al., *ACS Energy Lett.* **2019**, 844–845.

[19] N. Shibayama, H. Kanda, T. W. Kim, H. Segawa, S. Ito, *APL Mater.* **2019**, *7*, 031117.

[20] T. Abzieher, S. Moghadamzadeh, F. Schackmar, H. Eggers, F. Sutterlüti, A. Farooq, D. Kojda, K. Habicht, R. Schmager, A. Mertens, et al., *Adv. Energy Mater.* **2019**, *1802995*.

[21] C. Momblona, L. Gil-Escrig, E. Bandiello, E. M. Hutter, M. Sessolo, K. Lederer, J. Blochwitz-Nimoth, H. J. Bolink, *Energy Environ. Sci.* **2016**, *9*, 3456–3463.

[22] J. Werner, B. Niesen, C. Ballif, *Adv. Mater. Interfaces* **2018**, *5*, 1700731.

[23] C. Momblona, L. Gil-Escrig, E. Bandiello, E. M. Hutter, M. Sessolo, K. Lederer, J. Blochwitz-Nimoth, H. J. Bolink, *Energy Environ. Sci.* **2016**, *9*, 3456–3463.

[24] K. P. S. Zanoni, C. Dreessen, M. Sessolo, D. Pe, P. P. Boix, H. J. Bolink, *Chem. Mater.* **2019**, *31*, 6945–6949.

[25] W. Gao, A. Kahn, *J. Appl. Phys.* **2003**, *94*, 359–366.

[26] B. Danekamp, N. Droseros, D. Tsokkou, V. Brehm, P. P. Boix, M. Sessolo, H. J. Bolink, *J. Mater. Chem. C* **2019**, 523–527.

[27] J. H. Heo, H. J. Han, D. Kim, T. K. Ahn, S. H. Im, *Energy Environ. Sci.* **2015**, *8*, 1602–1608.

[28] Q. Wang, C. Bi, J. Huang, *Nano Energy* **2015**, *15*, 275–280.

[29] A. Isakova, P. D. Topham, *J. Polym. Sci. Part B Polym. Phys.* **2017**, *55*, 549–568.
[30] L. Zhao, X. Wang, X. Li, W. Zhang, X. Liu, Y. Zhu, H. Q. Wang, J. Fang, *Sol. Energy Mater. Sol. Cells* **2016**, *157*, 79–84.
[31] W. L. Tsai, W. H. Lee, C. Y. Chen, S. Y. Hsiao, Y. J. Shiau, B. W. Hsu, Y. C. Lee, H. W. Lin, *Nano Energy* **2017**, *41*, 681–686.
[32] L. Mazzarella, Y. H. Lin, S. Kirner, A. B. Morales-Vilches, L. Korte, S. Albrecht, E. Crossland, B. Stannowski, C. Case, H. J. Snaith, et al., *Adv. Energy Mater.* **2019**, *1803241*.
[33] L. Dou, J. Gao, E. Richard, J. You, C. C. Chen, K. C. Cha, Y. He, G. Li, Y. Yang, *J. Am. Chem. Soc.* **2012**, *134*, 10071–10079.
[34] K. Oka, O. Tsujimura, T. Suga, H. Nishide, B. Winther-Jensen, *Energy Environ. Sci.* **2018**, *11*, 1335.
[35] K. Oka, K. Noguchi, T. Suga, H. Nishide, B. Winther-jensen, *Adv. Energy Meter.* **2018**, *1803286*, 1–7.
[36] W. J. Jo, J. T. Nelson, S. Chang, V. Bulović, S. Gradečak, M. S. Strano, K. K. Gleason, *Adv. Mater.* **2016**, 6399–6404.
[37] B. Winther-jensen, J. Chen, K. West, G. Wallace, *Macromolecules* **2004**, *37*, 5930–5935.
[38] J. Mei, Z. Bao, *Chem. Mater.* **2014**, *26*, 604–615.

Figures, tables, and texts are partially adapted with permission from K. Suwa, L. Cojocaru, K. Wienands, C. Hofmann, P. S. C. Schulze, A. J. Bett, K. Winkler, J. C. Goldschmidt, S. W. Glunz, H. Nishide, *ACS Appl. Mater. Interfaces* **2020**, DOI: 10.1021/acsami.9b20981: Published by ACS Publications, Washington (2020).

# Chapter 5: Tandem Solar Cells with a Vapor-Phase Formed Hole-Transporting Polymer

## 5.1 Introduction

Tandem solar cells using two or more different kinds of solar cells with different light-absorbing wavelengths are effective methods for enhancing the entire photovoltaic conversion efficiency and reducing the cost of the solar cells.[1–3] The perovskite solar cells are reasonable candidates as a component of tandem solar cells owing to their adjustable band gap (1.5-1.8 eV) and great film formability.[4,5]

Two terminal (2T) cells have been proposed as fundamental tandem solar cells with simple fabrication processes (Figure 5.1).[6,7] $V_{OC}$ of the 2T cells is calculated by a sum of each light-absorbing layer, but $J_{SC}$ of the cells is determined by a lot of factors including bulk resistances and junction resistances of all materials and interfaces.[8,9] Therefore, the strict control of the homogeneous film formation, the band alignment, and the physical matching between the interlayers have been needed for obtaining highly efficient 2T cells. Especially, negative effects for other layers by, for example, solvents for wet processes must be prevented during film formation.

From the above viewpoint, the evaporation is a suitable method because it can deposit clean and homogeneous layers independent of the substrate´s roughness or texturing.[10] The evaporation method can realize highly efficient both perovskite/perovskite and perovskite/silicon tandem solar cells.

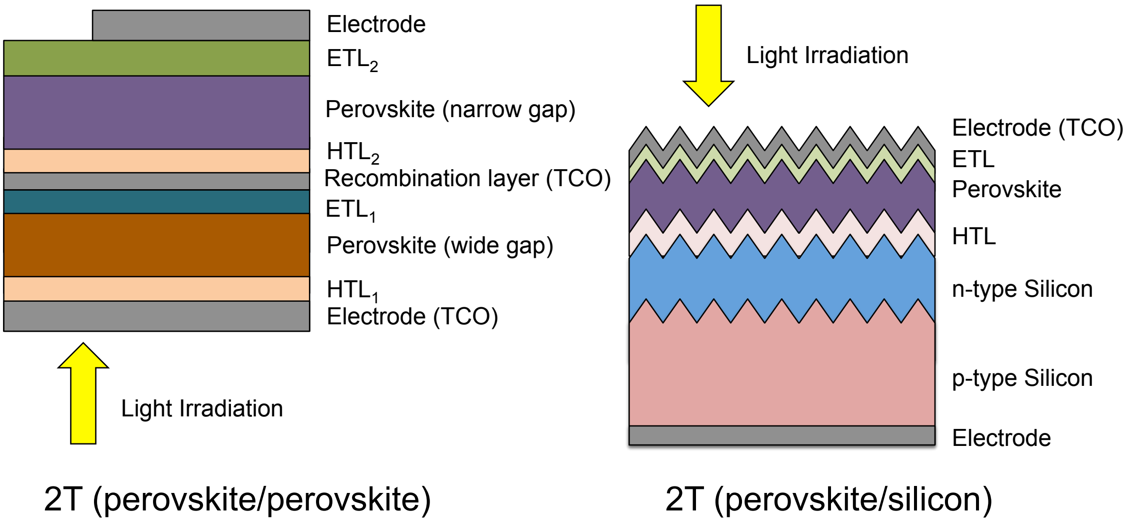

Figure 5.1 Structures of 2T tandem solar cells.

For enhancing the photovoltaic conversion efficiency of not only the silicon solar cells themselves but also the tandem solar cells, a front side texturing with micrometer scale pyramidal structures has been applied to suppress surface light reflection and redirect light into the silicon cells to enhance the photocurrent (Figure 5.2).[11–13] One report proposed that the theoretical maximum efficiency of the perovskite/silicon tandem cells could be enhanced from 28.3 % to 31.0 % with the textured surface structures.[14] However, a limitation of applicable materials on textured under layers has been one of the essential problematic issues. In-situ vapor-phase polymerized hole-transporting material described in Chapter 4 could be one potential candidate for a hole-transporting layer.

In this chapter, elemental technologies were developed for the fabrication of perovskite-modified tandem cells. Several types of perovskite layers were formed by the co-evaporation process to apply as light-absorbing layer of the solar cells. The in-situ vapor-phase polymerized PTTh thin layer was applied on the textured silicon substrate, and its applicability was calculated by optical properties of textured optical sheets (OPTOS) simulation method.[15,16]

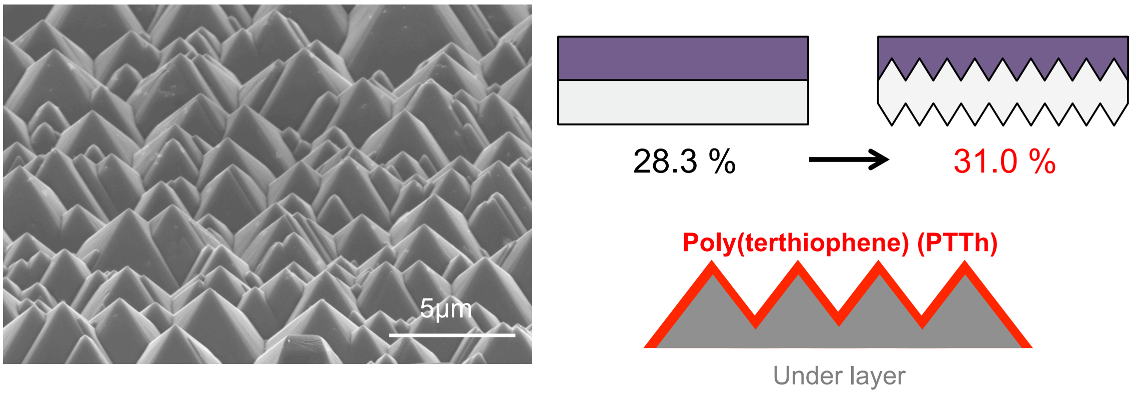

Figure 5.2 SEM image of a textured silicon substrate, schematic images of the enhanced performance, and the PTTh application.

## 5.2 Multiple Perovskite Layers Formation via Co-Evaporation Methods for Perovskite/Perovskite Tandem Solar Cells

### 5.2.1 Co-evaporated methylammonium lead iodide perovskite solar cells

Multiple types of perovskite layers with different optical properties, such as band gaps ($E_g$), conduction band minimum ($E_c$), and valence band maximum ($E_v$), have been demanded for fabricating perovskite/perovskite tandem solar cells. Reasonable fabrication processes for multi-layer stacking without negative effects for other layers are also important for highly efficient and durable tandem cells because tandem cells require more layers than single cells. From the above viewpoint, the evaporation methods are appropriate for the tandem cell fabrication.

A photovoltaic conversion layer using a representative perovskite compound, methylammonium lead iodide ($MAPbI_3$) with $E_g$ = 1.5 eV, $E_c$ = -3.9 eV, and $E_v$ = -5.4 eV,[17,18] was formed by the co-evaporation method described in Chapter 4. A ratio of methylamine hydroiodide (MAI) and lead iodide ($PbI_2$) was optimized for forming better $MAPbI_3$ layer. The condition of MAI:$PbI_2$ = 4:1 (an evaporation rate) gave homogeneous $MAPbI_3$ layer without remaining $PbI_2$ (Figure 5.3).

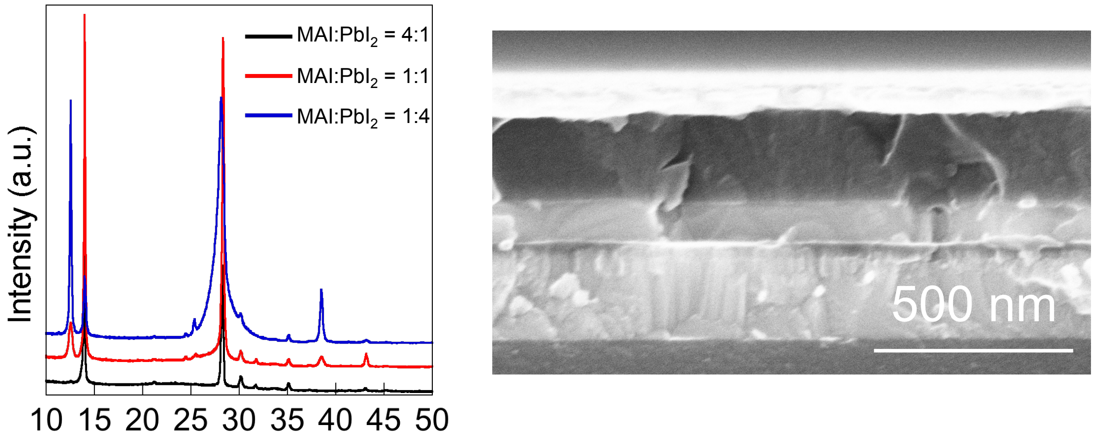

Figure 5.3 Left: XRD patterns of the $MAPbI_3$ layer formed by the co-evaporation method. Right: Cross-sectional SEM image of the $MAPbI_3$ perovskite solar cells fabricated by the co-evaporation method.

Planar-type perovskite solar cells were fabricated with planar conductive substrates of Indium-doped tin oxide (ITO)/antimony-doped tin oxide (ATO), planar electron transporting layers of compact-$TiO_2$ (*c*-$TiO_2$) and [6,6]-Phenyl-$C_{61}$-butyric acid methyl ester (PCBM), the co-evaporated light-absorbing layers, and hole-transporting materials because the evaporated perovskite layer has an advantage of the planarity. The cell fabricated with the co-evaporated $MAPbI_3$ layer formed by the ratio of MAI:$PbI_2$ = 4:1 and 2,2,7,7-tetrakis(*N*,*N*-di-*p*-methoxyphenylamine)-9,9-spirobifluorene (spiro-OMeTAD) as the hole-transporting layer showed the top photovoltaic conversion efficiency of 9.3 %, which was almost same as the efficiency of 10.1 % given by the cell fabricated with the solution-processed (anti-solvent method) $MAPbI_3$ layer

(Figure 5.4, Table 5.1). The perovskite layer fabricated by the "hybrid method", in which $PbI_2$ and MAI were sequentially deposited, has not achieved high efficiency in this study. The incident photon to current efficiency (IPCE) results of them also exhibited similar light absorption in the range of visible-light.

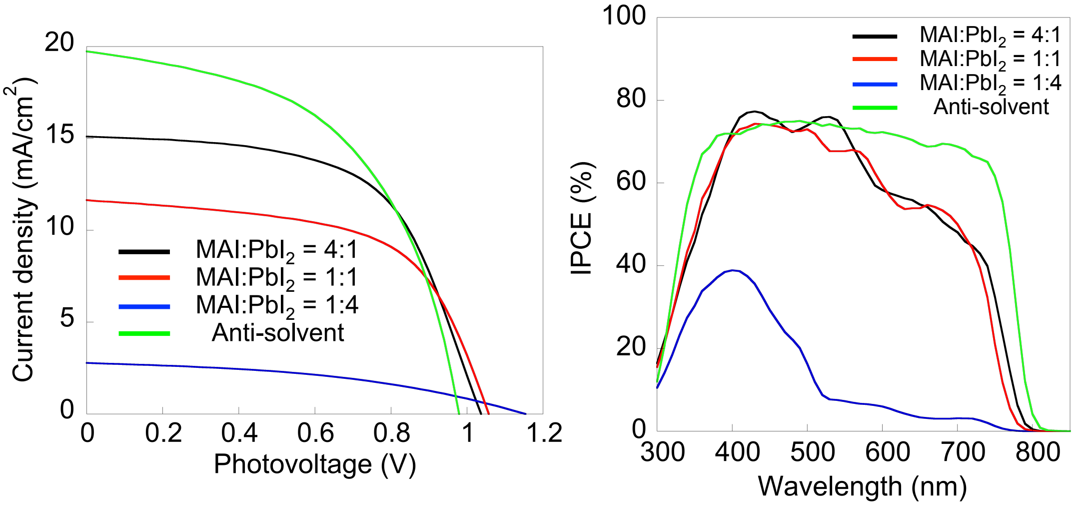

Figure 5.4 *J-V* curves and IPCE spectra of the perovskite solar cells fabricated with co-evaporation methods

**Table 5.1** Photovoltaic characteristics of perovskite solar cells fabricated with co-evaporation methods

| | MAI:$PbI_2$ | $J_{SC}$ (mA/cm$^2$) | $V_{OC}$ (V) | *FF* (-) | $\eta$ (%) |
|---|---|---|---|---|---|
| Co-evaporation | 4:1 | 15.1 | 1.04 | 0.59 | 9.3 |
| | 1:1 | 11.6 | 1.06 | 0.59 | 7.3 |
| | 1:4 | 2.8 | 1.15 | 0.42 | 1.3 |
| Anti-solvent | | 19.7 | 0.98 | 0.52 | 10.1 |
| Hybrid | | 14.9 | 0.97 | 0.36 | 5.2 |

The cell of ITO/ATO/*c*-$TiO_2$/PCBM/co-evaporated perovskite layer/hole-transporting materials/Au was totally planar; therefore, hole-transporting polymers, such as poly[bis(4-phenyl)(2,4,6-trimethylphenyl)amine] (PTAA), could be used effectively due to their thin film formability. The cells fabricated with PTAA showed higher photovoltaic efficiency of 9.0 % (maximum) and 8.8 % (average) than the cells with spiro-OMeTAD of 8.4 % (maximum) and 7.3% (average) in the same batch (Figure 5.5 and Table 5.2). The cells were also formed on large substrate (inset of Figure 5.3)

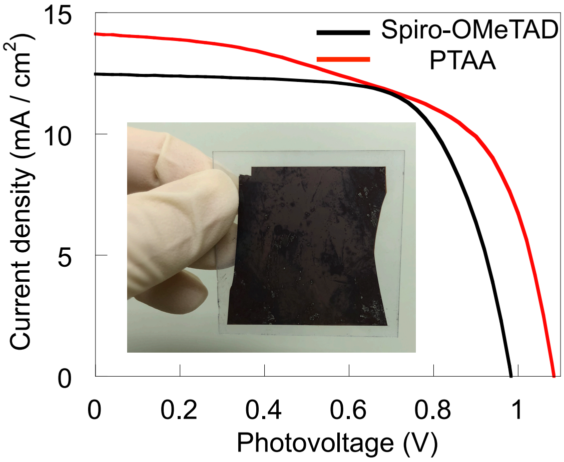

Figure 5.5 *J-V* curves of the perovskite solar cells fabricated with co-evaporated perovskite layer and spiro-OMeTAD or PTAA. Inset: the co-evaporated perovskite layer formed on a 10×10 cm$^2$ substrate.

**Table 5.2** Photovoltaic characteristics of perovskite solar cells fabricated with co-evaporated $MAPbI_3$ and various HTMs

| HTM | $J_{SC}$ (mA/cm$^2$) | $V_{OC}$ (V) | *FF* (-) | $\eta_{Max.}$ (%) | $\eta_{Ave.}$ (%) |
|---|---|---|---|---|---|
| PTAA | 14.1 | 1.08 | 0.59 | 9.0 | 8.8 |
| spiro-OMeTAD | 12.5 | 0.98 | 0.68 | 8.4 | 7.3 |

*Average of 4 cells

### 5.2.2 Co-evaporated formamidinium lead iodide perovskite solar cells

Formamidinium lead iodide ($FAPbI_3$) perovskite layer has also been investigated as the light-absorbing layer of the solar cells. $FAPbI_3$ shows a higher thermal stability (decomposed on ca. 150°C) and a wider light-absorbing length than $MAPbI_3$ (decomposed on ca. 120°C).[19,20] The appropriate deposition ratio of formamidinium iodide (FAI) and $PbI_2$ was also tuned to set for the high efficiency. The cell fabricated with the co-evaporated $FAPbI_3$ layer formed by the ratio of FAI:$PbI_2$ = 5:1 and spiro-OMeTAD showed the photovoltaic conversion efficiency of 8.6 % (maximum) and 7.4 % (average), compared to the cells with $MAPbI_3$ of 8.4 % (maximum) and 7.3% (average) in the same batch (Figure 5.6 and Table 5.3). $FAPbI_3$ also played a role as a fine light-absorbing layer of the perovskite solar cells.

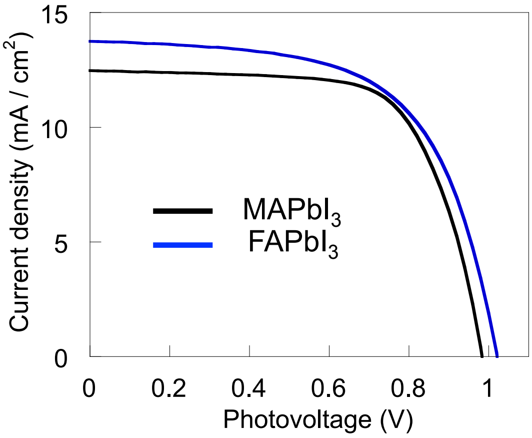

Figure 5.6 *J-V* curves of the perovskite solar cells fabricated with co-evaporated $MAPbI_3$ and $FAPbI_3$.

**Table 5.3** Photovoltaic characteristics of perovskite solar cells fabricated with co-evaporated perovskite layers

| | $J_{SC}$ (mA/cm$^2$) | $V_{OC}$ (V) | $FF$ (-) | $\eta_{Max.}$ (%) | $\eta_{Ave.}$ (%) |
|---|---|---|---|---|---|
| $FAPbI_3$ | 13.7 | 1.02 | 0.61 | 8.6 | 7.4 |
| $MAPbI_3$ | 12.5 | 0.98 | 0.68 | 8.4 | 7.3 |

*Average of 6 cells

A monolithic 2 cations perovskite layer of $MAPbI_3$ on $FAPbI_3$ was tried to apply for the photovoltaic conversion layer of the cells (Figure 5.7).[21] The efficiency was only 3.3 % but some cells showed high voltage of over 1.1 V. The mix-cations perovskite solar cells fabricated by the evaporation methods is expected as highly efficient cells.

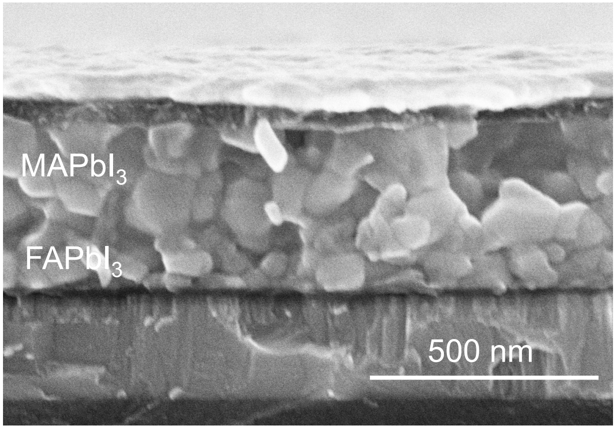

Figure 5.7 *J-V* curves of the perovskite solar cells fabricated with co-evaporation methods

### 5.2.3 Perovskite surface passivation by formamidinium hydrobromide via an evaporation method

Alkylammonium salt, representatively formamidinium hydrobromide (FABr), have been used for a passivation of perovskite surfaces to enhance the photovoltaic conversion efficiency and the durability.[22,23] However, the surface passivation has been executed by only solution processes; therefore, it has been difficult to apply for the large area fabrication. FABr was deposited on the 4-cations perovskite layer by the evaporation method for executing a large area surface passivation. The perovskite solar cells fabricated with passivated 4-cations perovskite layers by FABr evaporation showed higher photovoltaic performance of 18.3 % than that of primitive cells (Figure 5.8 and Table 5.4). The facile evaporation process can realize the surface passivation on large cells.

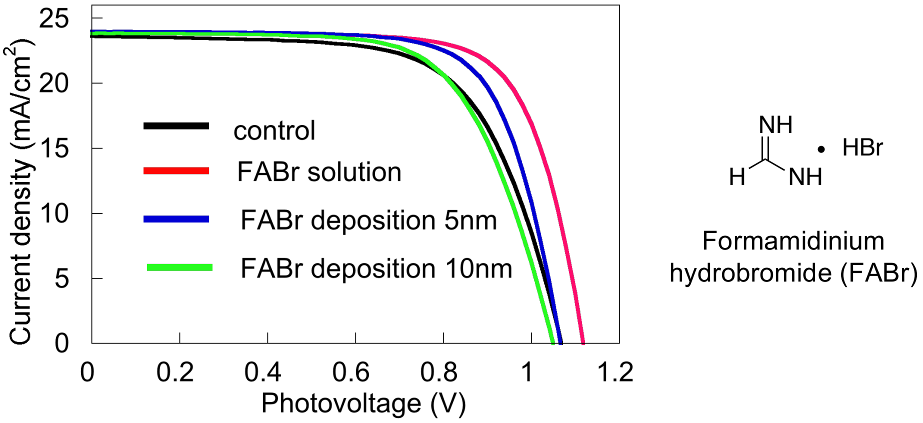

Figure 5.8 *J-V* curves of the perovskite solar cells fabricated with FABr surface passivation by the evaporation.

**Table 5.4** Photovoltaic characteristics of perovskite solar cells fabricated with the FABr passivation

| | $J_{SC}$ (mA/cm$^2$) | $V_{OC}$ (V) | *FF* (-) | $\eta$ (%) |
|---|---|---|---|---|
| - | 23.6 | 1.07 | 0.65 | 16.5 |
| FABr solution | 23.9 | 1.12 | 0.73 | 19.5 |
| FABr deposition 5 nm | 24.0 | 1.07 | 0.72 | 18.3 |
| FABr deposition 10 nm | 23.8 | 1.05 | 0.66 | 16.6 |

## 5.3 Hole-Transporting Poly(terthiophene) Layer and its Simulation for Durable Perovskite/Silicon Tandem Solar Cells

Tandem solar cells with the textured surface structure of micrometer scale pyramids can suppress surface light reflection and redirect light into the cells to enhance photovoltaic conversion efficiencies; therefore, homogeneous layer formation on textured substrates is essential for the perovskite/silicon tandem solar cells. [11−13] The in-situ vapor-phase polymerized terthiophene (PTTh) was prepared as an effective hole-transporting material of durable all-evaporated perovskite solar cells in Chapter 4. The PTTh layer formed with the in-situ vapor-phase method could perfectly cover the pyramidal structure of the textured silicon substrates (Figure 5.9). The formation of the homogeneous polymer layer with a thickness of ca. 40 nm using in-situ vapor-phase polymerization method on the textured substrates proposed the application of PTTh as the hole-transporting material of the efficient tandem cells.

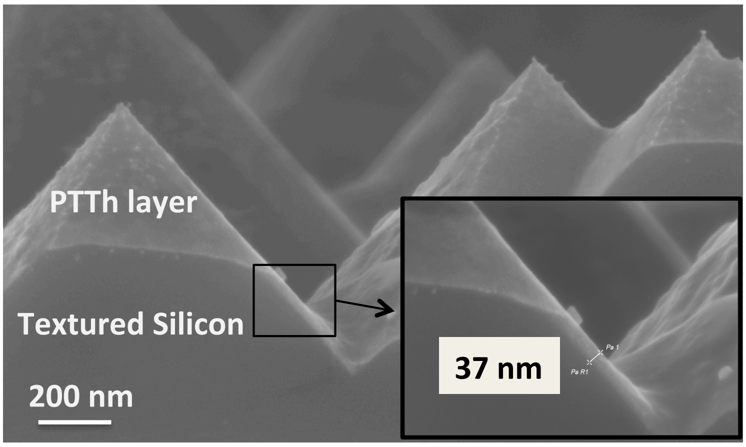

Figure 5.9 Cross-sectional SEM images of PTTh layer formed on the textured silicon substrate.

Applicability of the PTTh to the perovskite/silicon tandem solar cells was also confirmed by the optical simulation. At first, the tandem cell structure and reflective index and extinction coefficient (*n*-*k*) data[24] of the each layer were set for the simulation (Figure 5.10).

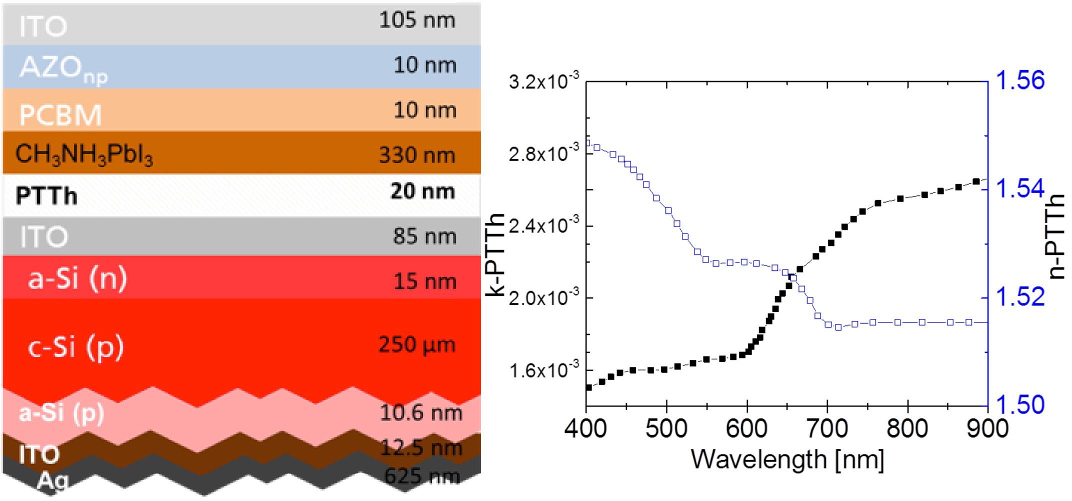

Figure 5.10 Cell structure and *n*-*k* data for PTTh for OPTOS simulation.

Optical properties of textured optical sheets (OPTOS) simulation was executed for confirming the extra-absorption of other layers and gave the simulated photocurrent of the tandem cells.[15,16] One concern of the PTTh application is a visible absorption (adsorption edge of 638 nm as described in Chapter 4). The OPTOS simulation proved a negligible parasitic absorption of PTTh layer of only 0.02 mA/cm$^2$; therefore, PTTh does not affect for absorption of the perovskite/silicon tandem cells (Figure 5.11). The simulation exhibited the high potential of the PTTh application for the tandem solar cells, in terms of great theoretical short circuit current density of 34.2 mA/cm$^2$.

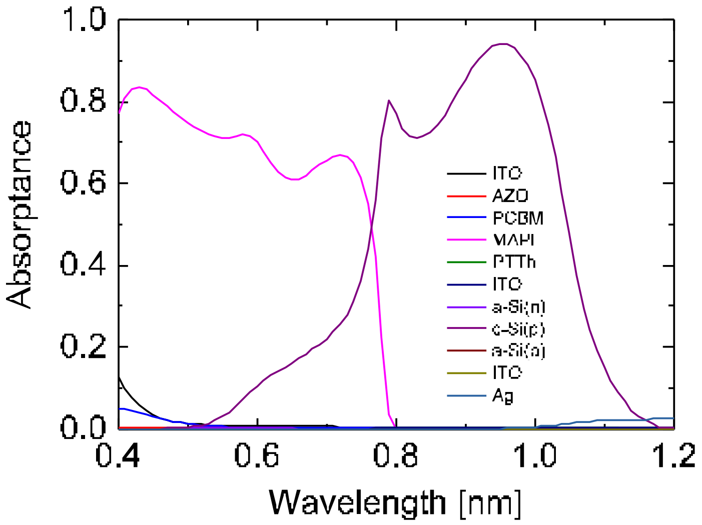

Figure 5.11 OPTOS simulation result of the perovskite silicon tandem cells fabricated with PTTh as the hole-transporting material.

## 5.4 Experimental Section

### 5.4.1 Fabrication method of inverted perovskite solar cells

The perovskite solar cells with the structure of ITO/ATO/*c*-$TiO_2$/PCBM/co-evaporated perovskite layers/hole-transporting materials/Au were prepared. First of all, the ITO/ATO substrates with spattered compact $TiO_2$ (Geomatec Co. Ltd.) were washed by acetone twice and 2-propanol for 10 min sequencially. The substrates were annealed at 500 °C for 1 h. After 15 min UV-$O_3$ treatment, 10 mg/ml PCBM solution in chlorobenzene was spin-coated on the c-$TiO_2$ layer as additional electron-transporting materials. The co-evaporated perovskite layers of both $MAPbI_3$ and $FAPbI_3$ were prepared by the method described in Chapter 4 and only the deposition ratio of alkylammonium and $PbI_2$ was optimized. Spiro-OMeTAD in chlorobenzene (85.8 mg/ml) with 520 mg/mL lithium bis(trifluoromethylsulphonyl) imide (LiTFSI) in acetonitrile (19.4 μL), 100 mg/ml tris(2-(1*H*-pyrazol-1-yl)-4-*tert*-butylpyridine)cobalt(III) tri[bis(trifluoromethane) sulfonamide] (FK209) in acetonitrile (31.6 μL), and *tert*-butylpyridine (*t*BP) (33.8 μL) and PTAA in toluene (10 mg/ml) with 170 mg/mL LiTFSI in acetonitrile (7.5 μL) and *t*BP (4.0 μL) were spin-coated on the perovskite layer at 4000 rpm for 20 s. Finally, 100 nm Au electrode was deposited by the evaporation methods.

PTTh layer was prepared by the in-situ vapor-phase method, as described in Chapter 4, on the washed textured silicon substrates produced by Fraunhofer Institute for Solar Energy System.

### 5.4.2 Measurements

A scanning electron microscope was used to show the cross-sectional images of the cells (Zeiss Auriga 60 CrossBeam workstation scanning electron microscope, Carl Zeiss and SU8000, Hitachi). *J-V* measurement under irradiation and IPCE measurement were performed with a solar cell evaluation system (YQ-2000, JASCO) and a solar simulator (CEP-2000MLQ, Bunkoukeiki). X-Ray patterns were reported by an x-ray diffractometer using the focused beam method (LINT-UltimaIII, Rigaku).

## References

[1] L. U. M. Azzarella, M. A. W. Erth, K. L. J. Äger, M. A. J. Ošt, L. A. R. S. K. Orte, S. T. A. Lbrecht, R. U. S. Chlatmann, B. Ernd, S. Tannowski, *Opt. Express* **2018**, *26*, 81–88.

[2] J. Werner, B. Niesen, C. Ballif, *Adv. Mater. Interfaces* **2018**, *5*, 1700731.

[3] F. Sahli, J. Werner, B. A. Kamino, M. Bräuninger, R. Monnard, B. Paviet-salomon, L. Barraud, L. Ding, J. J. D. Leon, D. Sacchetto, et al., *Nat. Mater.* **2018**, *17*, 820–826.

[4] J. Wemer, F. Sahli, F. Fu, J. J. D. Leon, A. Walter, B. A. Kamino, B. Niesen, S. Nicolay, Q. Jeangros, C. Ballif, *ACS Energy Lett.* **2018**, *3*, 2052–2058.

[5] L. Mazzarella, Y. H. Lin, S. Kirner, A. B. Morales-Vilches, L. Korte, S. Albrecht, E. Crossland, B. Stannowski, C. Case, H. J. Snaith, et al., *Adv. Energy Mater.* **2019**, *1803241*, 1–9.

[6] M. Filipi, P. Löper, B. Niesen, S. De Wolf, J. Kr, C. Ballif, M. Topi, *Opt. Express* **2015**, *23*, 480–484.

[7] Q. Wali, N. K. Elumalai, Y. Iqbal, A. Uddin, R. Jose, *Renew. Sustain. Energy Rev.* **2018**, *84*, 89–110.

[8] G. E. Eperon, T. Leijtens, K. A. Bush, R. Prasanna, T. Green, J. T. Wang, D. P. Mcmeekin, G. Volonakis, R. L. Milot, R. May, et al., *Science* **2016**, *354*, 861–866.

[9] M. Anaya, G. Lozano, M. E. Calvo, H. Miguez, *Joule* **2017**, *1*, 769–793.

[10] J. Avila, C. Momblona, P. Boix, M. Sessolo, M. Anaya, G. Lozano, K. Vandewal, H. Mıguez, H. J. Bolink, *Energy Environ. Sci.* **2018**, *11*, 3292–3297.

[11] L. Cojocaru, K. Wienands, T. W. Kim, S. Uchida, A. J. Bett, S. Rafizadeh, J. C. Goldschmidt, S. W. Glunz, *ACS Appl. Mater. Interfaces* **2018**, *10*, 26293–26302.

[12] G. Longo, C. Momblona, M.-G. La-Placa, L. Gil-Escrig, M. Sessolo, H. J. Bolink, *ACS Energy Lett.* **2018**, *3*, 214–219.

[13] B. W. Schneider, N. N. Lal, S. Baker-finch, T. P. White, *Opt. Express* **2014**, *22*, 1422–1430.

[14] L. Mazzarella, A. B. Morales-vilches, L. Korte, R. Schlatmann, B. Stannowski, *Sol. Energy Mater. Sol. Cells* **2018**, *179*, 386–391.

[15] N. Tucher, J. Eisenlohr, P. Kiefel, O. Höhn, H. Hauser, M. Peters, C. Müller, J. C. Goldschmidt, B. Bläsi, *Opt. Express* **2015**, *23*, 302–307.

[16] N. Tucher, J. Eisenlohr, H. Gebrewold, P. Kiefel, H. Hauser, J. C. Goldschmidt, B. Bläsi, *Opt. Express* **2016**, *24*, 1083–1093.

[17] J. H. Heo, H. J. Han, D. Kim, T. K. Ahn, S. H. Im, *Energy Environ. Sci.* **2015**, *8*, 1602–1608.

[18] C. Quarti, F. De Angelis, D. Beljonne, *Chem. Mater.* **2017**, *29*, 958–968.

[19] Q. Wei, W. Zi, Z. Yang, D. Yang, *Sol. Energy* **2018**, *174*, 933–939.

[20] S. Pang, H. Hu, J. Zhang, S. Lv, Y. Yu, F. Wei, T. Qin, H. Xu, Z. Liu, G. Cui, *Chem. Mater.* **2014**, *26*, 1485–1491.

[21] S. Pisoni, R. Carron, T. Moser, T. Feurer, F. Fu, S. Nishiwaki, A. N. Tiwari, S. Buecheler, *NPG Asia Mater.* **2018**, *10*, 1076–1085.

[22] V. A. Online, K. T. Cho, C. Rolda, P. Gao, Y. Lee, M. K. Nazeeruddin, *Energy Environ. Sci.* **2017**, *2*, 621–627.

[23] B. Li, V. Ferguson, S. R. P. Silva, W. Zhang, *Adv. Mater. Interfaces* **2018**, 1800326.

[24] S. V. Kamat, V. Puri, R. K. Puri, *Phys. Scr.* **2011**, *84*, 045801.

# Chapter 6: Conclusion and Future Prospects

**6.1 Conclusion**

**6.2 Future Prospects**

**References**

## 6.1 Conclusion

In this thesis, the author describes the charge-transporting polymer applications for enhancing the photovoltaic performance and stability of the perovskite solar cells. In this section, the significant conclusions in this study are summarized.

In chapter 2, the preparation of new arylamine polymers via a simple one-pot addition condensation reaction and the application as hole-transporting materials of the perovskite solar cells were described. The preparation condition of the ratio of monomers (arylamine:aldehyde = 1:4) and reaction time (8 h) was warily tuned for obtaining the high molecular weight polymers ($M_w > 10,000$) with the liner structure. The arylamine polymers exhibited appropriate HOMO levels due to the introduction of methyl and methoxy substituents, and high glass transition temperatures over 200 °C owing to their high molecular weights. The polymers gave homogeneous films due to their high solubility in organic solvents derived from the flexible main chain structure. The perovskite solar cells fabricated with the arylamine polymers as the hole-transporting layers exhibited both high photovoltaic conversion efficiency of over 16 % and relatively high thermal durability than the cells with spiro-OMeTAD.

In chapter 3, an incorporation of anti-oxidizing polymers in the perovskite layers for enhancing their stability was described. A radical-bearing redox-active polymer, PTMA, worked as an effective scaffold for forming the high quality perovskite grains and as an eliminating agent of the superoxide anion radical detected by a fluorescent prove, hydroethidine. The enhanced stability of the layer was also confirmed by GC-MS of the decomposed fragment, methylamine. The incorporation of PTMA decreased the resistance of the perovskite layer (13 Ω to 8.8 Ω) and enhanced the photovoltaic current owing to a carrier conductivity of PTMA. A cell fabricated with a PTMA-incorporated perovskite layer gave a photovoltaic conversion efficiency of 18.8 %. The incorporation of phenolic antioxidants also enhanced the stability of the perovskite layer dramatically.

In chapter 4, an in-situ vapor phase polymerized hole-transporting polymer was applied for the hole-transporting layer of the evaporated perovskite solar cells for improving their stability. A thiophene monomer of 2,2’:5’,2”-terthiophene and an evaporable oxidizing agent, iodine, were sequentially evaporated to yield PTTh layers via in-situ polymerization. A homogeneous PTTh layer with high hole mobility of ca. $10^{-3}$ cm$^2$/Vs and an appropriate HOMO level of -5.3 eV was applied to the co-evaporated perovskite solar cells to yield photovoltaic conversion performance of

5.9 %, and higher cell stability compared to the cells with existing low molecular weight hole-transporting materials.

In chapter 5, elemental technologies were developed for the fabrication of perovskite-modified tandem cells. Perovskite layers of $MAPbI_3$ and $FAPbI_3$ formed by the co-evaporation process were applied as light-absorbing layer of the solar cells to yield photovoltaic conversion efficiency of ca. 10 %. The in-situ vapor phase polymerized PTTh thin layer was also applied on the textured silicon substrate.

## 6.2 Future Prospects

The author hopes the sequential development of the perovskite solar cells. In this chapter, the future direction and a potential of the polymer application for further improvement of the cell performance are discussed.

### 6.2.1 Perovskite-based tandem solar cells with charge-transporting polymers

Photovoltaic conversion efficiency of the perovskite solar cells has almost reached at the limit.[1,2] Tandem solar cells must be investigated for further development of the efficiency but another problem is cell durability compared to silicon solar cells.[3,4] An application of charge-transporting polymers can enhance the durability of the perovskite cells owing to their processability and stability.

Elemental technologies for efficient tandem device fabrication were developed in chapter 4 and 5. An integration of these techniques, in-situ vapor phase formed hole-transporting polymers and appropriate light-absorbing perovskite compounds, and an additional combination with appropriate electron-transporting layers, such as in-situ vapor phase polymerized electron-transporting materials, can realize highly efficient and durable perovskite-based tandem solar cells.

### 6.2.2 Effective combination of surface passivation and hole-transporting polymers with long alkyl side chains

Although the hole-transporting materials are important for the effective charge separation, the organic compounds are generally unsuitable for forming on hydrophilic perovskite layers because of their hydrophobicity.[5,6] Spiro-OMeTAD and PTAA have often been used in a lot of reports owing to their formability of amorphous thin films.[5] However, many types of organic charge-transporting materials have been prepared, and a method for effectively use of them has been demanded.

An application of alkylammonium salts with long alkyl chain for a passivation of the perovskite layer was reported.[7] The method modified the perovskite layer by reacting with remained $PbI_2$ and gave hydrophobic surface on the perovskite layer. The cells fabricated with *n*-hexyl trimethylammonium bromide and poly(3-hexylthiophene) showed the high efficiency of 22.7% and high durability derived from and the surface passivation layer and the polymer layer.[7] This research can provide a possibility for a lot of hole-transporting materials that have not been applied due to their unfamiliarity with the perovskite layer (Figure 6.1). Further efficiency and durability can be realized by the optimized material applications based on "polymer chemistry".

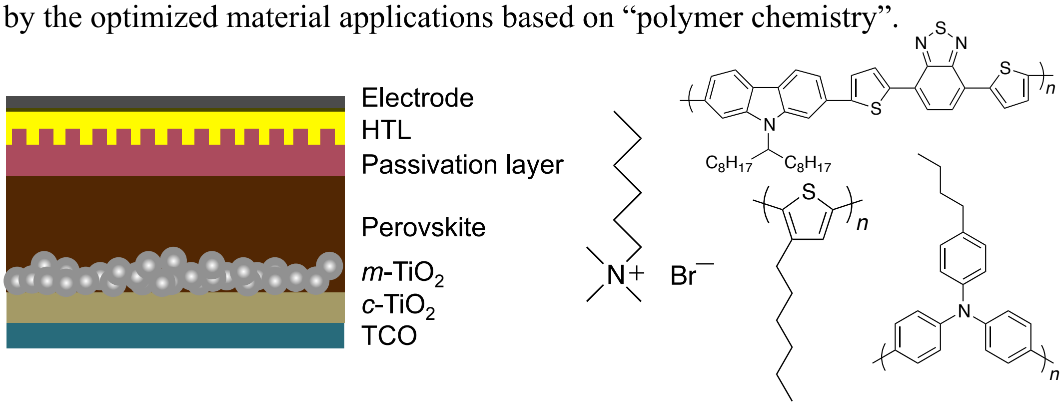

Figure 6.1 Structural image of the passivated perovskite solar cell and examples of alkylammonium salt and hole-transporting polymers with long alkyl side chains

## References

[1] L. M. Pazos-Outon, T. P. Xiao, E. Yablonovitch, *J. Phys. Chem. Lett.* **2018**, *9*, 1703–1711.
[2] C. H. Ng, H. N. Lim, S. Hayase, Z. Zainal, N. M. Huang, *Renew. Sustain. Energy Rev.* **2018**, *90*, 248–274.
[3] Q. Wali, N. K. Elumalai, Y. Iqbal, A. Uddin, R. Jose, *Renew. Sustain. Energy Rev.* **2018**, *84*, 89–110.
[4] N. Tucher, O. Höhn, J. Murthy, J. C. Martinez, M. Steiner, A. Armbruster, E. Lorenz, B. Bläsi, J. C. Goldschmidt, *Opt. Express* **2019**, *27*, 1419–1430.
[5] Z. Yu, L. Sun, *Adv. Energy Mater.* **2015**, *5*, 1500213.
[6] M. Abd, F. Aziz, A. Fauzi, W. Norharyati, W. Salleh, N. Yusof, J. Jaafar, T. Soga, M. Zainizan, N. Ahmad, *Appl. Mater. Today* **2018**, *13*, 69–82.
[7] E. H. Jung, N. J. Jeon, E. Y. Park, C. S. Moon, T. J. Shin, T.-Y. Yang, J. H. Noh, J. Seo, *Nature* **2019**, *567*, 511–515.

## List of Publications

1. Koki Suwa, Suguru Tanaka, Kenichi Oyaizu, Hiroyuki Nishide
"Arylamine Polymers Prepared via Facile Paraldehyde Addition Condensation: an Effective Hole-Transporting Material for Perovskite Solar Cells"
*Polymer International*, **67**, 670 (2018.2).

2. Koki Suwa, Kenichi Oyaizu, Hiroshi Segawa, Hiroyuki Nishide
"Anti-Oxidizing Radical Polymer-Incorporated Perovskite Layers and their Photovoltaic Characteristics"
*ChemSusChem*, **12**, 5207 (2019.10).

3. Koki Suwa, Ludmila Cojocaru, Karl Wienands, Clarissa Hofmann, Patricia S. C. Schulze, Alexander J. Bett, Jan Christoph Goldschmidt, Stefan W. Glunz, Hiroyuki Nishide
"Vapor-Phase Formation of a Hole-Transporting Thiophene Polymer layer for Evaporated Perovskite Solar Cells"
*ACS Applied Materials and Interfaces*, in press (2020. 2).

4. Hirofumi Maruo, Yusuke Sasaki, Kohei Harada, Koki Suwa, Kenichi Oyaizu, Hiroshi Segawa, Kenneth Carter, Hiroyuki Nishide
"Hole-transporting diketopyrrolopyrrole-thiophene polymers and their additive-free application for a perovskite-type solar cell with an efficiency of 16.3%"
*Polymer Journal*, **51**, 91 (2018.8).

5. Ludmila Cojocaru, Koki Suwa, Ulas Edril, Karl Wienands, Severin Vierrath, Matthias Breitwieser, Nico Tucher, Jan Christoph Goldschmidt, Hiroyuki Nishide, Stefan W. Glunz
"High-Quality Perovskite Absorber and Hole Transport Layer for Efficient Perovskite Solar Cells"
Freiburg Center for Interactive Materials and Bio-inspired Technologies (FIT)-report 2018, ISBN: 987-3-946018-04-9 (2019.3).

## List of Presentations

Oral Presentations

1. Koki Suwa, Kenichi Oyaizu, Hiroshi Segawa, Hiroyuki Nishide
"Perovskite Crystals Formed with TEMPO-Substituted Polymers as an Effective Scaffold and their Photovoltaic Characteristics"
*The 67th Annual Meeting of the Society of Polymer Science*, Nagoya, May 2018.

2. Koki Suwa, Kenichi Oyaizu, Hiroyuki Nishide
"Radical Polymer Application for the Highly Efficient Perovskite Solar Cells"
*Waseda-Peking Joint Workshop on Green Innovation*, Tokyo, January 2018.

3. Koki Suwa, Kenichi Oyaizu, Hiroyuki Nishide
"Hole-Transporting Polymers for Organic-Inorganic Perovskite Solar Cells"
*Waseda-Peking Joint Workshop on Green Innovation*, Peking, China, February 2017.

Poster Presentations

1. Koki Suwa, Kenichi Oyaizu, Hiroshi Segawa, Hiroyuki Nishide
"Anti-Oxidizing Perovskite Layer Formation via an Addition of Radical Polymers and its Photovoltaic Cells"
*Hybrid and Organic Photovoltaics Conference (HOPV-19)*, Rome, Italy, May 2019.

2. Koki Suwa, Kenichi Oyaizu, Hiroshi Segawa, Hiroyuki Nishide
"Redox-Active TEMPO Polymers as a Scaffold of Perovskite Layer Formation for a High Efficiency and Durability"
*4th International Conference on Perovskite Solar Cells and Optoelectronics (PSCO-18)*, Lausanne, Switzerland, September 2019.

3. Koki Suwa, Kenichi Oyaizu, Hiroshi Segawa, Hiroyuki Nishide
"Perovskite Layers Formed with Functional Polymers as a Scaffold and their Photovoltaic Characteristics"
*Grand Renewable Energy 2018*, Yokohama, 2018.6.

4. Koki Suwa, Kenichi Oyaizu, Hiroshi Segawa, Hiroyuki Nishide
”Perovskite Layer Composited with Radical Polymer and Improved Durability of the Cell”
*3rd International Conference on Perovskite Solar Cells and Optoelectronics (PSCO-17)*, Oxford, UK, September 2017.

5. Koki Suwa, Kenichi Oyaizu, Hiroshi Segawa, Hiroyuki Nishide
”Highly Durable Perovskite Layer Composited with Radical Polymer and its Application for a Solar Cell”
IUPAC 17th International Symposium on MacroMolecular Complexes (MMC-17), Tokyo, August 2017.

6. Koki Suwa, Hirofumi Maruo, Kenichi Oyaizu, Hiroshi Segawa, Hiroyuki Nishide
“Arylamine Polymers Prepared with a Very Facile Addition Condensation and their Application as a Hole Transporting Layer of Perovskite Solar Cells”
The 2nd Asia-Pacific Hybrid and Organic Photovoltaics Conference (AP-HOPV 18), Kanagawa, February 2017.

7. Koki Suwa, Hirofumi Maruo, Kenichi Oyaizu, Hiroyuki Nishide
“Synthesis of Amorphous Arylamine Polymers and its Application for Perovskite Solar Cells as a Hole Transporting Material”
6th Jilin-Korea-Waseda Alliance Annual Symposium, Jilin, China, August 2016.

## Awards

Excellent Poster Award

6th CSJ Chemistry Festa (Tokyo, December 2016)

## Acknowledgement

The present thesis is the collection of the studies conducted under the direction of Prof. Dr. Kenichi Oyaizu and Prof. Dr. Hiroyuki Nishide, Department of Applied Chemistry in Waseda University, during 2015-2020. The author expresses the greatest acknowledgement to Prof. Dr. Kenichi Oyaizu and Prof. Dr. Hiroyuki Nishide for invaluable suggestions, discussion, and encouragement throughout my laboratory life.

The author expresses the great acknowledge to Prof. Dr. Yukio Furukawa and Prof. Dr. Yoshinori Nishikitani for their valuable advice, discussion, and the opportunity for the acceptance on their laboratory.

The author is extremely grateful to Dr. Ludmila Cojocaru (Bordeaux Univ.) for her valuable advice, discussion, and opportunity for the collaborative research on a co-evaporation method of perovskite solar cells with Department of Sustainable Systems Engineering (INATECH) of University of Freiburg and Fraunhofer Institute for Solar Energy Systems (ISE).

The author expresses the great acknowledge to Dr. Michio Suzuka (Panasonic Co.) for his meaningful discussion as a member on judging committee for the doctoral thesis.

The author expresses the great acknowledge to Assistant Prof. Dr. Takeo Suga and Dr. Kan Hatakeyama-Sato for the technical suggestions and very kind support.

The author is grateful to Prof. Dr. Hiroshi Segawa and the members of his laboratory in The University of Tokyo for their technical advice and productive discussion.

The author expresses the special thanks to Prof. Dr. Stefan W. Glunz, Dr. Jan Christoph Goldschmidt, and the members of INATECH and Fraunhofer ISE for the heartwarming acceptance in their laboratory, technological advices, and kind supports.

The author is grateful to Dr. Hirofumi Maruo (NOK Co.), Dr. Ryo Kato (Chicago Univ.), Dr. Yoshito Sasada (Hitachi Ltd.), Dr. Hiroshi Tokue (Mitsubishi Chemical Co.), Dr. Takuma Kawai (Japan Tabacco Inc.), Mr. Wang Yu, and Mr. Koki Oka for technical supports, powerful discussion, and assistance.

The author expresses the special thanks to all team members, Mr. Masaki Takamura (NIPPON STEEL Chemical & Material Co.), Mr. Kohei Harada (JSR Co.), Ms. Risano Nakajima (Toray Industries Inc.), Mr. Shinichiro Watanabe (SII Crystal Technology Co.), Mr. Yusuke Sasaki (TOSOH Co.), Mr. Suguru Tanaka (Mitsui Chemical Inc.), Ms. Kanako Noguchi (DIC Co.), Mr. Wataru Okada (Mitsui Chemical Inc.), Mr. Yuta Shirogane (Mitsui Chemical Inc.), Ms. Mayu Yamaguchi (Mitsubishi Chemical Co.), Mr. Akihiro Okada, Mr. Keisuke Sugai, Ms. Marika Owada, Mr. Koichiro Kamimori, and Ms. Haruka Sugiyama.

The author is extremely grateful to Ms. Ayano Nozawa and Ms. Akie Takizawa.

The author deeply thanks all members in the laboratory for their fruitful discussion and kind assistance.

Special thanks to the Leading Graduate Program in Science and Engineering, Waseda University, from MEXT, Japan.

Finally, the author expresses his deepest gratitude heartily to his family, Mr. Yasunori Suwa, Ms. Junko Suwa, Mr. Hiroki Suwa, and Mr. Taiki Suwa for their heartfelt supports.

February, 2020
Koki Suwa